1994

Reactions of trifluoroiodomethane on metal surfaces

Mark Brian Jensen
Iowa State University

Order Number 9518392

Reactions of trifluoroiodomethane on metal surfaces

Jensen, Mark Brian, Ph.D.

Iowa State University, 1994

U·M·I
300 N. Zeeb Rd.
Ann Arbor, MI 48106

Reactions of trifluoroiodomethane on metal surfaces

by

Mark Brian Jensen

A Dissertation Submitted to the

Graduate Faculty in Partial Fulfillment of the

Requirements for the Degree of

DOCTOR OF PHILOSOPHY

Department: Chemistry
Major: Analytical Chemistry

Approved:

Signature was redacted for privacy.

In Charge of Major Work

Signature was redacted for privacy.

For the Major Department

Signature was redacted for privacy.

For the Graduate College

Iowa State University
Ames, Iowa

1994

DEDICATION

To my family,

Dad, Mom, Greg, Chris, Katie, and Molly

And in memory of my grandmothers,

Trina Poulsen and Nina Jensen

TABLE OF CONTENTS

ACKNOWLEDGMENTS

I am indebted to my research advisor, Professor Patricia Thiel, for her support and guidance over the past five years. Her confidence in me, as well as her patience with me, especially in times I felt undeserving of either, will always be remembered.

I will forever have nothing but fond memories of the Thiel research group. I have had the good fortune of being surrounded by not only good scientists, but wonderful individuals, several of whom I consider among the best friends I've ever had. I am grateful to Dr. Jim Dyer and Dr. Wai Leung for teaching me the basics of ultra-high vacuum technology. Once on my own, the helpful assistance of Drs. Joe Burnett, Luke Chang, Mike Columbia, Cynthia Jenks, Uwe Myler, and Oden Warren was greatly appreciated, as well as desperately needed. A heartfelt thanks also goes to Karen Gilley and Stacy Joiner for tremendous help and numerous un-repaid favors.

I thank Professor J.M. White at the University of Texas at Austin for providing me the opportunity to escape the Iowa winter for three weeks to learn something about X-ray photoelectron spectroscopy. Also, I am deeply grateful to Eddie Pylant, my XPS mentor, for his limitless patience and persistence during some late nights and early mornings.

I will make no attempt at an all-inclusive list of the wonderful friendships I have built while in Ames, as it would be almost endless. Within the chemistry department I have already mentioned the members of the Thiel group. I wish to also make special mention of Lloyd Allen, Tonya Bricker, Dr. Dave Dobberpuhl, Steve

Johnson, Dave Lang, Dr. Leslie Perkins, and Dr. Mitch Robertson. Sharing each others joys and frustrations has left me with memories I will cherish the rest of my life. I have been truly blessed to be surrounded by such wonderful friends. I also want to make special mention of the many good friends I've made in the ISU Weightlifting Club. Many times I've come into the gym frustrated after a bad day in the lab, only to be remarkably cheered up by the "stimulating" conversation.

I wish to thank the people of Memorial Lutheran Church for providing me with a haven from the pressures of graduate school, as well as an environment in which to nurture my faith. In particular, I thank Dennis Johnson, Anne Osslund, and Lois Theesfield for the opportunity to worship God through a quality of music which truly reflects His majesty.

Finally, I must thank my family, to whom this dissertation is dedicated. The love and support they give me is unfailing. I am forever thankful for the value system instilled in me at a young age which forms the basis of who I am and all that I will ever be.

I acknowledge financial support provided in part by a GAANN Fellowship from the U.S. Department of Education and a GSFAP Scholarship provided by the state of Iowa. Funding for this work comes primarily from the National Science Foundation through Grant No. CHE-9024358. This work was performed at Ames Laboratory, operated by Iowa State University for the U.S. Department of Energy under Contract No. W-7405-ENG-82. The United States government has assigned the DOE Report number IS-T-1725 to this dissertation.

ABSTRACT

To further understand reactions of fluorocarbons relevant to a number of technological applications, several surface-sensitive analytical techniques are applied to an investigation of the thermal and electron-induced chemistry of trifluoroiodomethane (CF_3I) on Ru(001) and Ni(100) surfaces.

Ni(100) is found to be very active toward C-F bond scission, as a significant amount of CF_3I thermally decomposes to its atomic constituents following adsorption at 100 K. Thermal desorption spectroscopy (TDS) shows that desorption of NiF_2 and I increases linearly with CF_3I exposure until reaching a saturation level. A small amount of CF_3 desorption is detected as the exposure approaches saturation, indicating that adsorbed CF_3 is stabilized as the surface sites required for decomposition become less available.

Electron-induced decomposition (EID) of multilayer CF_3I occurs with a cross-section of 1.5×10^{-16} cm^2. F^+ is the dominant product detected during electron irradiation. A number of new thermal desorption products are observed following electron irradiation. Of particular interest is a series of carbon-carbon bond formation products likely produced in the multilayer as a result of EID. The mechanism through which these products form may mimic the proposed electron-induced cross-linking of fluoropolymer chains.

Exposure of CF_3I to Ru(001) at 100 K results in a complex mixture of CF_n (n=2-4) thermal desorption products. X-ray photoelectron spectroscopy (XPS), low-

energy electron diffraction (LEED), and H_2 coadsorption experiments suggest that the reactions which lead to these desorption products are regulated by the availability of surface sites. High-resolution electron energy loss spectroscopy (HREELS), in conjunction with electron-stimulated desorption ion angular distribution (ESDIAD), suggests that adsorbed CF_3 adopts a "tilted" configuration in which one C-F bond is oriented normal to the surface plane.

ESDIAD identifies a number of interesting patterns which give insight into the surface chemistry of CF_3I on Ru(001), as well as the surface structure of the resulting products. A small hexagonal pattern is attributed to electron-stimulated desorption (ESD) of atomic fluorine adsorbed at step and defect sites, while two larger hexagons are attributed to various orientations of adsorbed CF_3.

CHAPTER I. GENERAL INTRODUCTION

Surface chemists are often faced with the challenge of simulating the behavior of a complex chemical environment with a simpler model system. The goal is to examine fundamental chemical interactions by eliminating as many of the variables associated with the real environment as possible. If the behavior of the model system is found to differ from that of the real system, these variables can be reintroduced systematically until those crucial to the behavior of the real system are determined. A classic example is the surface science approach to heterogeneous catalysis.[1] One begins by determining the chemistry of a simple molecule adsorbed on a clean, atomically smooth single crystal surface. Features of the working catalyst are then introduced. The physical features of steps and kinks on the real catalyst surface may be simulated by high-Miller-index crystal faces, or the chemical composition may be altered by coadsorption of possible interferant adsorbates. This process continues until the model catalyst behaves in a manner analogous to that of the working catalyst.

The surface science approach to fluorocarbon chemistry is another example of simulating a complicated, sometimes harsh environment with simpler model systems. The importance of fluorocarbons in industrial applications is well known. Most of these applications rely on the stability of these compounds toward thermal and oxidative degradation. Perfluoropolyethers (PFPE), commercially available under

such names as Fomblin, Demnum, and Krytox, are a class of compounds widely used as synthetic lubricants in a variety of industries.[2] While thought to be generally inert in the harsh environments to which these lubricants are often exposed, decomposition at high temperature in the presence of metals has been noted.[3-5]

A number of surface studies have been carried out in an attempt to model the interactions of PFPE lubricants with metal and metal oxide surfaces.[6-18] The aim is to better understand these interactions, as well as to clarify the mechanisms of decomposition. Most of these studies have modeled the PFPE polymer systems with simpler fluorinated ether analogs adsorbed on single crystal and polycrystalline metal and metal oxide surfaces. The initial work involved adsorbing simple fluorinated ethers on clean, atomically smooth surfaces.[11,13] When no ether decomposition was observed, the investigations were modified to introduce a number of possible causes for the polymer degradation. For example, the effects of surface morphology,[10] surface composition,[10-12] number of ether linkages,[12,18] and position of ether linkages[8] have all been investigated. As a result of these studies, the observed decomposition of these monomer-like compounds, as well as decomposition of the polymeric lubricants, has been proposed to be driven by C-F bond cleavage, resulting in the formation of metal fluorides which then catalyze further decomposition of the fluorinated ether.[15,17]

To examine the fundamental C-F bond scission activity of metal surfaces, we turn to studies of trifluoroiodomethane (CF_3I). Alkyl halides have become widely used in surface science as precursors to adsorbed alkyl groups thought to be

intermediates in many catalytic processes of industrial importance.[19,20] The carbon-halogen bond of a typical alkyl halide is easily broken, either thermally or photolytically, resulting in adsorbed halogens and alkyl species. The subsequent thermal chemistry of these alkyl groups is often complex, and is dependent upon the catalytic properties of the metal substrate. Iodomethane (CH_3I), for example, has been studied on a number of surfaces,[21-38] with the resulting thermal chemistry ranging from no dehydrogenation on Ag(111)[37] to complete dissociation to C(ad), H(ad), and I(ad) on (100) oriented polycrystalline tungsten foil.[25]

Like its hydrogenated analog, CF_3I undergoes thermally-induced C-I bond cleavage, and thus has received increasing attention in the surface science community in recent years as a precursor to adsorbed trifluoromethyl groups. The thermal chemistry of CF_3I has been studied on a number of surfaces using a number of surface-sensitive techniques.[39-44] As expected, the resulting chemistry following adsorption at low temperature is very dependent upon the substrate. No C-F bond cleavage is observed on Ag(111),[40] while a substantial number of C-F bonds are broken on both Ru(001)[39] and Pt(111).[43]

One technique not yet applied to the study of CF_3I is electron-stimulated desorption ion angular distribution (ESDIAD), a relatively new, yet powerful tool for determining adsorbate geometry.[45] The extreme sensitivity of fluorine-containing compounds to electron- and radiation-induced bond cleavage makes these compounds especially well-suited to ESD techniques. Indeed, while ESDIAD has not been applied to any previous investigation of CF_3I, it has been used to determine the

structures of other fluorine-containing compounds, most notably NF_3[46] and PF_3,[47-54] adsorbed on metal surfaces. The C_{3v} symmetry of the CF_3I molecule leads to the expectation of interesting ESDIAD images due to some form of azimuthal ordering.

The chemical changes induced by the interaction of electrons with fluorocarbons has received little attention in surface science studies, yet the understanding of this process is of fundamental importance to a number of technological applications. There is much interest in the effects of electron and photon bombardment of fluorocarbon polymers.[55-72] A number of studies have investigated the proposed cross-linking of polytetrafluoroethylene (PTFE, better known by its du Pont trade name, Teflon).[55-67] Teflon is of tremendous value in electronic applications due to its low dielectric constant, but, because of its well-known chemical inertness, is difficult to use in electronic device fabrication. It has been found, however, that if Teflon is first etched in a sodium naphthalenide solution, copper films may be deposited onto the etched portion via gas phase chemical vapor deposition (CVD) from Cu(I) precursors,[62] or via electroless solution-phase deposition.[64] Recently, it has been shown that selective copper pattern formation is possible on a Teflon substrate which has been irradiated with small doses of either X-rays or electrons prior to the chemical etching step.[67] Copper deposited by CVD will then adhere only to the areas of the surface which were not irradiated. Copper deposited electrolessly will adhere to the entire surface, but weakly enough on the irradiated areas so as to be easily peeled away without damage to the non-irradiated areas. This selective patterning offers tremendous benefits to the design of

microelectronic devices. Thin copper films may be deposited on a low dielectric material, limited only by the size of the irradiating beam. Electron irradiation offers simple control of beam size and position, making this method preferable to X-ray irradiation.

There is some question as to what effect the irradiation step has on the Teflon surface. The sodium naphthalenide etching step is thought to result in defluorination, yielding NaF as the etching product. It has been proposed that the irradiation step results in a rigid "cross-linking" of the polymeric chains, thereby inhibiting the penetration of sodium into the bulk of the substrate and keeping the surface inert toward copper adhesion.[56] Direct evidence for cross-linking has been difficult to obtain. Indirect evidence comes from thermal desorption analysis of irradiated Teflon.[56] These results show that with increasing irradiation time there is an increase in desorption of low molecular weight fluorocarbons, thought to be products of C-C and C-F bond scission reactions which result in free-radical cross-linking of the polymer chains. Further evidence for cross-linking comes from C(1s) XPS studies which report similar XPS spectra for an irradiated Teflon surface and cross-linked plasma-polymerized fluorocarbons.[63]

The importance of electron-induced cross-linking of fluorocarbon polymers is not limited to copper adhesion on Teflon. Returning to the role of fluorocarbons as lubricants, it has been reported that thin films of perfluoropolyether lubricants adhere more strongly to a number of surfaces following irradiation of the thin film with 185 nm photons.[68] Irradiation with low-energy electrons was found to yield the same

results.[72] Dissociative electron attachment was proposed, resulting in the formation of a radical and a F^- ion, followed by radical propagation and termination, which cross-link the polymer and attach it to the surface.[72] This process has been successfully applied to enhance the adhesion of PFPE lubricants to magnetic recording media.[70,71]

As stated above, direct evidence for cross-linking of fluorocarbon polymers is difficult to obtain. However, if the proposed cross-linking process is modeled by the electron bombardment of small fluorocarbons adsorbed on a surface, mass spectrometry may be used to directly observe carbon-carbon coupling. A previous study of the effects of low-energy electrons on a chemisorbed monolayer of CF_3Cl on Pt(111) made no mention of the formation of C-C bonds.[73] However, this may not have been a realistic model of a polymer surface, simply because the fluorocarbon adlayer is thin and close to a perturbing metal surface. If the initial adlayer coverage is increased to several layers, any interference from the solid substrate could be effectively eliminated, resulting in a more realistic model of the polymer. Again, in the tradition of surface science described earlier, this would be a refinement of a very simple system in such a way as to more accurately model a complex system.

The purpose of the work presented in this dissertation is three-fold. First, the thermal chemistry of CF_3I on Ru(001) and Ni(100) is investigated to determine the pathways of decomposition, as well as the relative activities of these two metals toward C-F bond scission, the principle step in perfluoropolyether lubricant decomposition. Second, the ESDIAD technique is used to investigate the structure

of CF_3I and its decomposition products on Ru(001). Finally, the effects of electron bombardment on multilayer CF_3I adsorbed on Ni(100) are studied in an attempt to gain direct evidence of electron-induced C-F bond scission followed by carbon-carbon coupling.

Dissertation Organization

The body of this dissertation contains three journal papers followed by a General Conclusions chapter. The first paper, "Thermally-Induced and Electron-Induced Chemistry of CF_3I on Ni(100)", has been accepted for publication by the Journal of the American Chemical Society. The second paper, "Reactivity and Structure of CF_3I on Ru(001)", has been submitted to the Journal of Physical Chemistry. The third paper, "An ESDIAD and LEED Investigation of CF_3I on Ru(001)", will be submitted to Langmuir. References are specific to each paper; therefore, each paper is followed by its own reference list.

Two appendices are included. The first, "Local and Collective Structure of Formate on Pt(111)", describes an application of the ESDIAD experiment not related to the CF_3I work. It appears in Volume 290 of Surface Science Letters on pages L655-L661. The second appendix describes the specific instrumentation, as well as the experimental method, used to collect the ESDIAD data presented in this dissertation.

References

(1) Somorjai, G. A. *Introduction to Surface Chemistry and Catalysis*; John Wiley and Sons: New York, 1994; pp 461.

(2) Del Pesco, T. W. In *Synthetic Lubricants and High-Performance Functional Fluids*; R. L. Shubkin, Ed.; Marcel Dekker: New York, 1993; pp 145.

(3) Jones, W. R., Jr.; Paciorek, K. J. L.; Ito, T. I.; Kratzer, R. H. *Ind. Eng. Chem. Prod. Res. Dev.* **1983**, *22*, 166.

(4) Snyder, C. E., Jr.; Dolle, R. E., Jr. *ASLE Trans.* **1976**, *19*, 171.

(5) Sianesi, D.; Zamboni, V.; Fontanelli, R.; Binaghi, M. *Wear* **1971**, *18*, 85.

(6) Napier, M. E.; Stair, P. C. *Surf. Sci.* **1994**, *316*, 317.

(7) Golden, W. G.; Hunziker, H.; de Vries, M. S. *J. Phys. Chem.* **1994**, *98*, 1739.

(8) Jenks, C. J.; Jacobson, J. A.; Thiel, P. A. *J. Vac. Sci. Technol. A* **1994**, *12*, 2101.

(9) Walczak, M. M.; Leavitt, P. K.; Thiel, P. A. *Trib. Trans.* **1990**, *33*, 557.

(10) Leavitt, P. K.; Thiel, P. A. *J. Vac. Sci. Technol. A* **1990**, *8*, 2269.

(11) Maurice, V.; Takeuchi, K.; Salmeron, M.; Somorjai, G. A. *Surf. Sci.* **1991**, *250*, 99.

(12) Takeuchi, K.; Salmeron, M.; Somorjai, G. A. *Surf. Sci.* **1992**, *279*, 328.

(13) Walczak, M. M.; Leavitt, P. K.; Thiel, P. A. *J. Am. Chem. Soc.* **1987**, *109*, 5621.

(14) Napier, M. E.; Stair, P. C. *Surf. Sci.* **1993**, *298*, 201.

(15) Napier, M. E.; Stair, P. C. *J. Vac. Sci. Technol. A* **1991**, *9*, 649.

(16) DeKoven, B. M.; Meyers, G. F. *J. Vac. Sci. Technol. A* **1991**, *9*, 2570.

(17) John, P. J.; Liang, J. *J. Vac. Sci. Technol. A* **1994**, *12*, 199.

(18) Walczak, M. M.; Thiel, P. A. *Surf. Sci.* **1989**, *224*, 425.

(19) Zaera, F. *Acc. Chem. Res.* **1992**, *25*, 260, and references therein.

(20) Zaera, F. *J. Mol. Catal.* **1994**, *86*, 221, and references therein.

(21) Lin, J.-L.; Bent, B. E. *J. Vac. Sci. Technol. A* **1992**, *10*, 2202.

(22) Zhou, X.-L.; White, J. M. *Surf. Sci.* **1988**, *194*, 438.

(23) Tjandra, S.; Zaera, F. *Langmuir* **1992**, *8*, 2090.

(24) Tjandra, S.; Zaera, F. *J. Vac. Sci. Technol. A* **1992**, *10*, 404.

(25) Zhou, X.-L.; Yoon, C.; White, J. M. *Surf. Sci.* **1988**, *206*, 379.

(26) Chiang, C.-M.; Wentzlaff, T. H.; Jenks, C. J.; Bent, B. E. *J. Vac. Sci. Technol. A* **1992**, *10*, 2185.

(27) Chiang, C.-M.; Wentzlaff, T. H.; Bent, B. E. *J. Phys. Chem.* **1992**, *96*, 1836.

(28) Zhou, X.-L.; White, J. M. *Chem. Phys. Lett.* **1987**, *142*, 376.

(29) Henderson, M. A.; Mitchell, G. E.; White, J. M. *Surf. Sci.* **1987**, *184*, L325.

(30) Zhou, X.-L.; White, J. M. *Surf. Sci.* **1991**, *241*, 270.

(31) Henderson, M. A.; Mitchell, G. E.; White, J. M. *Surf. Sci.* **1991**, *248*, 279.

(32) Zhou, Y.; Henderson, M. A.; Feng, W. M.; White, J. M. *Surf. Sci.* **1989**, *224*, 386.

(33) Zaera, F.; Hoffmann, H. *J. Phys. Chem.* **1991**, *95*, 6297.

(34) Zaera, F. *Surf. Sci.* **1992**, *262*, 335.

(35) Chiang, C.-M.; Bent, B. E. *Surf. Sci.* **1992**, *279*, 79.

(36) Solymosi, F.; Revesz, K. *Surf. Sci.* **1993**, *280*, 38.

(37) Zhou, X.-L.; Solymosi, F.; Blass, P. M.; Cannon, K. C.; White, J. M. *Surf. Sci.* **1989**, *219*, 294.

(38) Chen, J. G.; Beebe, T. P.; Crowell, J. E.; Yates, J. T., Jr. *J. Am. Chem. Soc.* **1987**, *109*, 1726.

(39) Dyer, J. S.; Thiel, P. A. *Surf. Sci.* **1990**, *238*, 169.

(40) Castro, M. E.; Pressley, L. A.; Kiss, J.; Pylant, E. D.; Jo, S. K.; Zhou, X.-L.; White, J. M. *J. Phys. Chem.* **1993**, *97*, 8476.

(41) Jones, R. G.; Singh, N. K. *Vacuum* **1988**, *38*, 213.

(42) Armentrout, D. D.; Grassian, V. H. *Langmuir* **1994**, *10*, 2071.

(43) Liu, Z.-M.; Zhou, X.-L.; Kiss, J.; White, J. M. *Surf. Sci.* **1993**, *286*, 233.

(44) Sun, Z.-J.; Schwaner, A. L.; White, J. M. *Chem. Phys. Lett.* **1994**, *219*, 118.

(45) Madey, T. E. *Science* **1986**, *234*, 316.

(46) Walczak, M. M.; Johnson, A. L.; Thiel, P. A.; Madey, T. E. *J. Vac. Sci. Technol. A* **1988**, *6*, 675.

(47) Alvey, M. D.; Yates, J. T., Jr.; Uram, K. J. *J. Chem. Phys.* **1987**, *87*, 7221.

(48) Alvey, M. D.; Yates, J. T., Jr. *J. Am. Chem. Soc.* **1988**, *110*, 1782.

(49) Joyce, S. A.; Johnson, A. L.; Madey, T. E. *J. Vac. Sci. Technol. A* **1989**, *7*, 2221.

(50) Joyce, S. A.; Yarmoff, J. A.; Madey, T. E. *Surf. Sci.* **1991**, *254*, 144.

(51) Joyce, S. A.; Clark, C.; Chakarian, V.; Shuh, D. K.; Yarmoff, J. A.; Madey, T. E.; Nordlander, P.; Maschhoff, B.; Tao, H.-S. *Phys. Rev. B* **1992**, *45*, 14264.

(52) Johnson, A. L.; Joyce, S. A.; Madey, T. E. *Phys. Rev. Lett.* **1988**, *61*, 2578.

(53) Madey, T. E.; Nair, L.; Diebold, U.; Shivaprasad, S. M.; Johnson, A. L.; Poradzisz, A.; Shinn, N. D.; Yarmoff, J. A.; Chakarian, V.; Shuh, D. In *Desorption Induced by Electronic Transitions DIET V*; A. R. Burns, E. B. Stechel and D. R. Jennison, Ed.; Springer-Verlag: Berlin, 1993; Vol. 31; pp 182.

(54) Madey, T. E.; Joyce, S. A.; Yarmoff, J. A. In *Chemistry and Physics of Solid Surfaces VIII*; R. Vanselow and R. Howe, Ed.; Springer-Verlag: Berlin, 1990; Vol. 22; pp 55.

(55) Rye, R. R.; Kelber, J. A. *Appl. Surf. Sci.* **1987**, *29*, 397.

(56) Rye, R. R. *J. Polym. Sci., Polym. Phys.* **1988**, *26*, 2133.

(57) Rye, R. R.; Arnold, G. W. *Langmuir* **1989**, *5*, 1331.

(58) Rye, R. R.; Martinez, R. J. *J. Appl. Polym. Sci.* **1989**, *37*, 2529.

(59) Rye, R. R.; Shinn, N. D. *Langmuir* **1990**, *6*, 142.

(60) Rye, R. R. *Langmuir* **1990**, *6*, 338.

(61) Rye, R. R.; Chi, K.-M.; Hampden-Smith, M.; Kodas, T. T. *J. Electrochem. Soc.* **1992**, *139*, L60.

(62) Rye, R. R.; Knapp, J. A.; Chi, K.-M.; Hampden-Smith, M. J.; Kodas, T. T. *J. Appl. Phys.* **1992**, *72*, 5941.

(63) Rye, R. R. *J. Polym. Sci., Polym. Phys.* **1993**, *31*, 357.

(64) Rye, R. R.; Ricco, A. J. *J. Electrochem. Soc.* **1993**, *140*, 1763.

(65) Rye, R. R.; Arnold, G. W.; Ricco, A. J. *J. Electrochem. Soc.* **1993**, *140*, 3233.

(66) Wheeler, D. R.; Pepper, S. V. *J. Vac. Sci. Technol. A* **1990**, *8*, 4046.

(67) Hampden-Smith, M. J.; Kodas, T. T.; Rye, R. R. *Adv. Mater.* **1992**, *4*, 524.

(68) Saperstein, D. D.; Lin, L. J. *Langmuir* **1990**, *6*, 1522.

(69) Simons, J. K.; Frigo, S. P.; Taylor, J. W.; Rosenberg, R. A. *J. Vac. Sci. Technol. A* **1994**, *12*, 681.

(70) Lee, T.-H. D. *J. Vac. Sci. Technol. A* **1991**, *9*, 1287.

(71) Lee, H. J.; Zubeck, R.; Hollars, D.; Lee, J. K.; Chao, A.; Smallen, M. *J. Vac. Sci. Technol. A* **1993**, *11*, 711.

(72) Vurens, G. H.; Gudeman, C. S.; Lin, L. J.; Foster, J. S. *Langmuir* **1992**, *8*, 1165.

(73) Kiss, J.; Alberas, D. J.; White, J. M. *Surf. Sci.* **1992**, *275*, 82.

CHAPTER II. THERMALLY-INDUCED AND ELECTRON-INDUCED CHEMISTRY OF CF_3I ON Ni(100)

A paper accepted by the Journal of the American Chemical Society

Mark B. Jensen and Patricia A. Thiel

Abstract

We have investigated the thermally-induced and electron-impact-induced chemistry of CF_3I on Ni(100) following adsorption at 100 K. The data support a model for the thermally-induced chemistry, in which CF_3I dissociates to CF_3 and I, either upon adsorption or at slightly-elevated temperatures. Most CF_3 decomposes to adsorbed C and F. Above 75% saturation of the first layer, the availability of surface sites for decomposition decreases to a level where some adsorbed CF_3 remains intact and desorbs as such. Bombardment of multilayer CF_3I by low-energy electrons introduces new chemistry. Electron-induced decomposition (EID) of the parent molecule occurs through both C-I and C-F bond scission, with a measured cross-section of 1.5×10^{-16} cm^2 (upper limit). Thermally-induced desorption from the electron-bombarded surface indicates a number of EID fragment reactions, most notably carbon-carbon bond formation, as evidenced by $C_2F_3I^+$, $C_2F_4^+$, $C_2F_5^+$, $C_3F_5^+$, and $C_4F_7^+$. To our knowledge, this is the first report of C-C bond formation in small fluorocarbons adsorbed on metal surfaces.

1. Introduction

The interaction of fluorocarbons with surfaces is fundamentally important in a wide variety of applications, from lubrication in the aerospace and magnetic media industries,[1,2] to fluorocarbon etching of electronic devices.[3-5] Furthermore, interactions of low-energy electrons with fluorocarbons are important in a number of surface-related processes. For instance, electron-impact events in fluorocarbon discharges lead to CF_x radical formation and, depending on the components of the discharge, eventual selective etching of Si or SiO_2.[5] Also, it has been reported that low-energy electrons or UV-induced photoelectrons cause increased adhesion of perfluoropolyether lubricants to several substrates through cross-linking of the polymer chains.[6] This has proven especially beneficial in computer disk lubrication, where lubricant-metal bonding is critical because of high disk rotation speeds.[2,7] Polymer chain cross-linking has also been reported after electron irradiation of polytetrafluoroethylene (Teflon).[8] This same effect has been noted for photon irradiation, and is thought to be initiated by low-energy valence excitations resulting from secondary electrons.[9]

In spite of the importance of the topic, only one study to date has sought to clarify the interaction of low-energy electrons with small fluorocarbons adsorbed on a surface.[10] There, no evidence is reported for C-C bond formation (the fundamental step in cross-linking). The present paper deals with the electron-induced chemistry of CF_3I on Ni(100), establishing first the thermally-induced chemistry as a baseline. We find clear evidence for C-C coupling, but only after irradiation of the condensed

multilayer. This may be a first step toward understanding cross-linking induced by electron bombardment of polymers.

2. Experimental Description

The experiments are performed in a previously described stainless steel vacuum chamber with a base pressure of 6 x 10^{-11} Torr.[11] Briefly, the chamber is equipped for Auger electron spectroscopy (AES), thermal desorption mass spectrometry (TDS), electron-stimulated desorption ion angular distribution (ESDIAD), low-energy electron diffraction (LEED), and gas introduction.

The disk-shaped Ni(100) single crystal, 1 mm thick and 9 mm in diameter, is spotwelded to two tapered tantalum rods for efficient resistive heating, and is in thermal contact with a liquid nitrogen-coolable cold finger. Temperature is monitored with a W5%Re-W26%Re thermocouple spotwelded to the back of the crystal.

Initial cleaning of the freshly prepared Ni(100) single crystal is described elsewhere.[12] Major contaminants detected by AES are carbon, oxygen, and sulfur. Sulfur and oxygen are removed by argon ion bombardment, while small exposures of O_2 (0.3-0.7 L), followed by annealing at 1000 K serve to deplete the surface of residual carbon. Before each experiment the crystal is argon ion bombarded for 10-15 minutes to deplete the surface of sulfur and undesorbed iodine from CF_3I. This is followed by low exposures of O_2 at 300 K and 20-60 s anneals at 1000 K until the surface is clean, as determined by AES. AES peaks at 146 and 180 eV were originally attributed to residual sulfur and chlorine, respectively. Attempts to

eliminate these peaks by excessive ion bombardment were unsuccessful. However, if the AES signal is collected at a crystal temperature of 900 K, these peaks disappear, and are, therefore, determined to be electron diffraction peaks common to well-ordered Ni(100) surfaces.[13]

TDS experiments are performed using a UTI 100C quadrupole mass spectrometer (QMS) interfaced to a personal computer, thereby allowing simultaneous monitoring of up to eight masses. A feedback circuit in the design of Herz *et al.*[14] is used for control of the heating rate. For all TDS experiments, except where otherwise noted, the heating rate is 4 K/s to 250 K, and 2 K/s to 1200 K. Exposure is carried out at 100 K.

In order to reduce stray electron current from the QMS ionizer to the crystal, three electrostatic lenses with 8 mm apertures separate the crystal from the ionizer. The lens closest to the ionizer is held at +5 V, while the middle lens is held at -55 V. The lens closest to the sample, and sample, are grounded, with the distance from the crystal to the front of the ionizer being approximately 1.5 cm. In this configuration, stray electron current at the sample is reduced by 95%, from 2.8 μA to 100 nA.

The ionizer of the QMS is used as the electron source for studying the effects of low-energy electrons on the CF_3I chemistry. After dosing CF_3I, the sample is moved to the TDS position. The voltage bias is removed from the two electrostatic lenses closest to the ionizer, and a bias of +40 V is applied to the crystal. The ionizer emission current is 3.0 mA, resulting in a current from crystal to ground measured at approximately 6 μA. This current is used as an estimate of the electron

flux incident on the crystal, although it is not corrected for secondary electron emission and is, therefore, a lower limit. The maximum incident electron energy is 110 eV.

CF_3I is purchased from PCR Inc. which specifies 99.0% purity. Several freeze-pump-thaw cycles are carried out under vacuum with liquid nitrogen for further purification. CF_3I is introduced into the chamber through a directional gas doser, consisting of a 2 μm diameter conductance-limiting aperture in series with a collimating aperture. The crystal is positioned approximately 0.5 cm from the doser end. Pressure in the doser line is 25-30 Torr, measured with a capacitance manometer. Exposures are reported in experimental units of Torr-s, or in relative units which give the percentage of the exposure required to saturate the decomposition products (notably iodine). Cracking of CF_3I in the QMS results in the following relative intensities: CF_3^+(1.00), CF_3I^+(0.89), I^+(0.78), CF_2^+(0.11), CF^+(0.08). These intensities are close to the standard reference fragmentation pattern of CF_3I^+(1.00), I^+(0.96), CF_3^+(0.77), CF^+(0.12), CF_2^+(0.07).[15] We also establish the fragmentation pattern of CF_n species in situ by monitoring known CF_2 and CF_3 desorption states from CF_3I decomposition on Ru(001).[16] In this way, it is determined that the relative intensities of CF_3^+, CF_2^+, and CF^+ from CF_3 are 0.42, 1.00, and 0.45, respectively, while those of CF_2^+ and CF^+ from CF_2 are 1.00 and 0.86. These ratios differ from those reported previously by our laboratory,[16] because the QMS is retuned for the present experiments to maximize sensitivity for high masses (>40 amu).

3. Results

3.1 Thermal chemistry of CF_3I on Ni(100)

Figure 1 shows the yield of three main fragment ions, derived from three main desorbates, as a function of exposure. Evidence of C-I bond cleavage is given by the presence of an atomic iodine desorption state, represented by I^+ in fig. 1. Figure 2 shows the I^+ (m/z = 127) desorption traces with increasing CF_3I exposure. The peak temperature shifts from 1130 K at the lowest exposure to 1085 K at highest exposure, indicative of adsorbate-adsorbate repulsive interactions and similar to atomic iodine desorption from Ru(001).[16] As shown in the top panel of fig. 1, the area under the I^+ curve grows monotonically with increasing exposure until reaching a saturation level at approximately 4000 Torr-s. Above this exposure, defined as 100% saturation-exposure, only the CF_3I multilayer state grows. At exposures approaching saturation and beyond, a small feature is seen in the I^+ signal at 885 K. We believe neither state of I^+ can originate from NiI_2 or IF, since no NiI^+ or IF^+ is detected.

Figure 3 shows the CF_3I^+ (m/z = 196) desorption traces at selected exposures. No sharp monolayer peak is evident. Instead, at 2000 Torr-s, or 50% saturation, a broad feature appears between 150 K and 350 K. At 60% saturation this feature intensifies and gives the appearance of a doublet, one peak at 180 K, the other at approximately 270 K. Above this exposure a sharp desorption state appears at 150 K and increases in intensity with all exposures thereafter, as shown in the inset of fig. 3 and in the bottom panel of fig. 1. This state is attributed to CF_3I multilayers. It should be noted that the broad feature between 150 K and 350 K, although not

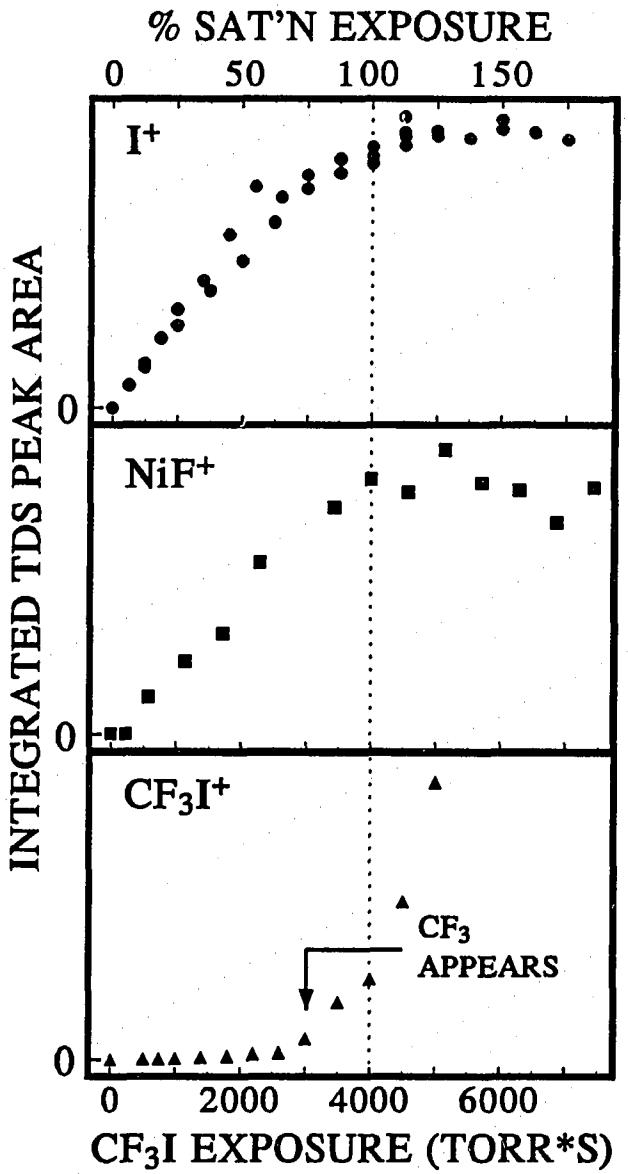

Figure 1. Integrated TDS peak area vs. CF_3I exposure for CF_3I^+, NiF^+, and I^+. Saturation of C-I bond cleavage occurs at 4000 Torr-s. A CF_3 desorption state appears at 3000 Torr-s.

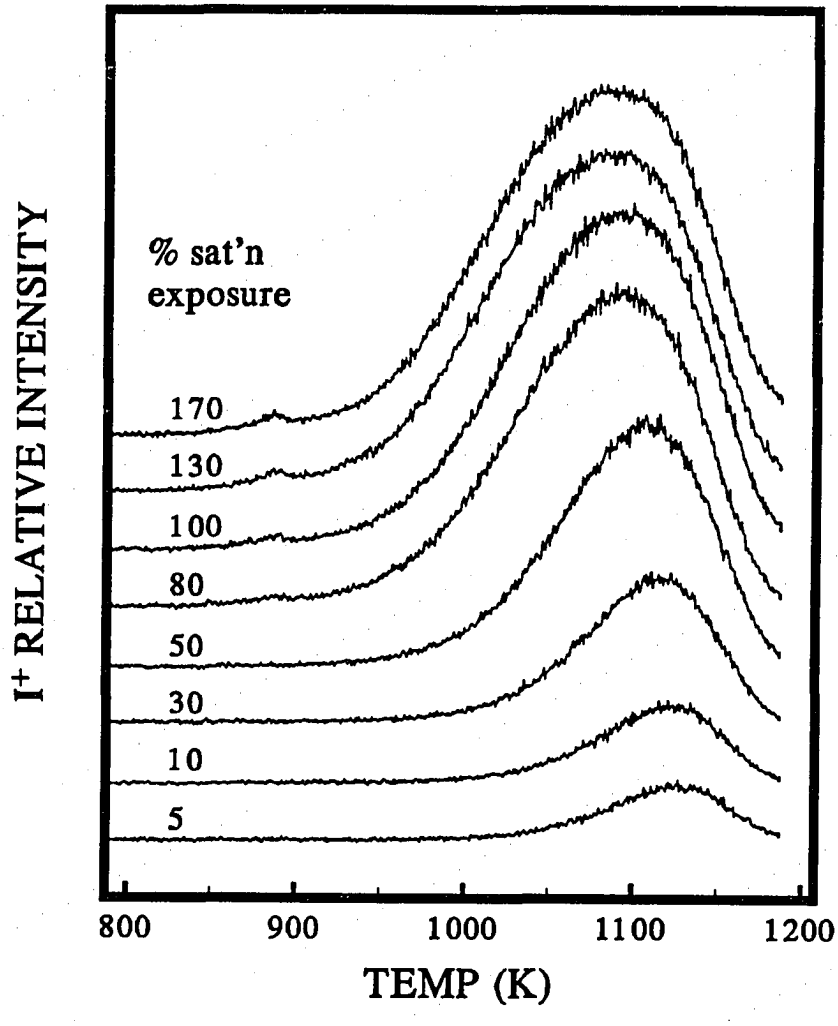

Figure 2. I^+ (m/z = 127) TDS signal for increasing exposures of CF_3I on Ni(100). A 4000 Torr-s exposure corresponds to saturation.

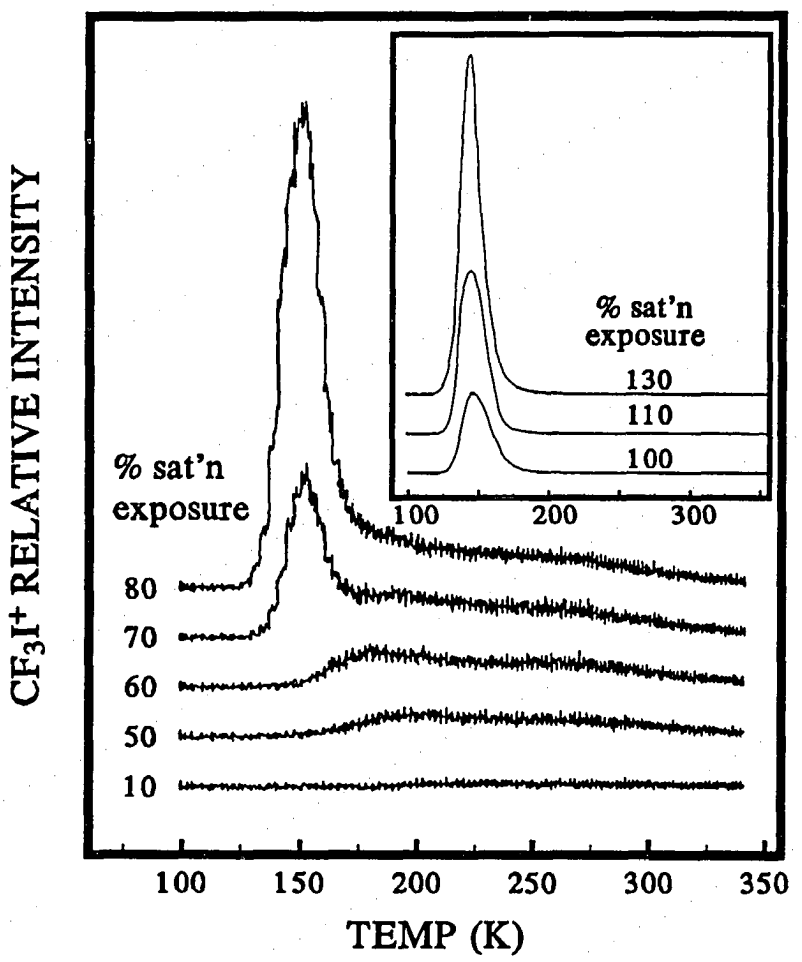

Figure 3. CF_3I^+ (m/z = 196) TDS signal for increasing exposures of CF_3I on Ni(100). The heating rate for exposures below saturation is 2 K/s, as opposed to the usual 4 K/s for this temperature range, in an attempt to resolve possible multiple molecular desorption states. For exposures at saturation and above, shown in the inset, the heating rate is 4 K/s.

visible because of the scale of the inset in fig. 3, remains as a high temperature foot on the multilayer peak at all high exposures.

Carbon-fluorine bond scission is indicated by NiF_2 desorption at 885 K, concurrent with the low-temperature I^+ state. Ni^+, NiF^+, and NiF_2^+ are detected for all naturally occurring Ni isotopes, providing unambiguous determination of the parent species as NiF_2. Desorption traces of the strongest cracking fragment, $^{58}NiF^+$ (m/z = 77), are shown in fig. 4. There is no shift in the peak desorption temperature with increasing exposure. The middle panel of fig. 1 shows the NiF^+ desorption peak area vs. CF_3I exposure. The NiF_2 state appears shortly after atomic iodine, and grows monotonically, saturating along with atomic iodine at 4000 Torr-s.

Figure 5 shows desorption traces in the temperature range 200-500 K for the major cracking fragments of CF_3I after a saturation exposure. At 340 K, a small peak exists in the CF_2^+ signal. Also at this temperature, a small rise above baseline is evident in the CF^+ signal. A small CF_3^+ peak may be discernible, but examination of similar data shows its existence never to be obvious. Because the CF_2^+ signal for this state is approximately twice that of CF^+, and based on the cracking patterns established in Section 2, we attribute this state to a small amount of CF_3 desorption. This feature first appears at an exposure of approximately 75% saturation, and is detected at all exposures thereafter, although always visible only slightly above the baseline.

The rapidly decreasing CF_3I^+ and CF_3^+ signals shown between 200 K and 300 K in fig. 5 are interpreted as the high temperature CF_3I foot coming off the large

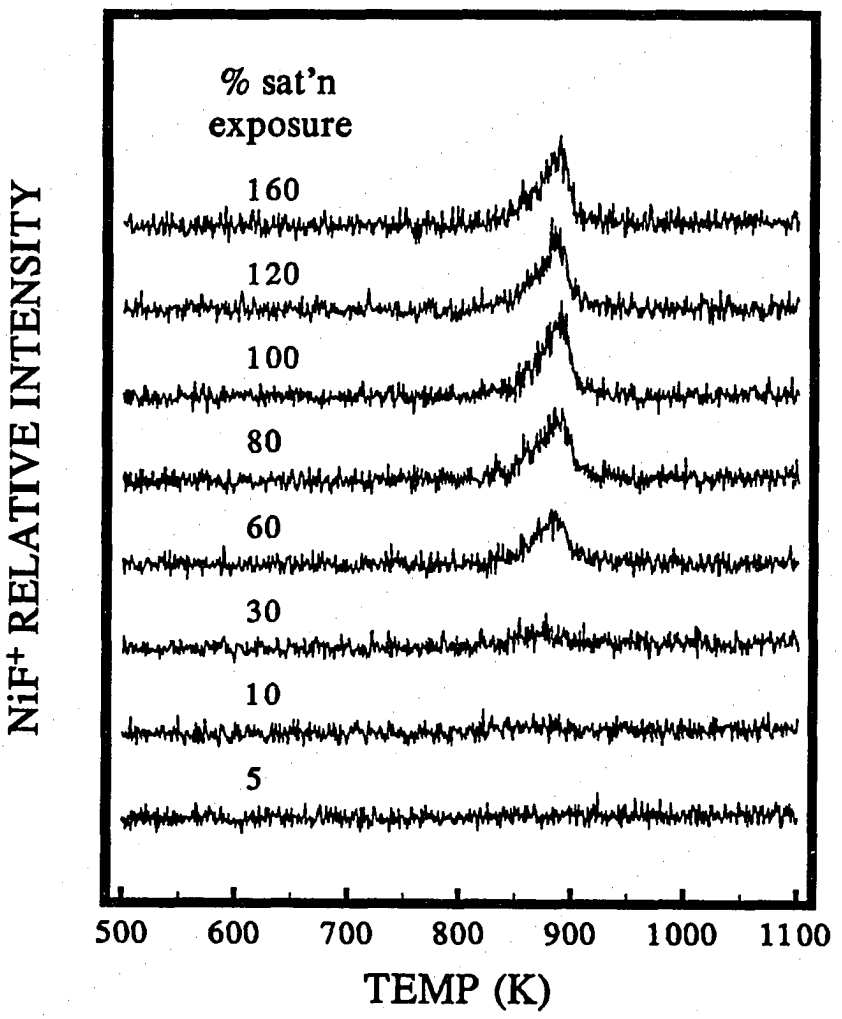

Figure 4. NiF^+ (m/z = 77) TDS signal, representing NiF_2 desorption, for increasing exposures of CF_3I on Ni(100) at 100 K.

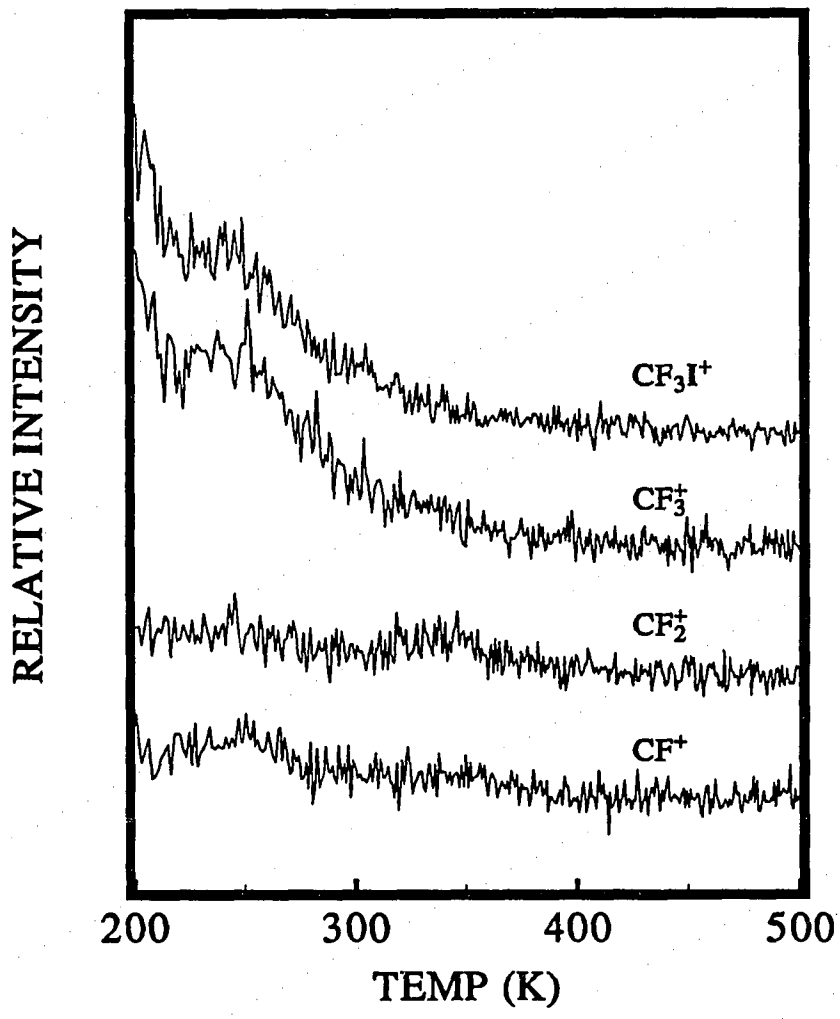

Figure 5. TDS spectra for CF_3I^+ (m/z = 196), CF_3^+ (m/z = 69), CF_2^+ (m/z = 50), and CF^+ (m/z = 31) for a saturation exposure, 4000 Torr-s, of CF_3I.

multilayer peak. Also in this temperature range, peaked at 250 K, a small CF^+ feature is visible, but too large to be due to QMS fragmentation of CF_3I. Since the absence of a corresponding CF_2^+ peak of similar height makes it impossible to attribute this state to CF_2 or CF_3I desorption (cf. Sec. 2), we believe it is due to a small amount of CF desorption. It is visible at all exposures equal to and above 90% saturation. We believe this small CF state originates from electron beam damage to CF_3I multilayers (cf. Section 3.2). Even though our electrostatic lens configuration limits the amount of stray electron current at the crystal, some current is still measured. If the ionizer of the QMS is left off until 200 K during TDS of a saturation exposure of CF_3I, this small CF^+ peak is not seen.

3.2 Electron-induced chemistry of CF_3I on Ni(100)

As shown in fig. 6, CF_3I multilayers are very susceptible to EID. Figure 6 shows the CF_3I^+ (m/z = 196) TDS signal from a 5000 Torr-s CF_3I exposure after various low-energy ($E_i \leq 110$ eV) electron fluences at 100 K. The decreasing peak area indicates that CF_3I is consumed via EID.

The kinetic behavior of EID in multilayer CF_3I can be modeled as a first-order process,

$$-d[CF_3I]/dt = k[CF_3I] \qquad (1)$$

where $[CF_3I]$ is the concentration of adsorbed CF_3I. The first-order rate constant, k, can be expressed:

$$k = (i_e/eA)\sigma_{EID} = \text{flux} \cdot \sigma_{EID} \qquad (2)$$

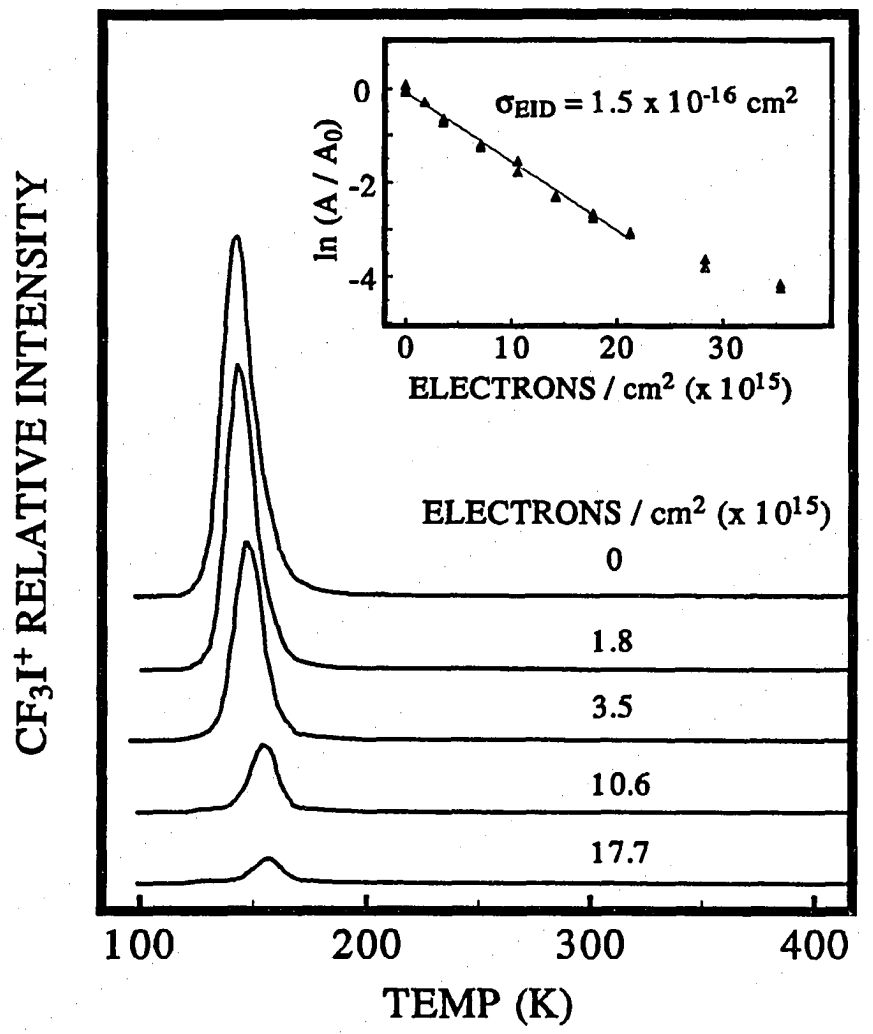

Figure 6. CF_3I^+ TDS signal from a 5000 Torr-s CF_3I exposure after increasing levels of electron fluence. Decreasing peak intensity indicates EID. The inset shows the linear relationship between $\ln(A/A_0)$ and electron fluence, resulting in σ_{EID} = 1.5 x 10^{-16} cm^2.

where i_c is the current measured at the crystal, e is the electron charge, A is the surface area of the crystal, and σ_{EID} is the EID cross-section. Equation (1) can then be solved to yield:

$$\ln(A_t/A_0) = -(i_c/eA)\sigma_{EID}t = -F_e\,\sigma_{EID} \qquad (3)$$

where F_e is the total electron fluence, A_t is the area under the TDS peak corresponding to t seconds of electron exposure, and $A_t/A_0 = [CF_3I]_t/[CF_3I]_0$. A plot of $\ln(A_t/A_0)$ vs. F_e is shown in the inset of fig. 6. A slight deviation from linearity occurs at high electron fluences, probably due to inhibited EID from surface fragments--an effect reported previously for CF_3Cl on Pt(111).[10] From the plot in fig. 6, the cross-section for EID, σ_{EID}, is calculated to be 1.5×10^{-16} cm^2. This value must be considered an upper limit since i_c is not completely corrected for secondary electron emission.

Products of electron-stimulated desorption (ESD) can be detected with the QMS during electron bombardment. The results of a 2 min electron bombardment at 100 K on a 5000 Torr-s CF_3I exposure are shown in fig. 7. A bias of +40 V is applied to the crystal after 15 s to initiate the experiment. Species detected are F^+, HF^+, CF_n^+(n = 1-3), I^+, and a small amount of CF_3I^+. HF^+ is probably the result of recombination in the QMS ionizer of fluorine from fluorinated ESD products and background H_2. Atomic fluorine is the dominant ESD product, which is not surprising, given the well-known susceptibility of fluorine to ESD.

A substantial amount of C-I bond scission results from electron bombardment. During irradiation, the QMS detects I^+, along with CF_n fragments. Most of the

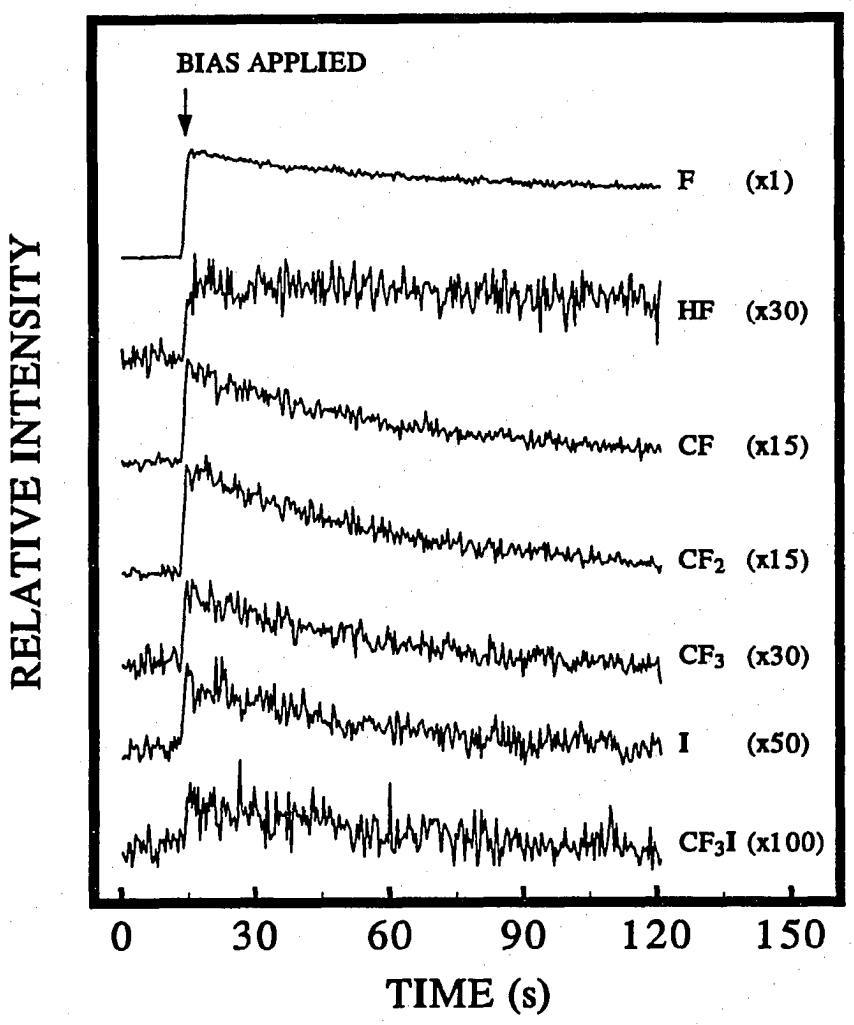

Figure 7. Species detected during EID after a 5000 Torr-s CF_3I exposure at 100 K. The electron flux is 5.89 x 10^{13} electrons s^{-1} cm^{-2}, and a 120 s dose corresponds to a fluence of 7.1 x 10^{15} electrons/cm^2.

atomic iodine created as a result of electron-induced C-I bond scission is retained on the crystal surface. This is shown by TDS following electron bombardment; I^+ peak areas are plotted vs. electron fluence in fig. 8. C-I bond scission occurs rapidly at first, leveling off after 20-25 x 10^{15} electrons/cm^2. Upon electron irradiation, the small I^+ feature at 885 K intensifies along with the main I^+ state, while the NiF^+ feature at this same temperature remains constant (data not shown).

As reported below, we observe C-C bond formation products in post-EID TDS of CF_3I on Ni(100), yet we detect no $C_2F_3^+$ (m/z = 81), $C_2F_4^+$ (m/z = 100), $C_2F_5^+$ (m/z = 119), or $C_3F_5^+$ (m/z = 131) *during* electron bombardment.

A variety of decomposition products desorb during post-EID TDS. Figure 9 shows C_xF_yI desorption states from a 5000 Torr-s CF_3I dose at increasing levels of electron fluence, (i) to (vi). Two states can be seen in the CF_2I^+ (m/z = 177) spectrum of fig. 9A. The state at 150 K, overranged at low fluences, is due to molecular CF_3I, as shown previously in fig. 6. At 200 K, a second state emerges, initially increasing with electron dose, then decreasing back to baseline level. No corresponding CF_3I^+ is visible. Therefore, we attribute this new desorption state to CF_2I, formed from CF_3I by electron-induced C-F bond cleavage. Finally, in data not shown, a small CFI state can be identified at 240 K, which appears and intensifies after the CF_2I state is in decline, then itself disappears. Thus, the three CF_xI species (x = 3, 2, 1) undergo sequential population and loss under the influence of the electron beam, as illustrated in fig. 10; note also the desorption at progressively higher temperatures (150, 200, 240 K).

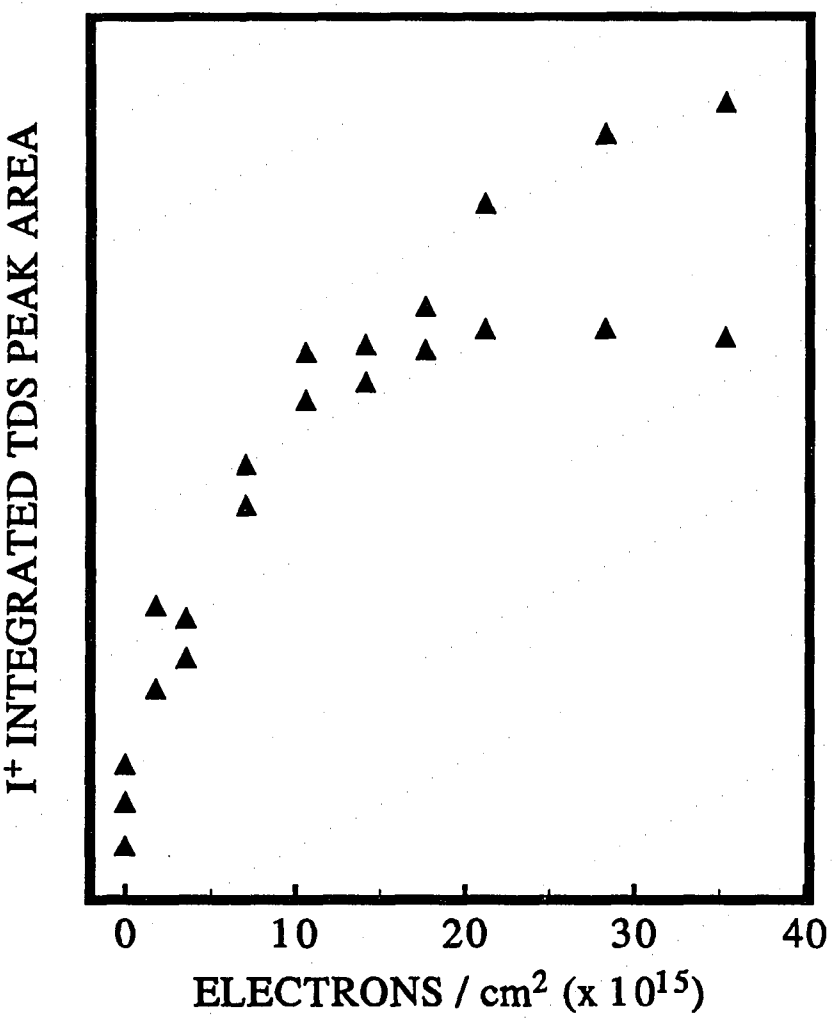

Figure 8. Integrated I^+ desorption peak area vs. electron fluence for a 5000 Torr-s CF_3I exposure. The two curves represent two sets of experiments.

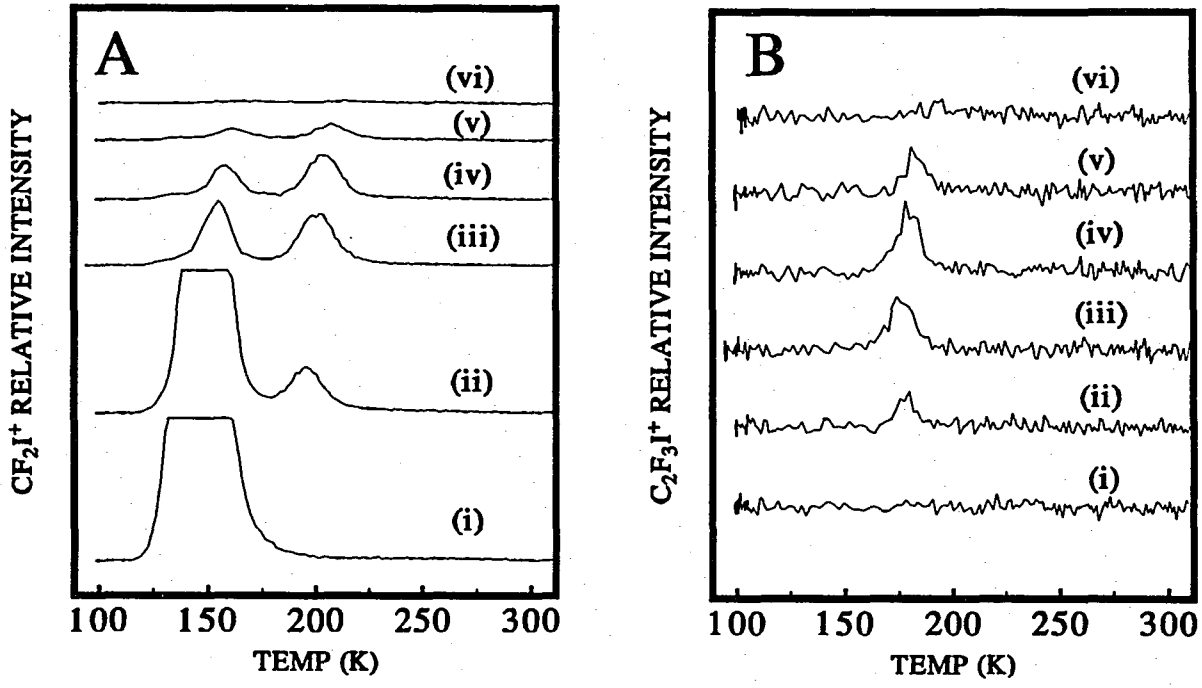

Figure 9. TDS signal for: (A) CF_2I^+, and (B) $C_2F_3I^+$, after electron fluences of: (i) 0, (ii) 3.5 x 10^{15}, (iii) 17.7 x 10^{15}, (iv) 24.7 x 10^{15}, (v) 35.3 x 10^{15}, and (vi) 70.7 x 10^{15} electrons/cm^2, after a 5000 Torr-s CF_3I exposure at 100 K.

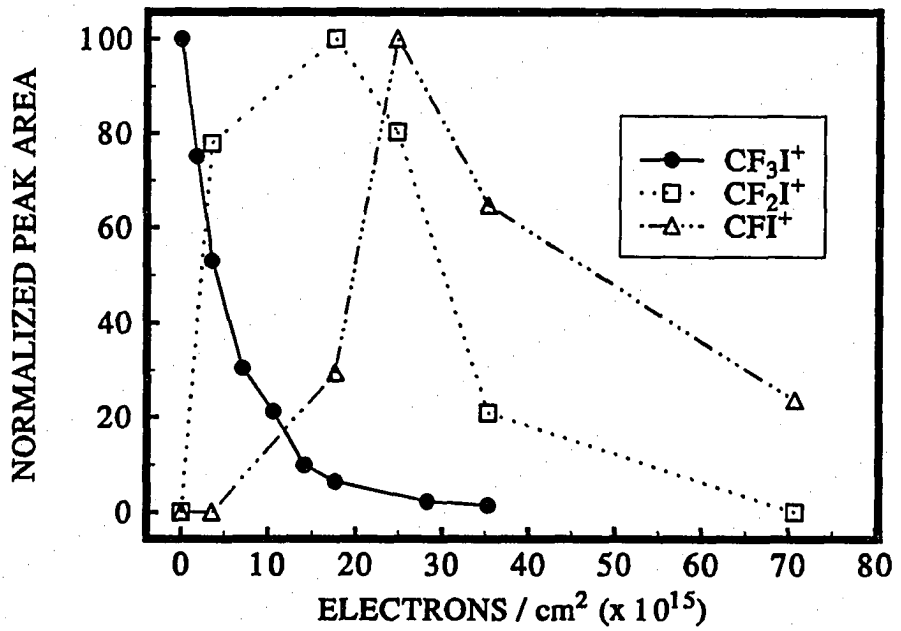

Figure 10. Yield of various species in TDS as a function of initial electron fluence at low temperature.

A similar rise and fall, paralleling that of CF_2I, is seen in the $C_2F_3I^+$ (m/z = 208) signal at 180 K, shown in fig. 9B. Masses higher than 208 are not observed for this state. Candidate parent ions for this new species are C_2F_5I, C_2F_4I, and C_2F_3I. However, the mass spectrometer fragmentation pattern of C_2F_5I shows $C_2F_5I^+$ (m/z = 246) as the largest peak, with no perceptible $C_2F_3I^+$;[17] one would expect a similar pattern for C_2F_4I. Therefore, we can eliminate the first two species from consideration and attribute the state at 180 K to C_2F_3I. An independent measurement of the C_2F_3I cracking pattern is consistent with this assignment.[17] The formation of this product, as well as others (below), entails C-C bond formation.

Several new electron-induced features are also evident from the CF_x (x = 1-3) TDS results, shown in fig. 11 with increasing electron fluence. Sharp peaks at 150 K and 200 K in the CF^+ spectrum of fig. 11A correspond to CF_3I and CF_2I, respectively, as described above. Consistent with this assignment, both peaks are evident in the CF_2^+ spectrum of fig. 11B, while the CF_3^+ spectrum of fig. 11C shows only the CF_3I state.

At 250 K, peaks arise in the CF^+ and CF_3^+ spectra. Assignment of this state to one desorbing species is difficult since no CF_2^+, and no higher masses, are detected at this temperature. In mass spectral cracking of CF_4(g), CF_3^+ is the main fragment, with no detectable CF_4^+, and very little CF_2^+ or CF^+.[15] As discussed in Section 2, if CF_2(g) were detected, CF_2^+ and CF^+ would be of roughly equal intensity. Therefore, we attribute the peaks at 250 K in the CF_3^+ and CF^+ spectra to reaction-limited CF_4 and CF.

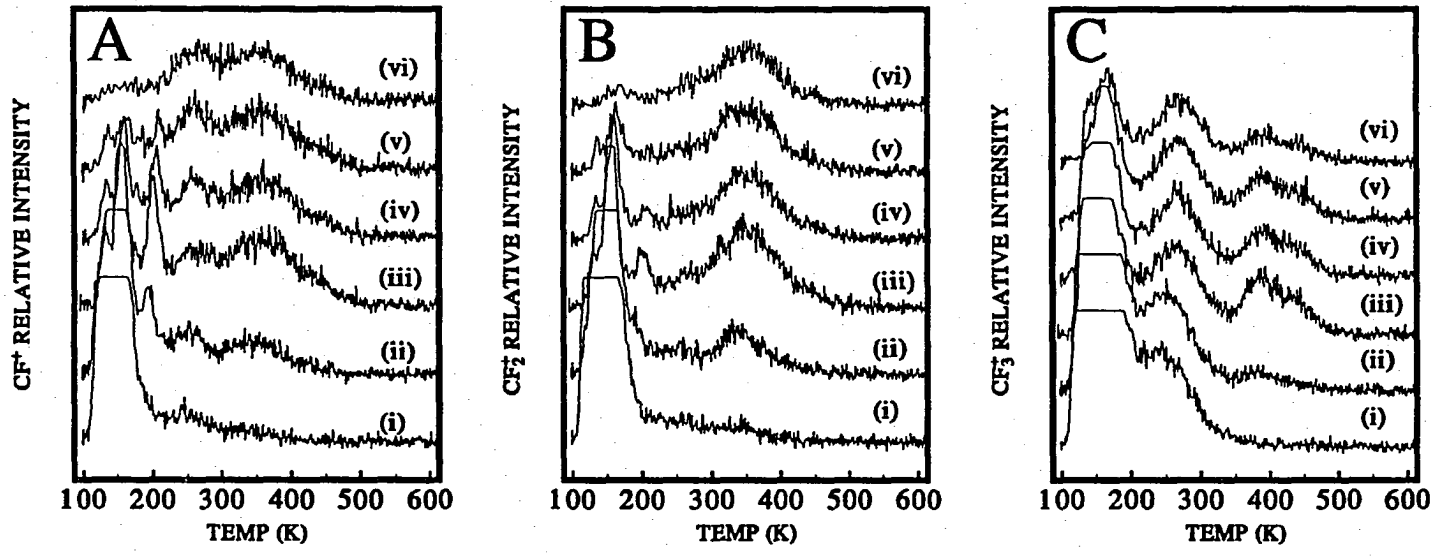

Figure 11. TDS signal for: (A) CF^+, (B) CF_2^+, and (C) CF_3^+ after electron fluences of: (i) 0, (ii) 3.5×10^{15}, (iii) 17.7×10^{15}, (iv) 24.7×10^{15}, (v) 35.3×10^{15}, and (vi) 70.7×10^{15} electrons/cm^2, after a 5000 Torr-s CF_3I exposure.

A broad desorption state, centered at 350 K, can be seen in the CF^+ and CF_2^+ spectra. Since the two masses generate approximately equal signals at this temperature, we can attribute this state to CF_2 desorption. It is interesting to note that, as described above, in the absence of low-energy electrons, high exposures of CF_3I react on Ni(100) to give a CF_3 desorption state at this same temperature, 350 K.

Another broad state can be seen, this time in the CF_3^+ spectrum of fig. 11C. Its onset is at 340 K, peaking at 400 K, and extending to 500 K. The state appears to be a superposition of two peaks, one peaked at 400 K, the other at 450 K. We attribute this state to products of electron-induced C-C bond formation. Figure 12 shows the major products detected in this same temperature range for a 5000 Torr-s CF_3I exposure bombarded by 17.7×10^{15} electrons/cm^2. CF_3^+ and $C_2F_4^+$ (m/z = 100) are the dominant species detected, followed by $C_3F_5^+$ (m/z = 131), $C_2F_5^+$ (m/z = 119), and $C_4F_7^+$ (m/z = 181). Also detected, but not shown, are small of amounts of $C_3F_6^+$ (m/z = 150), and $C_3F_3^+$ (m/z = 93). All species detected in this temperature range show the same peak shape and the same relative intensity response with respect to electron exposure. This response is shown in fig. 13, represented by $C_2F_4^+$. Initially, the state grows in intensity with increasing electron fluence, peaks at 17.7×10^{15} electrons/cm^2, then decreases with higher electron fluence.

The parent ions corresponding to the state at 340 to 500 K are difficult to identify. We consider two main possibilities: only one species desorbs and we monitor a cracking pattern of that species, or a mixture of products evolves due to a series of reactions triggered by the same slow rate-determining step. In evaluating the first

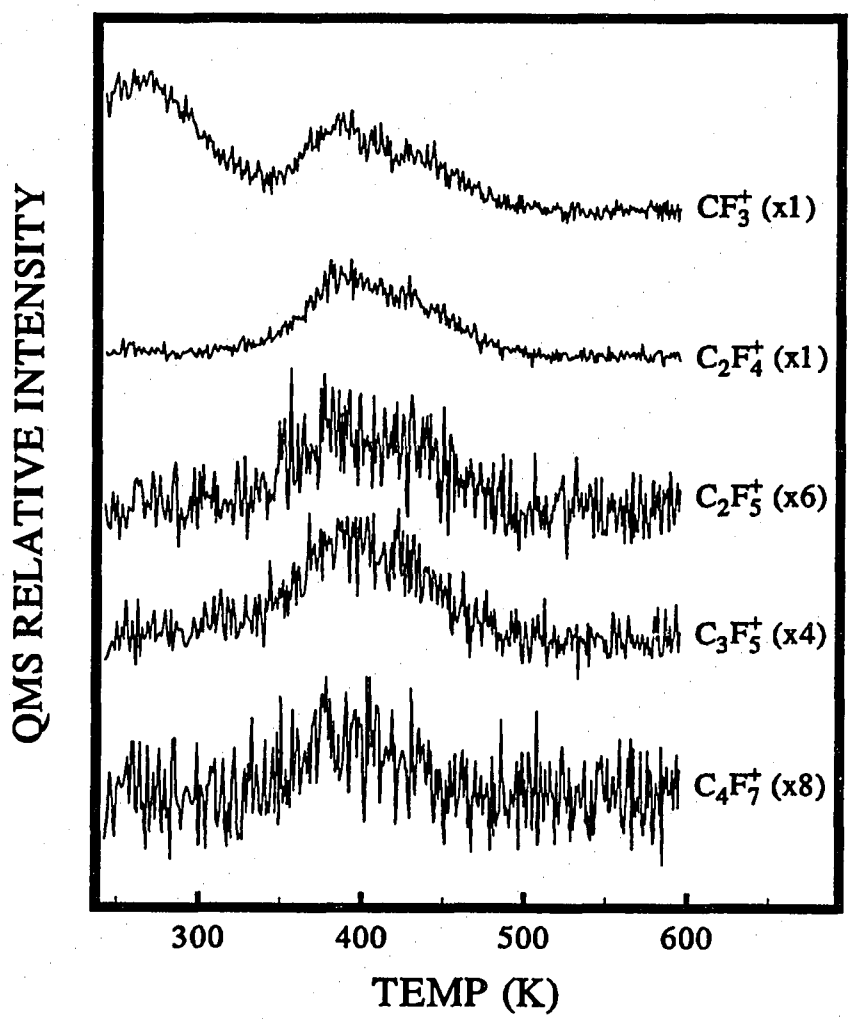

Figure 12. Species with C-C bonds detected after 5000 Torr-s CF_3I exposure, plus EID, at 100 K. The electron fluence is 17.7 x 10^{15} electrons/cm^2.

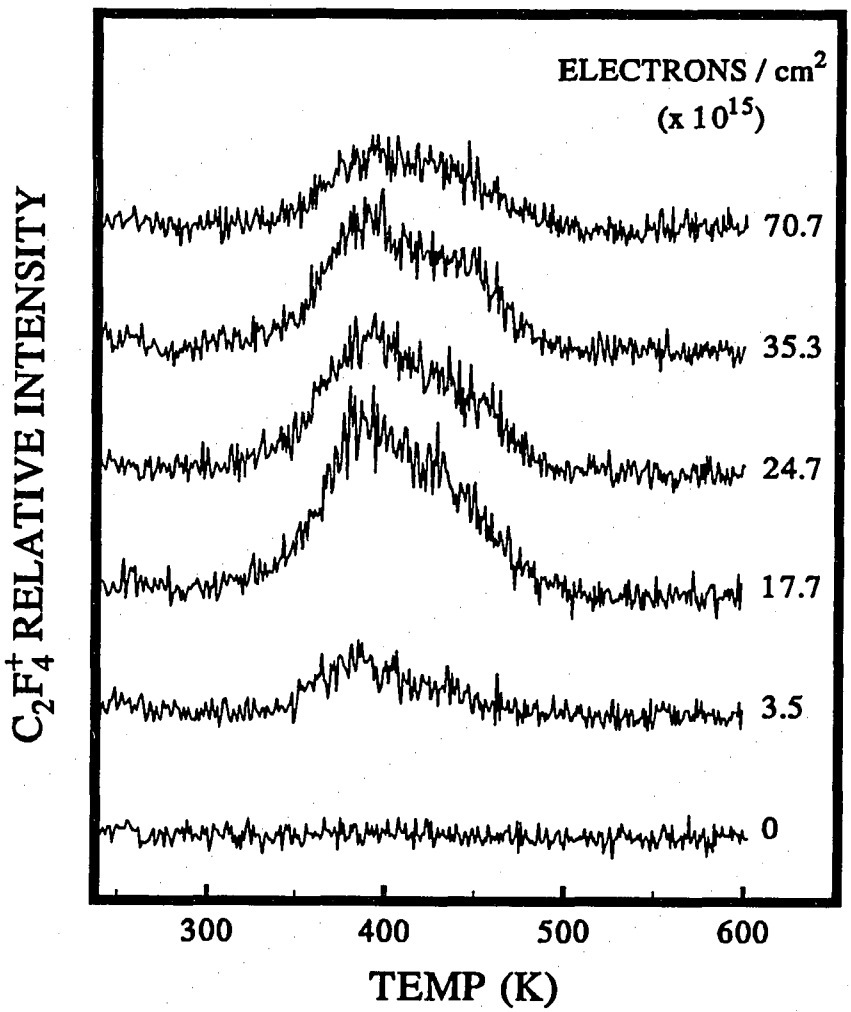

Figure 13. Response of the $C_2F_4^+$ TDS signal to increasing electron fluences. The CF_3I exposure is 5000 Torr-s in each case.

possibility, the relative intensities of the fragment species do not match the published mass spectral cracking patterns of any simple C_1-C_4 fluorocarbons.[15] From fig. 12, the fragmentation ratios are CF_3^+ (1.00), $C_2F_4^+$ (1.00), $C_3F_5^+$ (0.25), $C_2F_5^+$ (0.17), and $C_4F_7^+$ (0.12). It can be seen from fig. 11 that both CF^+ and CF_2^+ extend into this temperature range, but their relative contributions are difficult to estimate. The most intense fragments are CF_3^+ (m/z = 69) and $C_2F_4^+$ (m/z = 100). CF_3^+ is the main fragment in all C_1-C_6 perfluoro-non-cyclic alkanes, but $C_2F_4^+$ is much more rare. It appears as the strongest fragment of perfluorocyclobutane, which is, however, inconsistent with the rest of the fragments we observe.

We postulate, therefore, that a mixture of reaction-limited products desorb between 340 and 500 K (peak at 400 K). These products are the result of two or more reactions initiated by the same rate-determining step, which begins to occur at 340 K. Since we observe no desorption peak temperature shift in the C_n desorbing species, we assume this rate-limiting step is first order. A similar model has been proposed to explain the thermal chemistry of CH_3I on Cu(110).[18] There, evolution of a methane-ethylene mixture in a single first-order state is initiated by slow methyl decomposition to CH_2(ad) and H(ad).

We can use the fragmentation pattern to tentatively identify some of the products. All mass spectral cracking patterns are taken from the same reference.[15] The observation of $C_4F_7^+$ (m/z = 181) and $C_3F_5^+$ (m/z = 131) is especially helpful, as it indicates a perfluoroalkene, C_nF_{2n} (n = 3,4), or a perfluoro-cyclic alkane, C_nF_{2n} (n = 5,6). A mixture of perfluoropropenes, namely 1-hexafluoropropene and 2-methyl-

octafluoropropene, can account best for the appearance and relative intensities of $C_4F_7^+$, $C_3F_6^+$, $C_3F_5^+$, and $C_3F_3^+$ that we observe, along with a portion of the CF_3^+. This leaves only the $C_2F_4^+$, $C_2F_5^+$, and the remainder of the CF_3^+ fragments unexplained.

$C_2F_4^+$ may arise from C_2F_5 radical desorption. Mass spectrometric detection of the C_2F_5 radical, with electron-impact ionization, has been accomplished by monitoring $C_2F_5^+$ (m/z = 119).[19] However, we have been unable to obtain an entire mass spectral fragmentation pattern of this radical. It is not difficult to imagine that the major fragment will result from the loss of one fluorine atom, as has been observed for the CF_3 radical.[16] We note also the thermodynamic stability of the C_2F_5 radical (ΔH_f = -217.3 kcal/mol).[20]

The remainder of the large CF_3^+ signal, as well as a portion of the $C_2F_5^+$ signal, can be attributed to a saturated fluorocarbon, most probably C_2F_6. CF_3^+ is generally the largest fragment in saturated fluorocarbons, e.g. more than twice the size of the next largest, $C_2F_5^+$, in C_2F_6. We can, therefore, postulate that the series of C-C bond formation products desorbing between 350 and 500 K result from rate-determining C_2F_5(ad) activation, followed by formation and desorption of $CF_3CF{=}CF_2$, $CF_3C(CF_3){=}CF_2$ and C_2F_6.

4. Discussion

4.1 Thermal chemistry of CF_3I on Ni(100)

The thermal chemistry of CF_3I on Ni(100) is summed up by the peak area vs. exposure plots shown in fig. 1 for the major desorbing species. Atomic iodine desorption begins at lowest exposure, followed by NiF_2 at 600 Torr-s; both grow monotonically to saturation at 4000 Torr-s. At 75% saturation, 3000 Torr-s, the small CF_3 desorption state appears. Molecular CF_3I rises slowly between 50 and 75%, then grows rapidly with the appearance of the multilayer. It is interesting to note that the multilayer state appears below saturation exposure, indicating multilayer island population before the completion of C-I bond cleavage.

We do not observe a sharp CF_3I peak for a chemisorbed layer, as has been seen for other metals;[16,21,22] instead, there is a very broad molecular CF_3I desorption state between 150 and 300 K. Given the persistence of this state to relatively high temperatures, we speculate that this small feature is due to recombination of adsorbed CF_3 and I, with the CF_3 possibly stabilized by defect sites or slight impurities. Following vacuum breaks, we detect high levels of sulfur contamination and notice a large amount of CF_3 desorption at 350 K after CF_3I exposure, indicating that impurities can stabilize adsorbed CF_3 against dissociation.

Based on the TDS data, a simple model can be developed for the reactions of monolayer CF_3I on Ni(100). CF_3I dissociates to CF_3 and I, either upon adsorption or at slightly-elevated temperatures. In a reaction which probably occurs through impurity- or defect-oriented channels, a small amount of CF_3 recombines with I below

300 K to desorb as CF_3I. (Note that the breadth of this peak suggests unusual recombination kinetics, such as kinetic parameters which vary with coverage or binding site.) However, most CF_3 decomposes to adsorbed C and F. (Although there is a slight difference in the exposures at which I(g) and NiF_2(g) first appear, we can assume that they are both formed at the lowest exposures; it has been documented that low vapor pressure solids, such as NiF_2, are difficult to detect by mass spectrometry due to their high sticking coefficient on chamber surfaces.[18]) At exposures above 75% saturation, the availability of surface sites for decomposition decreases to a level where some adsorbed CF_3 remains intact and desorbs as such. Except for the defect- or impurity-mediated recombination, this model is very similar to that proposed for CH_3I on Ni(100).[23-26]

In our data, the concurrence of NiF_2 and I desorption at 885 K suggests another type of reaction. The I^+ state appears only near saturation, and is very small relative to the main I^+ state at higher temperature. One possible explanation is that adsorbed F and I segregate into separate islands. As coverage reaches saturation, these island boundaries begin to interact. Therefore, when NiF_2 desorbs, the local disruption of the Ni lattice causes desorption of adjacent I. Limiting the reaction to island boundaries accounts for the small size of the I^+ feature at 885 K. While EID produces a higher concentration of I(ad), the NiF_2 concentration remains constant as EID-induced atomic fluorine is ejected into the gas phase. Hence, more I(ad) interacts with the same amount of NiF_2. This is consistent with the increase in the I^+ yield at 885 K resulting from electron bombardment, as well as the unchanged NiF_2

yield.

A comparison of the thermal chemistry of CF_3I, CH_3I,[23-26] and C_2H_5I [27] on Ni(100) indicates that this surface is very effective in activating both C-F and C-H bonds of the simple halocarbons. Ag(111) lies at the other extreme, with no evidence either of C-F or C-H bond cleavage in the simple halocarbons.[21,28] Other metal surfaces, however, are more discriminatory between C-F and C-H bonds. For instance, the reactivity of Ru(001) toward CF_3I is intermediate between that of Ni(100) and Ag(111),[16] whereas Ru(001) is even more active than Ni(100) for CH_3 decomposition.[28,29]

4.2 Electron-induced chemistry of CF_3I on Ni(100)

Efficient EID of multilayer CF_3I occurs on Ni(100) with a cross-section, σ_{EID}, of 1.5×10^{-16} cm^2. We observe two types of products from this process: gaseous species which evolve during electron bombardment; and products which remain at the surface, reacting and/or desorbing during subsequent heating. The main component of the former group is atomic fluorine; lesser amounts of CF_n (n = 1-3), I, and CF_3I are also detected. No products of C-C bond formation are in this group. Interestingly, C_2H_5(g) and C_2H_6(g) are detected during EID of adsorbed CH_3Cl on Ag(111).[30]

Post-irradiation TDS shows a number of new products. While molecular CF_3I decreases in intensity, a CF_2I state grows in at 200 K, then disappears with increasing electron fluence; as it disappears, a CFI state develops at 240 K and again disappears.

This sequence, illustrated in fig. 10, is evidence that electron-induced decomposition proceeds in a stepwise fashion:

$$CF_3I \dashrightarrow CF_2I + F \dashrightarrow CFI + 2F$$

The fluorine liberated in this reaction may contribute to that which is observed in the gas-phase during EID. The increase in desorption temperature corresponding to loss of fluorine indicates that as C-F bonds break, the surface-molecule interaction intensifies. A similar sequential defluorination has been observed in EID of PF_3 on Ru(001).[31]

A number of CF_n products are also observed. CF and CF_4 are detected simultaneously at 250 K, while CF_2 is seen at 350 K. The relatively high temperature for CF_4 desorption indicates a reaction-limited process. Since CF desorption occurs simultaneously, we can imagine a disproportionation reaction of the sort:

$$CF_3(ad) + CF_2(ad) \dashrightarrow CF_4(g) + CF(g)$$

The greater abundance and variety of CF_n species observed in post-EID TDS, relative to normal TDS, may result from a site-blocking effect: EID produces an abundance of fragments at low temperature, which are then stable because the sites needed for thermally-induced decomposition are occupied. Thus, electron impact inhibits subsequent thermal dissociation at the metal surface.

In EID of CF_3Cl on Pt(111), decomposition occurs with a probability close to ours, $\sigma_{EID} = 7 \times 10^{-16}$ cm^2.[10] However, in the CF_3Cl work, no C-C bond formation products are reported, either during electron irradiation or in post-irradiation TDS. The difference may stem from the fact that our work focusses on *multilayer* CF_3I,

while the CF_3Cl/Pt(111) study focusses on *monolayer (chemisorbed)* CF_3Cl. Several other studies have shown that electron-induced coupling occurs readily in hydrocarbons on metal surfaces.[30,32-36] The mechanism is generally thought to be initiated by electron-induced bond dissociation, followed by coupling of the remaining fragments.[30] More specifically for this discussion, perfluorinated molecules are especially susceptible to dissociative electron attachment, resulting in a F^- ion and a radical. This process has, in fact, been suggested as the initiation step in the cross-linking of perfluoropolyethers.[6] It is reasonable to expect that a proximate metal surface might shorten the lifetime, either of the initial ionized molecule (via quenching) or of the resultant free radical, and that electron-induced chemistry would thus be more effective farther from the metal, i.e. more effective in a multilayer than in a monolayer. Comparing the CF_3Cl/Pt(111) work with ours suggests that this is the case, although a more systematic comparison would strengthen that conclusion. Finally, this scenario suggests that electron-induced chemistry in multilayers, not monolayers, is most relevant to that in bulk polymers.

For our system, we postulate the following picture. Incident electrons create fluorocarbon radicals from randomly-oriented, physisorbed molecules; these radicals are then free to desorb, and/or to react further. Some fragments react within the multilayer, whereas others reach the metal surface before reacting/desorbing. Some single-carbon fragments are created. Some of these appear in post-EID TDS as CF_2I and CFI (200, 240 K), while others remain at the metal to higher temperature. Those retained at the metal give rise to the CF and CF_4 desorption states at 250 K,

as well as the CF_2 state peaked at 350 K. Two-carbon fragments also form, leading to C_2F_3I in post-EID TDS. Some C_2 fragments are also retained at the metal surface in the form of C_2F_5. These chemisorbed C_2 fragments are activated in the temperature range 340 to 500 K, yielding a mixture of $C_2F_5(g)$, $C_3F_6(g)$, $C_4F_8(g)$ and $C_2F_6(g)$. It is not clear from our data exactly which reactions occur in the multilayer and which in the monolayer, although it seems probable that the iodine-containing fragments form in the multilayer, given the effectiveness of the Ni(100) surface for C-I bond breaking in the absence of electrons. Hence, the observation of the two-carbon iodide, C_2F_3I, suggests significant C-C bond formation within the multilayer.

5. Summary

The following model for the reactions of CF_3I on Ni(100) develops from our data. The thermally-induced chemistry is simple. Adsorption at 100 K is followed by C-I bond cleavage, either upon adsorption or in the initial stages of heating, resulting in $CF_3(ad)$ and I(ad). $CF_3(ad)$ readily decomposes to C(ad) and F(ad) at low coverages. At coverages approaching saturation of the first layer, CF_3 decomposition is suppressed by a lack of surface sites, and a small CF_3 desorption state appears. F(ad) desorbs as NiF_2 at 885 K, accompanied by a small amount of atomic iodine at exposures approaching saturation, while the main iodine state is observed at 1130 to 1085 K. A CF_3I multilayer state is seen at 150 K, even before the decomposition products are saturated.

The electron-induced chemistry is complex. Irradiation of multilayer CF_3I with

low-energy electrons ($E_i \leq 110$ eV) causes EID with a cross-section, σ_{EID}, of 1.5 x 10^{-16} cm^2. Atomic fluorine is the dominant gaseous product observed during irradiation. Atomic iodine, produced by electron-induced C-I bond scission, is retained at the surface, as evidenced by an increase in the I^+ integrated TDS peak area with electron fluence. Post-irradiation TDS identifies a number of unique electron-induced reaction products. Sequential defluorination of CF_3I yields CF_2I and CFI. CF_2 is another new desorption product, and there is some evidence that adsorbed CF_2 reacts with CF_3, to yield other new gaseous products: CF_4 and CF. A group of fragment ions containing C-C bonds also are detected in a single desorption peak; the parent species may be CF_3CF_2(g), $CF_3CF{=}CF_2$(g), $CF_3C(CF_3){=}CF_2$(g) and a saturated perfluorocarbon, probably C_2F_6(g). These could all form upon rate-limiting activation of CF_3CF_2(ad), a possible product of electron irradiation. Carbon-carbon bond formation is also evident in detection of an iodine-containing molecule, C_2F_3I.

6. Acknowledgments

Thanks are due to R. Rye and D. Saperstein for originally bringing the electron- and photon-induced chemistry of fluoropolymers to our attention, and to C. Jenks and W. Trahanovsky for insightful discussions of halocarbon chemistry. This work is supported by the Ames Laboratory, which is operated for the U.S. Department of Energy by Iowa State University under Contract No. W-7405-Eng-82. In addition, the work is supported by a GAANN Fellowship from the Department of

Education (MBJ), and by Grant No. CHE-9024358 from the National Science Foundation.

7. References

(1) Watson, N. D.; Miller, J. B.; Taylor, L. V.; Lovell, J. B.; Cox, J. W.; Fedors, J. C.; Kopia, L. P.; Holloway, R. M.; Bradley, O. H. *NASA TM-87636*, 1985.

(2) Lee, H. J.; Zubeck, R.; Hollars, D.; Lee, J. K.; Chao, A.; Smallen, M. *J. Vac. Sci. Technol. A* **1993**, *11*, 711.

(3) Oehrlein, G. S.; Zhang, Y.; Vender, D.; Haverlag, M. *J. Vac. Sci. Technol. A* **1994**, *12*, 323.

(4) Oehrlein, G. S.; Zhang, Y.; Vender, D.; Joubert, O. *J. Vac. Sci. Technol. A* **1994**, *12*, 333.

(5) Robertson, R. M.; Golden, D. M.; Rossi, M. J. *J. Vac. Sci. Technol. B* **1988**, *6*, 1632.

(6) Vurens, G. H.; Gudeman, C. S.; Lin, L. J.; Foster, J. S. *Langmuir* **1992**, *8*, 1165.

(7) Lee, T.-H. D. *J. Vac. Sci. Technol. A* **1991**, *9*, 1287.

(8) Rye, R. R. *J. Polym. Sci., Polym. Phys.* **1993**, *31*, 357.

(9) Rye, R. R.; Shinn, N. D. *Langmuir* **1990**, *6*, 142.

(10) Kiss, J.; Alberas, D. J.; White, J. M. *Surf. Sci.* **1992**, *275*, 82.

(11) Walczak, M. M.; Thiel, P. A. *Surf. Sci.* **1989**, *224*, 425.

(12) Wang, W.-D.; Wu, N. J.; Thiel, P. A. *J. Chem. Phys.* **1990**, *92*, 2025.

(13) Becker, G. E.; Hagstrum, H. D. *J. Vac. Sci. Technol.* **1974**, *11*, 284.

(14) Herz, H.; Conrad, H.; Kuppers, J. *J. Phys. E.* **1979**, *12*, 369.

(15) *CRC Atlas of Spectral Data and Physical Constants for Organic Compounds*; 2nd ed.; Grasselli, J. G.; Ritchey, W. M., Ed.; Chemical Rubber Company: Cleveland, 1975.

(16) Dyer, J. S.; Thiel, P. A. *Surf. Sci.* **1990**, *238*, 169.

(17) Jensen, M. B.; Thiel, P. A. unpublished results.

(18) Chiang, C.-M.; Wentzlaff, T. H.; Bent, B. E. *J. Phys. Chem.* **1992**, *96*, 1836.

(19) Butkovskaya, N. I.; Larichev, M. N.; Leipunskii, I. O.; Morozov, I. I.; Tal'roze, V. L. *Dokl. Phys. Chem.* **1978**, *240*, 442.

(20) *CRC Handbook of Chemistry and Physics*; 67th ed.; Weast, R. C., Ed.; Chemical Rubber Company: 1986-87.

(21) Castro, M. E.; Pressley, L. A.; Kiss, J.; Pylant, E. D.; Jo, S. K.; Zhou, X.-L.; White, J. M. *J. Phys. Chem.* **1993**, *97*, 8476.

(22) Liu, Z.-M.; Zhou, X.-L.; Kiss, J.; White, J. M. *Surf. Sci.* **1993**, *286*, 233.

(23) Zhou, X.-L.; White, J. M. *Surf. Sci.* **1988**, *194*, 438.

(24) Zhou, X.-L.; White, J. M. *Chem. Phys. Lett.* **1987**, *142*, 376.

(25) Tjandra, S.; Zaera, F. *Langmuir* **1992**, *8*, 2090.

(26) Tjandra, S.; Zaera, F. *J. Vac. Sci. Technol. A* **1992**, *10*, 404.

(27) Tjandra, S.; Zaera, F. *Surf. Sci.* **1993**, *289*, 255.

(28) Zhou, X.-L.; Solymosi, F.; Blass, P. M.; Cannon, K. C.; White, J. M. *Surf. Sci.* **1989**, *219*, 294.

(29) Zhou, X.-L.; Yoon, C.; White, J. M. *Surf. Sci.* **1988**, *206*, 379.

(30) Zhou, X.-L.; Blass, P. M.; Koel, B. E.; White, J. M. *Surf. Sci.* **1992**, *271*, 427.

(31) Madey, T. E.; Nair, L.; Diebold, U.; Shivaprasad, S. M.; Johnson, A. L.; Poradzisz, A.; Shinn, N. D.; Yarmoff, J. A.; Chakarian, V.; Shuh, D. In *Desorption Induced by Electronic Transitions DIET V*; A. R. Burns, E. B. Stechel and D. R. Jennison, Ed.; Springer-Verlag: Berlin, 1993; Vol. 31; pp 182.

(32) Zhou, X.-L.; Blass, P. M.; Koel, B. E.; White, J. M. *Surf. Sci.* **1992**, *271*, 452.

(33) Zhou, X.-L.; Castro, M. E.; White, J. M. *Surf. Sci.* **1990**, *238*, 215.

(34) Castro, M. E.; Pressley, L. A.; White, J. M. *Surf. Sci.* **1991**, *256*, 227.

(35) Zhou, X.-L.; White, J. M. *J. Phys. Chem.* **1992**, *96*, 7703.

(36) Zhou, X.-L.; White, J. M. *J. Chem. Phys.* **1990**, *92*, 5612.

CHAPTER III. REACTIVITY AND STRUCTURE OF CF_3I ON Ru(001)

A paper submitted to the Journal of Physical Chemistry

M.B. Jensen, U. Myler, C.J. Jenks, E.D. Pylant,[1] J.M. White,[1] and P.A. Thiel

Abstract

A variety of surface-sensitive techniques are used to elucidate the reaction pathways, as well as adsorbate structures, associated with thermal activation of CF_3I following adsorption on Ru(001) at 100 K. XPS shows that the C-I bond of CF_3I dissociates below 200 K to form CF_3(ad) and I(ad); the subsequent reactions of CF_3 are best viewed as being regulated by the availability of surface sites. CF_3(ad) dissociates to CF_2(ad) below 200 K. Further CF_3 dissociation, some of which is activated by H(ad), occurs between 200 K and 400 K until all available sites are filled. Desorption of the remaining CF_3, peaked at 705 K, once again opens surface sites for decomposition. This is followed by recombination of the products to form CF_3(g). No evidence for CF(ad) is ever observed. Hydrogen coadsorption studies explain interesting features associated with fluorine evolution. HREELS and ESDIAD

---

[1]Department of Chemistry and Biochemistry
The University of Texas at Austin
Austin, TX 78712 USA

results indicate that CF_3 adopts a tilted configuration on Ru(001).

1. Introduction

There is a great deal of interest in the reactions of fluorocarbons on metal surfaces. Many studies have been motivated by problems associated with the use of fluorocarbon polymers as high-temperature lubricants in industrial applications.[1] Several investigations have focused on examining short-chain fluorocarbons adsorbed on clean, well-ordered metal and metal oxide surfaces in an attempt to model the polymeric lubricants and to study the mechanisms of degradative reactions known to occur in the presence of metals at elevated temperatures.[2-13] Other studies have investigated the reactions of fluorinated alkyl iodides on metal surfaces.[14-21] Because the C-I bond is easily broken, the iodides are excellent precursors for investigating the basic chemistry of fluorinated alkyl groups. Their chemistry can also be compared with the well-studied reactions of alkyl halides on metals[22-31] to give insight into the effects of fluorination on reactivity.

Focusing specifically on CF_3I, the subject of this study, the C-I bond is cleaved readily on all metals studied thus far, but the C-F bonds are activated differently. CF_3I decomposes to CF_3(ad) and I(ad) on Ag(111) with no evidence of C-F bond cleavage upon heating.[17] On the other hand, Ni(100) totally decomposes CF_3I to C(ad), F(ad), and I(ad).[20] The activity of Pt(111) toward C-F bond cleavage lies between these two extremes, as thermal desorption of both CF_3 and CF_2 is reported.[16]

The catalytic activity of ruthenium, the substrate used in this study, is well-

known[32] and a relatively high C-F bond activity is expected. Indeed, a thermal desorption spectroscopy (TDS) analysis of CF_3I on Ru(001) shows desorption of CF_3, CF_2, and F.[15] The purpose of the present study is twofold: (1) to determine the reaction pathways which lead to formation of CF_3, CF_2, and F, by using X-ray photoelectron spectroscopy (XPS) and coadsorption with H_2; and (2) to obtain structural information about the fluorocarbon adspecies using high-resolution electron energy loss spectroscopy (HREELS) and electron-stimulated desorption ion angular distribution (ESDIAD). The results of a more complete ESDIAD investigation will be published elsewhere.[33]

2. Experimental Description

The experiments are carried out in three separate ultra-high vacuum chambers. High resolution electron energy loss spectroscopy (HREELS) measurements are carried out in the first chamber, described in detail elsewhere.[34,35] HREELS spectra are taken at the specular angle with a primary beam energy of 1.6 eV and a resolution of 11 meV full width at half maximum (FWHM). The intensity of the elastic peak is adjusted to 6×10^4 counts per second (cps) before scanning.

X-ray photoelectron spectroscopy (XPS) experiments are carried out in a second UHV chamber described previously.[36] Mg Kα radiation at 1253.6 eV is generated by a Vacuum Generators X-ray source, while photoelectron measurements are made with a double pass cylindrical mirror analyzer (PHI 15-255GAR) with an analyzer pass energy of 50 eV. Experiments are performed by flashing the crystal,

then immediately cooling back to 100 K before beginning the scan. XPS scan windows are 15 eV wide and data collection time is about 15 min. Core level binding energies are referenced to the Ru($3d_{5/2}$) photoelectron peak centered at 280.0 eV. (Peak width at half maximum, $\Delta E_{1/2}$, is 1.9 eV.) Binding energy uncertainties are approximately ±0.15 eV. I($3d_{5/2}$) spectra are plotted with scatter points representing the raw data and a solid line through the points calculated with a weighted, least-squares smoothing routine. F(1s) spectra show scatter points for the raw data, along with dotted lines indicating each individual state, and a solid line representing the sum of the individual states. Curve fitting is accomplished by first smoothing the data using a 13-point Savitsky-Golay routine, then fitting this smoothed data by assuming a 100% Gaussian peak shape and a full width at half maximum (FWHM) of 1.9 eV for each individual state. All data smoothing and curve fitting is performed using Axum software (TriMetrix, Inc.).

Thermal desorption spectroscopy and electron-stimulated desorption ion angular distribution (ESDIAD) experiments are carried out in a third chamber, described previously.[3] The details of the ESDIAD experiments will be given elsewhere.[33] TDS experiments are performed using a UTI 100C quadrupole mass spectrometer (QMS) interfaced to a HP Vectra QS/20 microcomputer such that multiplexing of up to eight masses is possible. The heating rate is 5.3 K/s (100-200 K), 2.3 K/s (200-400 K), and 4.2 K/s (400-1500 K) for all TDS experiments. It should be noted that, in comparison to previous work,[15] the RF generator of the QMS is retuned to maximize sensitivity in the high mass range (>40 amu). This

leads to different fragmentation patterns for CF_x desorbing species. The new relative intensities are CF^+(0.45), CF_2^+(1.00), and CF_3^+(0.42) for CF_3 parent, and CF^+(0.86) and CF_2^+(1.00) for CF_2 parent. Also, we have found that the high fluorine signal commonly observed in residual gas analysis (RGA) of vacuum chambers after prolonged use of fluorinated compounds is greatly reduced by an increase in the QMS emission current (from 2.0 mA to 3.0 mA), thereby depleting the ionizer surface of adsorbed atomic fluorine via electron-stimulated desorption (ESD).

The temperature of the crystal is monitored with a W5%Re-W26%Re thermocouple spotwelded to the back of the crystal for the HREELS, TDS, and ESDIAD experiments. Temperature in the XPS measurements is calibrated with an optical pyrometer. Because of the large uncertainty in this approach, it appears that temperatures in the latter case are as much as 100 K lower than those in the other three experiments. Each chamber allows for resistive heating and thermal contact with a liquid nitrogen reservoir. CF_3I exposures are cross-calibrated by determining the saturation point of I(ad).[15] This is accomplished by measuring either the I^+ TDS peak area or the Ru(273)/I(511) peak ratio in Auger electron spectroscopy (AES) versus CF_3I dosing time. Exposures are reported in simple percentages of the exposure required to saturate the I^+ desorption signal, e.g. a '60% saturation exposure.'

Initial cleaning of the Ru(001) single crystal has been detailed previously.[3] Major contaminants include O, C, and Si. These impurities can be removed by a combination of Ar^+ sputtering, O_2 exposure, and annealing at 1600-1700 K. Sample

cleanliness is monitored by AES and/or XPS. CF_3I is purchased from PCR, Inc. which specifies 99.0% purity. Several freeze-pump-thaw cycles are carried out with liquid nitrogen for further purification. CF_3I is introduced into all three vacuum chambers through a directional gas doser. H_2 used in coadsorption experiments is purchased from Matheson (min. 99.99% purity) and introduced through a standard leak valve with no further purification. H_2 exposures are reported in Langmuirs (1 L = 10^{-6} Torr-s).

3. Results

3.1 TDS

The thermal desorption spectrum of a saturation exposure of CF_3I on Ru(001) at 100 K is shown in fig. 1. A complete TDS study has been published previously, and the results of that investigation are summarized in table 1.[15] As can be seen from table 1, two states of molecular CF_3I are observed. These are assigned to a chemisorbed layer bound directly to the surface and a physisorbed multilayer, with desorption peak temperatures at 145 K and 136 K, respectively. A substantial amount of C-F and C-I bond breaking occurs as evidenced by desorption states of CF_2, CF_3, CF_4, atomic iodine, and two states of atomic F. The area of the I^+ peak (m/z = 127) grows monotonically with increasing exposure until a saturation level is reached, above which only the multilayer CF_3I state grows. Sub-saturation exposures sequentially populate the two atomic fluorine states at 270-390 K and 1226 K, followed by CF_2 at 1165 K, CF_3 at 705 K, and finally a small amount of CF_4 at 605 K.

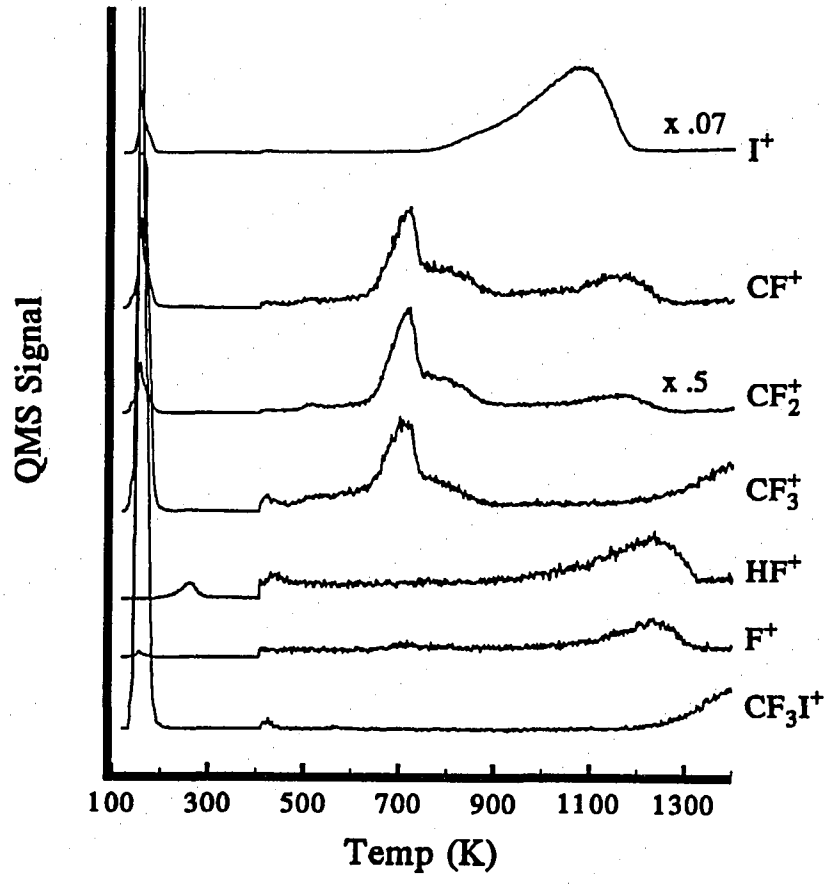

Figure 1. Thermal desorption spectrum for CF_3I on Ru(001) following a saturation exposure at 100 K.

Table 1. Summary of TDS results [Ref. 15]

Desorbing Species	Peak temperature (K)	Onset exposure (% saturation)	Exposure at maximum yield (% saturation)
I	1130-1060	0	100
F	270-390	18	100
	1226	24	67
CF_3I	145	18	100
	136	100	n/a
CF_2	1165	44	71
CF_3	705	67	100
CF_4	605	100	100

Peak temperatures of the CF_2 and CF_3 states remain constant with increasing exposure, showing no characteristics of second- (or higher-) order desorption.[15] We call special attention to the shape of the CF_3 peak, where a sharp peak at 705 K is superimposed on a much broader feature extending to 900 K.

As can be seen from fig. 1, depending on the level of background hydrogen, QMS detection of HF^+ (m/z = 20) can be more sensitive than F^+ (m/z = 19) to the previously-mentioned atomic fluorine states at 270-390 K and 1226 K. The HF^+ signal can arise from one of three possible sources: desorption-limited HF, reaction-limited HF, or desorption of F(ad) followed by hydrogenation in the vacuum chamber. The relatively high desorption temperatures allow us to rule out desorption-limited HF; HF is known to desorb from metal surfaces below 130 K.[37-39] Reaction-limited HF can be ruled out for the 1226 K state since hydrogen desorption from clean Ru(001) is complete by 500 K.[40] We can, therefore, attribute the 1226 K state to desorption of atomic fluorine followed by hydrogenation in the vacuum chamber.

The lower-temperature state attributed to atomic fluorine is more complex, and actually consists of two well-resolved features. Two features were also suggested in the previous TDS data for F^+ (although not well-resolved).[15] Figure 2 shows the HF^+ signal in the 100-500 K range as a function of increasing CF_3I exposure. In fig. 2, the first feature appears initially at 390 K and shifts down while growing larger, then disappears; the second appears at 250 K and shifts slightly upward while growing larger. These shifts in peak position indicate a deviation from simple first-order

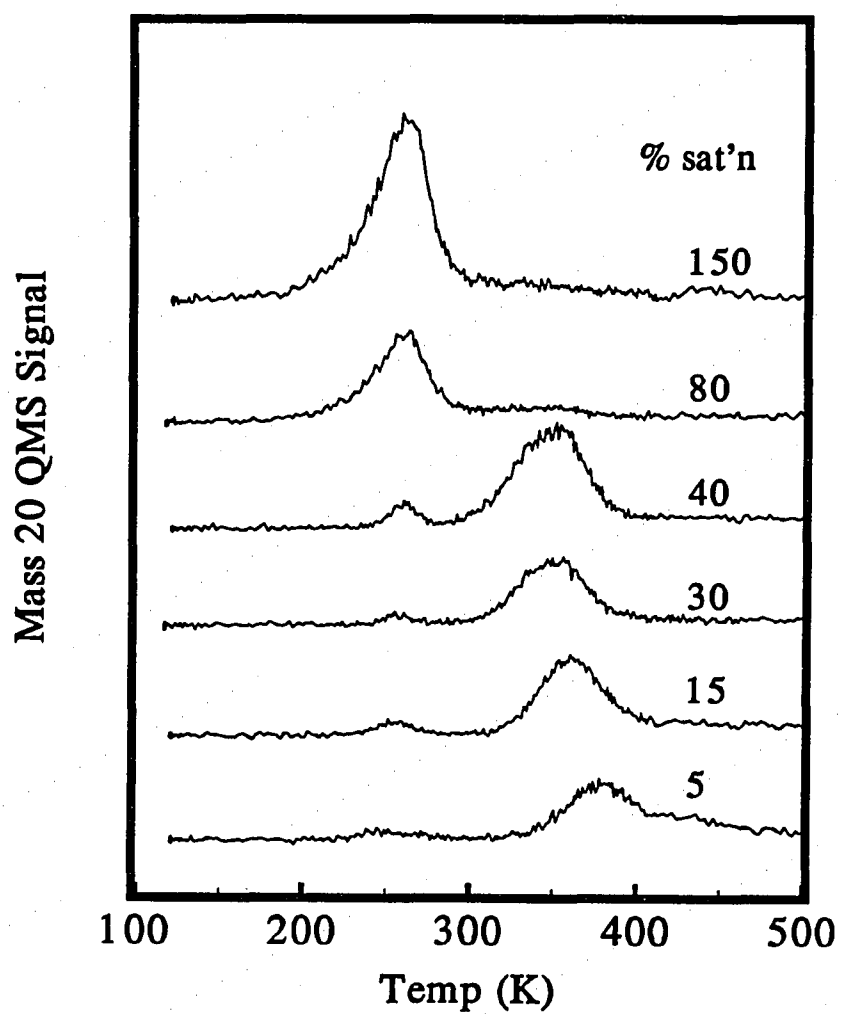

Figure 2. HF^+ (m/z = 20) TDS spectra in the 100-500 K range, as a function of increasing CF_3I exposure.

desorption kinetics. The two components of this single 'state' are clearly coupled: rapid growth of the second feature is accompanied by extinction of the first, between exposures which are 40% and 80% of saturation. Interestingly, further examination of the data presented in ref. [15] shows the feature at 260 K to become dominant at the same exposure where CF_3 desorption at 705 K begins to appear. As pointed out in ref. [15], and evident also in our experimental data, a small amount of fluorocarbon desorbs with this state at 260 K for high CF_3I coverages.

3.2 Coadsorption with H_2

The interesting behavior of HF^+ in TDS is clarified by coadsorption of CF_3I and H_2. Adsorption of H_2 on Ru(001) at 100 K results in dissociation to form H(ad).[41] Figure 3 shows the results of a 60% saturation exposure of CF_3I on clean Ru(001), followed by a 2.0 L H_2 exposure. Figure 3A shows the HF^+ (m/z = 20) signal which monitors desorbing HF and F, while fig. 3B shows the CF_2^+ (m/z = 50) signal, monitoring CF_3I and CF_2 desorption. The dotted lines represent a TDS experiment with no H coadsorption, while the solid lines represent a CF_3I exposure followed directly by 2.0 L H_2 at 100 K. Clearly, H_2 does little to affect either the amount or the temperature of molecular CF_3I desorption. Above 200 K, however, the chemistry changes greatly. Figure 3A shows that when H is coadsorbed with CF_3I, both features of the low-temperature HF state grow substantially, with the lowest shifting from 265 K to 275 K, and the highest shifting from 340 K to 325 K. The CF_2 and F intensities, meanwhile, drop to barely detectable levels. The results shown

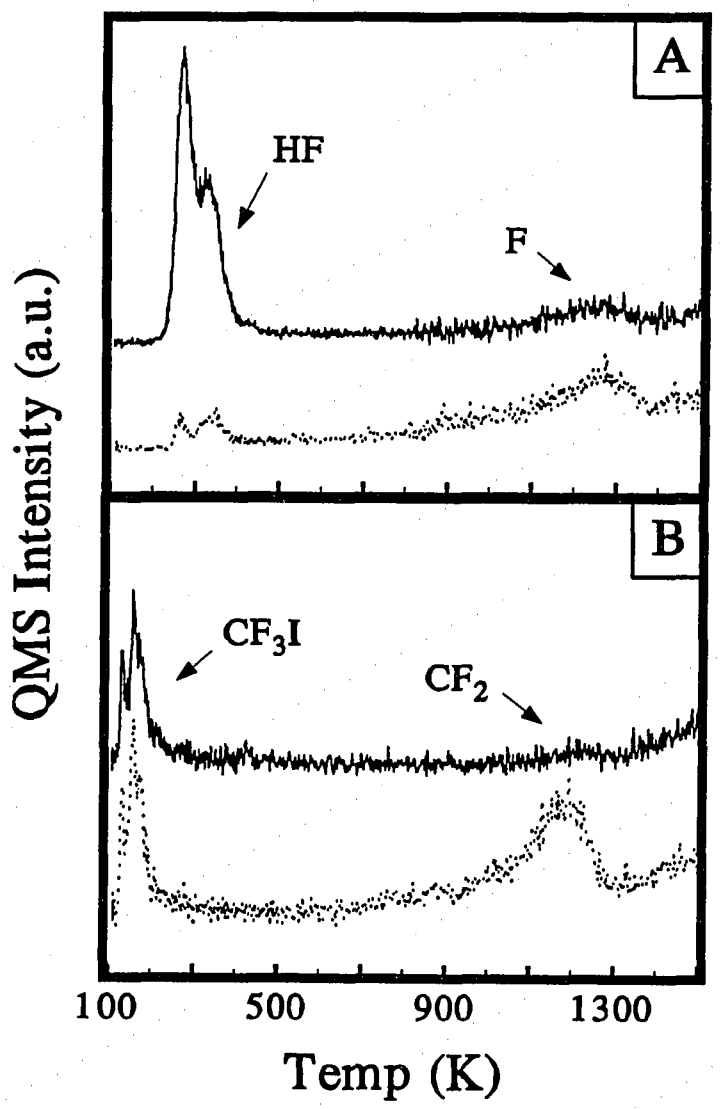

Figure 3. Results of H_2 coadsorption experiments for a 60% saturation coverage of CF_3I showing TDS signal for (A) HF^+, and (B) CF_2^+. Dotted lines show the TDS signal following adsorption of CF_3I alone. Solid lines show the signal when a 2.0 L H_2 exposure at 100 K immediately follows CF_3I adsorption.

in fig. 3 lead us to conclude that coadsorbed H has little effect on the initial decomposition of adsorbed CF_3I. Molecular desorption is not altered, and, in data not shown, the atomic iodine state is unchanged. The decomposition of the resulting CF_x species, however, is very different: coadsorbed H(ad) appears to activate C-F bonds, resulting in more HF desorption. Similar results were reported previously for D_2/CF_3I coadsorption studies on Pt(111).[16]

Figure 4 shows results from coadsorption experiments which are different in two ways. First, the sample is annealed between exposures. In each curve, the crystal is flashed to the given temperature after CF_3I exposure, then cooled to 150 K, and finally exposed to 2.0 L H_2. Second, the CF_3I exposure is slightly higher, about 80% of saturation. Under these conditions, fig. 4A shows the HF^+ TDS signal while fig. 4B shows CF_2^+. The dotted lines in fig. 4B represent the control experiments using the same experimental conditions, except no H_2 exposure. No similar dotted lines are included in fig. 4A since the controls show negligible signal above background.

Comparison of the solid and dotted lines in the 600 K and 700 K cases of fig. 4B shows that while coadsorbed H_2 has no effect on the CF_3 desorption state, the intensity of the CF_2 state at 1165 K is slightly lower. This loss of CF_2 is accompanied by the emergence of the HF state between 250-400 K in fig. 4A. Presumably, the F which is lost from the CF_2 state appears in the emerging HF state. As the flash temperature increases to 950 K, the HF peak becomes very large and the corresponding CF_2 signal disappears completely. Above 950 K, the CF_2 desorption state remains absent, and the HF peak area eventually declines.

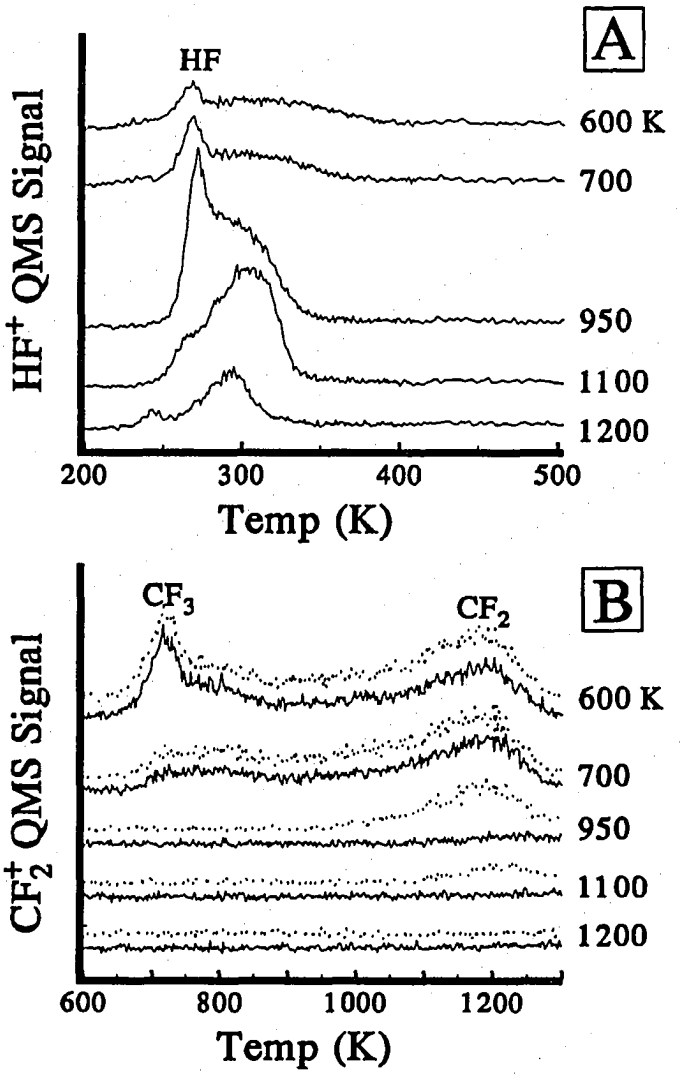

Figure 4. Results of H_2 coadsorption experiments for an 80% saturation coverage of CF_3I showing (A) HF^+, and (B) CF_2^+ TDS signals. Experiments are performed by first exposing Ru(001) to CF_3I at 100 K, flashing to the desired temperature, then exposing to 2.0 L H_2 at 150 K, and running TDS. The dotted lines indicate the identical experimental procedure without the H_2 exposure.

As indicated in sec. 3.1, two HF features are evident in the 100-500 K range (fig. 2). Both are also evident in the coadsorption experiments (figs. 3 and 4). The first of these is broad, with peaks from 290 K (fig. 4A) to 380 K (fig. 2). This wide range of values is consistent with second-order kinetics, since the peak at 380 K in fig. 2 corresponds to H_2 exposure from the background (low coverage), while the 290 K peak in fig. 4A corresponds to a deliberate H_2 exposure (higher coverage). The TDS data in fig. 1 show that flashing a CF_3I multilayer to 1200 K depletes the surface of all adsorbed species except atomic fluorine (and possibly some residual carbon). When H_2 is dosed after flashing to 1200 K, TDS shows a strong HF peak at 290 K (fig. 4A). We can, therefore, attribute the broad HF feature showing second-order characteristics to combinative desorption of F(ad) and H(ad).

The other HF feature between 100 K and 500 K is sharper and appears first at 250 K in fig. 2, then shifts slightly upward with increasing CF_3I exposure. In the coadsorption studies, this peak is as high as 275 K. Although the mechanism is not unequivocal, we hypothesize that this feature is due to H(ad)-induced C-F bond activation, resulting in formation of HF(g). As previously indicated, this peak is accompanied by a small amount of CF_x desorption at high CF_3I coverages.

3.3 XPS

X-ray photoelectron spectroscopy (XPS) yields further insight into the composition of the adlayer. A summary of the species detected by XPS and their respective binding energies, as well as a comparison to related work, is given in table

2.

The relative contribution of molecular and dissociative adsorption at 100 K is revealed by the F(1s) spectra, shown as a function of exposure at 100 K, in fig. 5. Some degree of molecular adsorption is to be expected since TDS shows desorption of chemisorbed CF_3I beginning after an exposure of 18% saturation. Indeed, XPS shows two states: CF_3 at 685.4 eV and CF_3I at 687.1 eV. A comparison of the peak areas of the two states shows a 2:1 CF_3 to CF_3I ratio following an exposure of 25% saturation at 100 K, while at 50% saturation this ratio increases to 2.4:1. Increasing the CF_3I exposure to 150% saturation shows no change in the size of the CF_3 peak, but approximately a six-fold increase in the CF_3I peak, indicating that adsorption is mostly molecular above 50% saturation.

F(1s) XPS spectra are shown in fig. 6 as a function of annealing temperature, starting from the multilayer represented at the top of fig. 5. By 200 K the CF_3I state at 687.1 eV disappears, and a CF_2 state can be identified at 686.8 eV along with the CF_3 state at 685.4 eV. The area of the CF_3 portion is approximately 20% larger at 200 K than at 100 K, indicating that some molecular CF_3I dissociates as the temperature is raised. Between 200 and 500 K, the CF_3 to CF_2 ratio decreases from 4.2:1 to 2.2:1, mainly due to loss of CF_3. A new state appears at 681.4 eV and is attributed to atomic fluorine. Interestingly, there is no change in the size of the CF_2 peak upon heating from 200 K to 500 K, as would occur if CF_3(ad) were forming CF_2(ad) and F(ad). This indicates either that CF_3 decomposes completely to C and F, while CF_2 is stable, or that both CF_3 and CF_2 defluorinate simultaneously, with

Table 2. Summary of XPS binding energies (eV)

Species		CF_3I/Ru(001)[a]	CF_3I/Pt(111)[b]	CF_3I/Ag(111)[c]	F/TiN(100)[d]
F(1s)	CF_3I	687.1	687.3	687.9	-
	CF_3	685.4	685.8	686.0	-
	CF_2	686.8	686.4	-	-
	F	681.4, 682.5	-	-	683.8
I($3d_{5/2}$)	CF_3I	~619.8	620.4	620.5	-
	I	619.3	619.5	618.7	-

[a] This work [b] Ref [16] [c] Ref [17] [d] Ref [42]

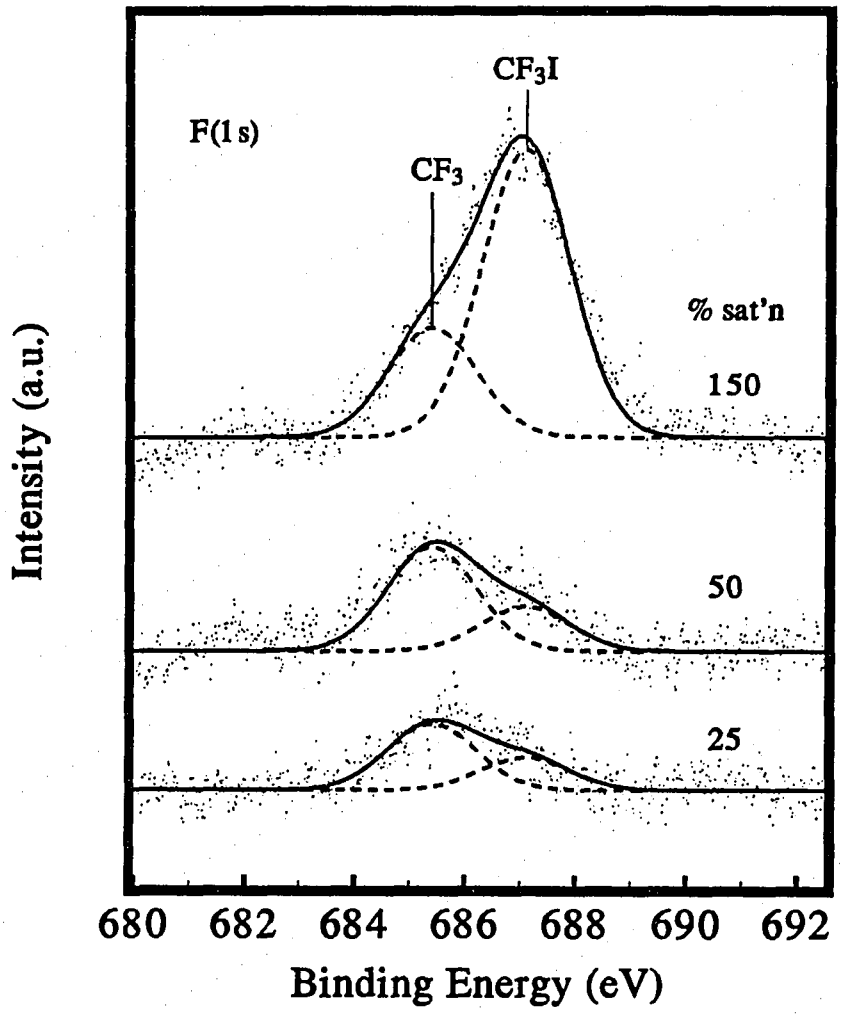

Figure 5. F(1s) XPS spectra as a function of initial CF_3I exposure at 100 K.

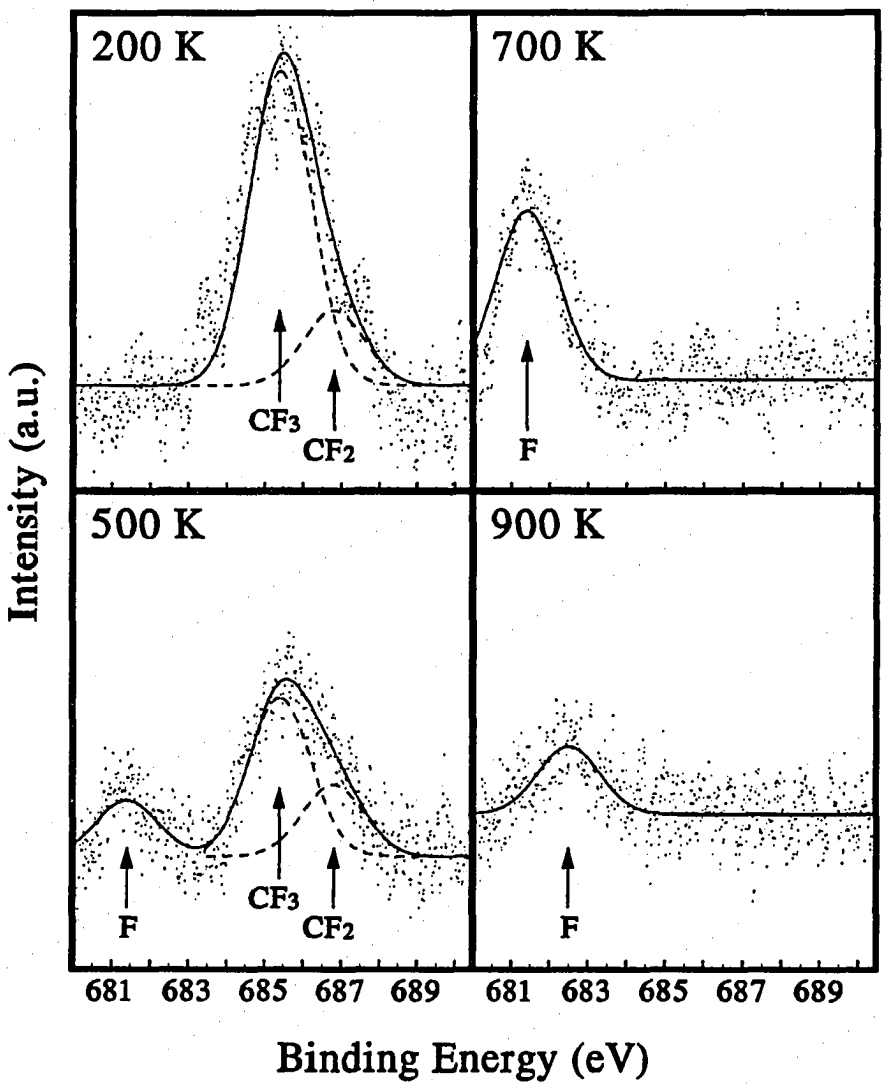

Figure 6. F(1s) XPS spectra at different annealing temperatures. The initial CF_3I exposure is 150% saturation. The y-scales in all four spectra are the same.

the rate of formation of CF_2 cancelled exactly by its rate of loss, i.e. with no net change in CF_2 concentration. The latter scenario seems unlikely, as there is no apparent reason why these two rates should simply cancel.

After flashing to 700 K, no fluorocarbons appear in XPS. TDS shows a desorption state of CF_3 peaked at 705 K, and tailing off to almost 900 K. Although the origin of this TDS state is discussed in sec. 4.1., we note here that the low-temperature component alone is associated with CF_3(ad). Hence, heating to 700 K leaves the crystal in the CF_3 desorption region long enough to remove all, or nearly all, the CF_3(ad), thus accounting for its disappearance in XPS.

Upon flashing to 900 K, F(1s) XPS shows one peak at 682.5 eV; by 1100 K no F(1s) signal is visible (not shown). We attribute the peak at 682.5 eV, as well as the peak at 681.4 eV, to atomic fluorine. The shift from 681.4 eV to 682.5 eV is interesting. We speculate that different binding sites, possibly defect sites, are populated at the higher temperature.

It should be noted that XPS is relatively insensitive to low concentrations of fluorine. TDS shows desorption of CF_2 at 1165 K and F at 1226 K, yet XPS shows no F(1s) signal above 1100 K. Unfortunately, overlap of the C(1s) peak with that of Ru($3d_{3/2}$) precludes quantitation of C(1s) spectra.

The interpretation of the F(1s) spectra is supported by I($3d_{5/2}$) XPS as a function of increasing temperature (fig. 7). Beginning again with a thin multilayer (150% of saturation), fig. 7 shows a peak at 619.8 eV. This value varies significantly from the reported values of 620.4 eV and 620.5 eV for multilayer CF_3I on Pt(111)[16]

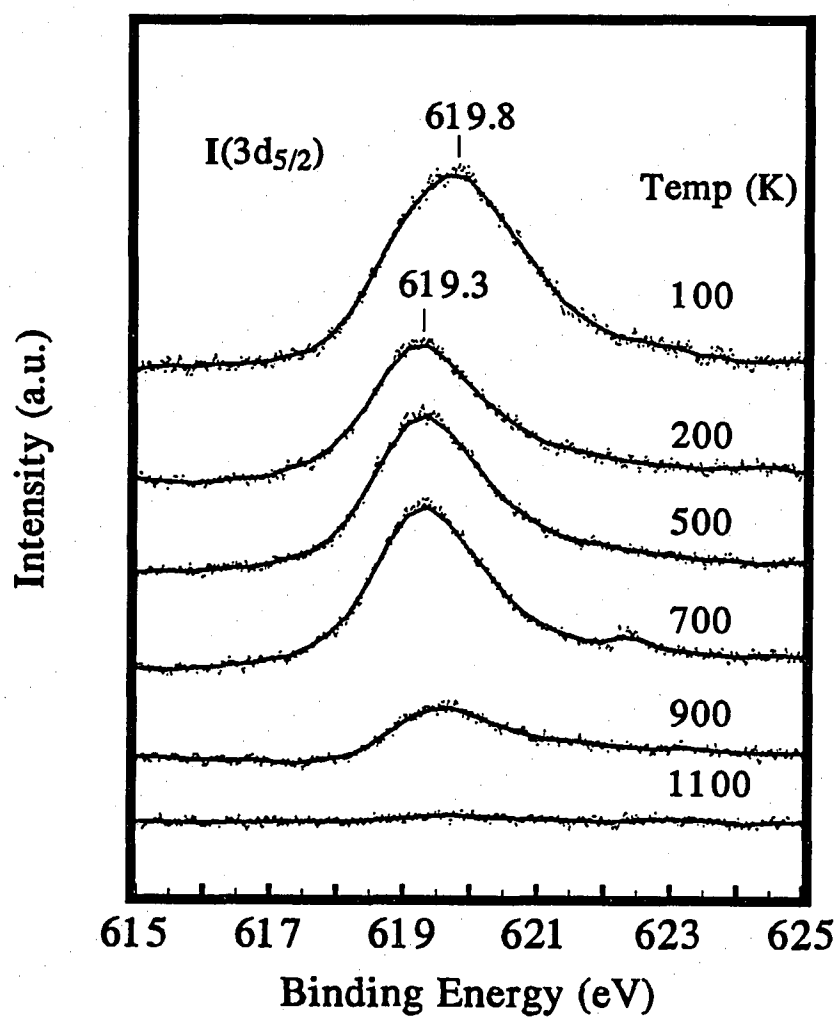

Figure 7. $I(3d_{5/2})$ XPS spectra as a function of annealing temperature for a 150% saturation exposure of CF_3I at 100 K.

and Ag(111),[17] respectively. This difference may have two sources. The first is a substrate contribution due to the thin initial multilayer (< 2 layers) used in our experiments. Second, the width of this peak indicates a contribution from I(ad), consistent with the F(1s) data showing some C-I bond scission at 100 K. Therefore, the overlap of the multilayer and atomic iodine peaks may also cause some difference. Upon heating to 200 K, all molecular CF_3I, both physisorbed and chemisorbed, desorbs and the peak at 619.8 eV decreases in intensity and shifts to 619.3 eV. We assign this to I(ad) since its position and intensity remain constant until the beginning of atomic iodine desorption (fig. 1). No iodine is detected by XPS after flashing to 1100 K.

Figure 8 shows the I($3d_{5/2}$) signal as a function of CF_3I exposure. At 25% saturation a peak at 619.4 eV is observed. The slight shift from the I(ad) value of 619.3 eV seen in fig. 7 indicates a contribution from both I(ad) and molecular CF_3I. No change in peak position is observed in moving from 25% saturation to 50%. Population of the multilayer, however, causes the peak to shift to 619.8 eV.

3.3 HREELS

We now turn to HREELS for information regarding the structure of adsorbed CF_3I and the resulting CF_x species. Figure 9 shows the HREELS spectra of a multilayer (300% of saturation exposure) of CF_3I on Ru(001) at 80 K as a function of annealing temperature. Peaks are visible at 745, 1092, and 1189 cm^{-1}. Based on previous assignments, compiled in table 3, we assign these peaks to the C-F

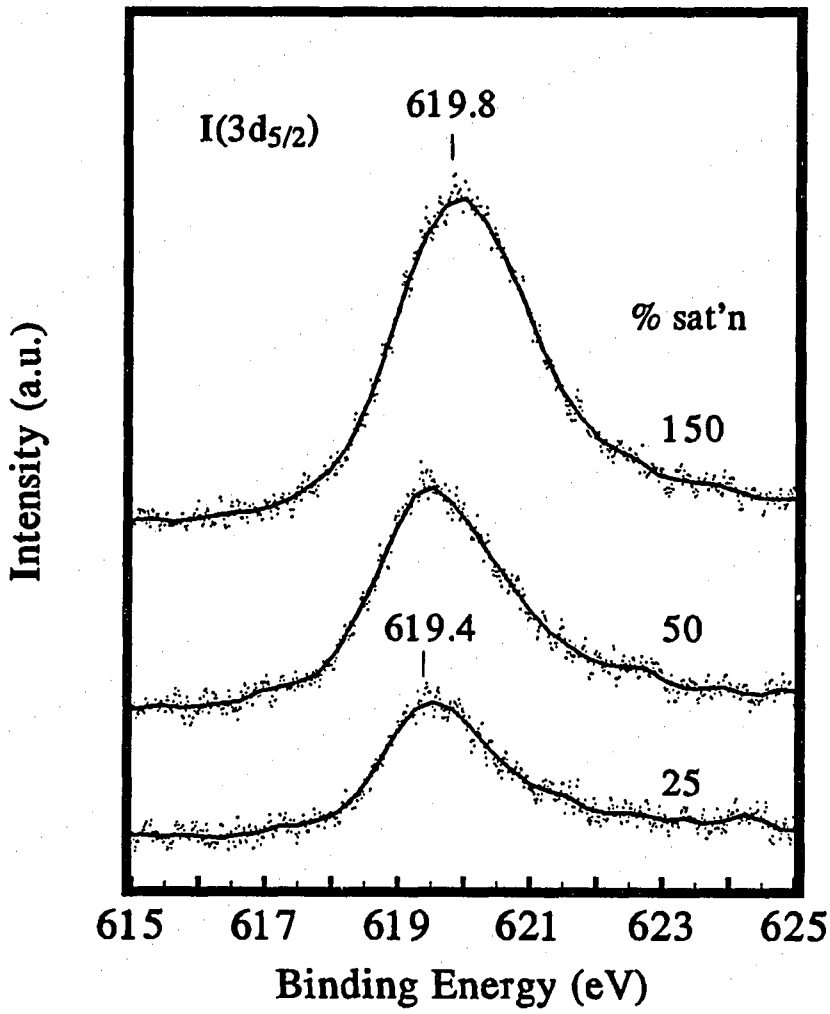

Figure 8. $I(3d_{5/2})$ XPS spectra as a function of initial CF_3I exposure at 100 K.

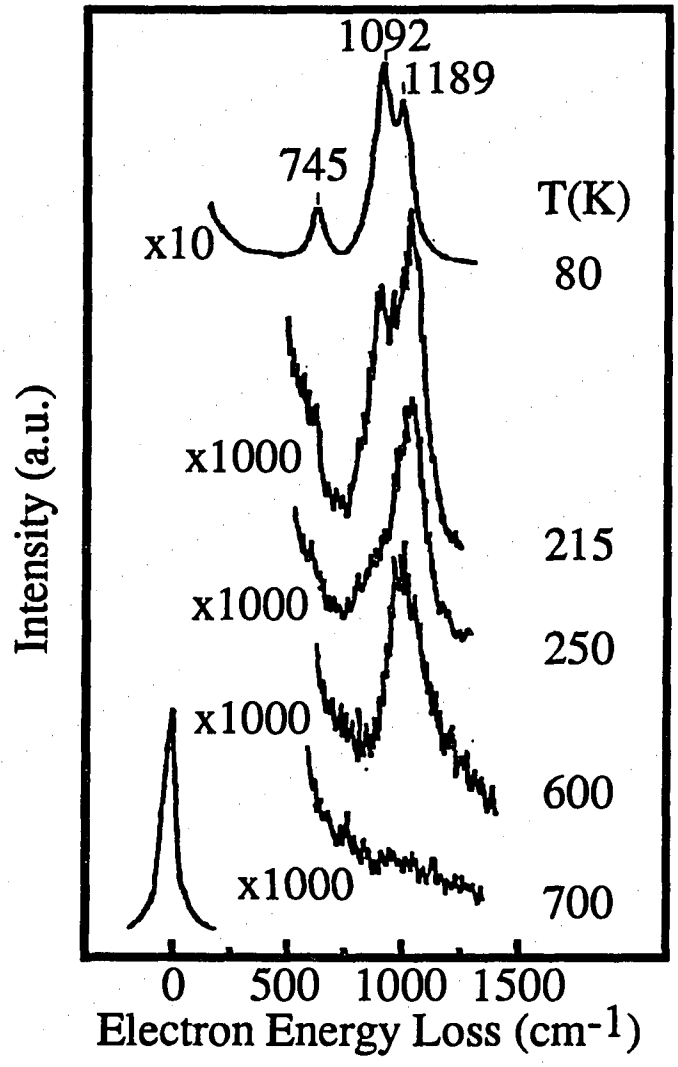

Figure 9. HREELS spectra shown as a function of annealing temperature for a multilayer (300% saturation exposure) of CF_3I deposited at 80 K.

Table 3. Vibrational assignments (cm^{-1}) for CF_3I, CF_3, and CF_2.

species	ref.	C-F sym. stretch	CF_x asym. stretch	CF_3 sym. deformation	CF_3 asym. deformation	C-I stretch	C-I bend
CF_3I(g)	[43]	1076	1185	743	539	284	260
CF_3I/Pt(111)	[16]	1050-1060	1180-1200	735	535	245	n.o.
CF_3I/Pt(111)	[19]	1060	1190	745	540	n.o.	n.o.
CF_3I/Ru(001)	this work	1092	1189	745	n.o.	n.o.	n.o.
CF_3	[44]	1087	1251	703	512	-	-
CF_3/Pt(111)	[16]	1060	-	735	-	-	-
CF_3/Pt(111)	[19]	1060	-	745	-	-	-
CF_3/Ru(001)	this work	1082	1210-1240	-	-	-	-
CF_3/Cu(100)	[45]	1205	-	-	-	-	-
CF_2	[44]	1222	1102	-	-	-	-
CF_2/Pt(111)	[16]	1200	-	-	-	-	-
CF_2/Pt(111)	[19]	1210	-	-	-	-	-

n.o. = not observed

symmetric deformation, the C-F symmetric stretch, and the C-F asymmetric stretch, respectively. We detect neither the asymmetric C-F deformation (at 539 cm^{-1} in the gas-phase), nor the C-I stretch (at 284 cm^{-1}).

Upon annealing to 215 K, the peak at 745 cm^{-1} disappears. As at 80 K, two peaks are evident in the C-F stretching range, but their positions shift to 1082 cm^{-1} and 1240 cm^{-1}. Raising the temperature to 250 K results in loss of the feature at 1082 cm^{-1}, leaving only the peak at 1240 cm^{-1}. By 600 K we still observe only one peak, but its position shifts to 1202 cm^{-1}. This peak disappears at 700 K, above which no loss features are evident.

3.4 ESDIAD

The results of a complete ESDIAD investigation will be published elsewhere.[33] For present purposes, fig. 10 shows the ESDIAD image produced from a multilayer exposure of CF_3I (400% of saturation) heated to 500 K. The image itself is taken after re-cooling to 170 K. We believe that this image represents emission from the (001) terraces. Only a single normal beam is visible with no evidence for azimuthal ordering. Figure 11 shows that a different ESDIAD image is obtained when the incident electron beam is focussed near the edge of the crystal. Other conditions are the same as in fig. 10. This image shows hexagonal emission, all trace of which disappears at 700 K.

Identification of the ESD products is possible by focusing the resulting ion beam into the QMS with the ionizer current turned off. Not surprisingly, F^+ is the

Figure 10. ESDIAD image of a multilayer coverage of CF_3I after heating to 500 K.

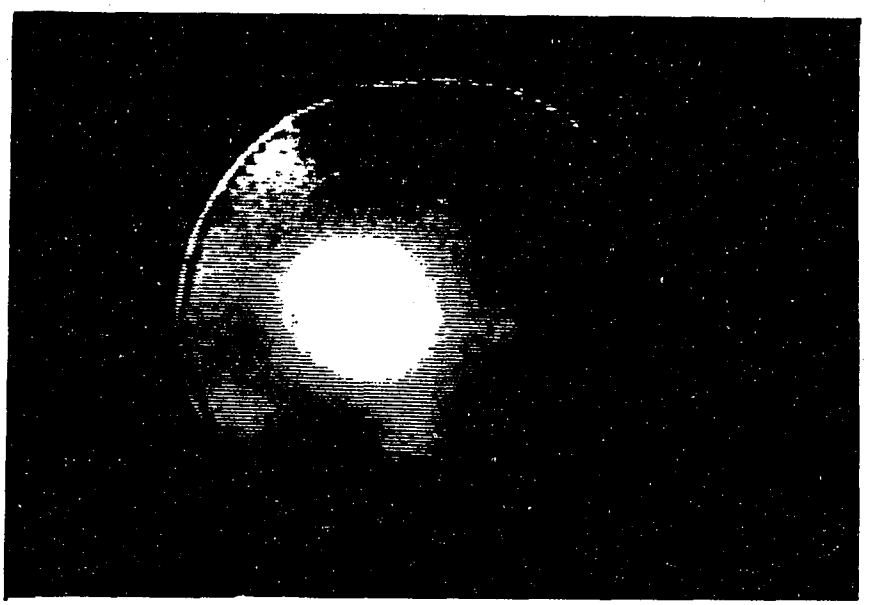

Figure 11. ESDIAD image, with the electron beam focused on the edge of the crystal, from a multilayer coverage of CF_3I after heating to 500 K.

major ESD product identified. We can, therefore, attribute the ESDIAD images in figs. 10 and 11 to ESD of fluorine from either F(ad) or CF_x(ad).

4. Discussion

4.1 Reactions of CF_3I

The original observation of CF_3 and CF_2 desorption in this system, and the coverage-dependent emergence of these species (table 1), led to speculation about whether desorption of these fragments was controlled by dissociation-site-blocking or dissociation-recombination.[15] Our data show that, while both processes occur, the predominant features of this system are controlled by dissociation-site-blocking of the adsorbed CF_3 fragment.

This CF_3 fragment forms already upon adsorption at 100 K, as shown clearly by the XPS data of fig. 5. Adsorption is both molecular and dissociative, resulting in a mixture of CF_3I(ad), CF_3(ad), and I(ad). The relative areas of the peaks corresponding to CF_3(ad) and CF_3I(ad) show that dissociative adsorption dominates at exposures below 50% saturation. In moving from 50% saturation to 150%, the size of the F(1s) peak associated with CF_3(ad) does not change, thereby indicating that adsorption is almost entirely molecular above 50% saturation. Similar results, showing the predominance of dissociative adsorption at low coverage and molecular adsorption at high coverage, are reported for CF_3I adsorption at 105 K on Ag(111).[17]

A saturation exposure of CF_3I results in two molecular desorption states, a multilayer at 136 K and a chemisorbed layer at 145 K. By 200 K the remaining C-I

bonds break, as shown by the 200 K XPS spectrum of fig. 6. Also, by 200 K, a small amount of CF_2(ad) is evident. This CF_2(ad) is most likely formed by thermal decomposition of CF_3(ad). Consistent with the site-blocking model, we believe that this decomposition reaction is regulated by the availability of surface sites and we speculate that at low coverages, conversion from CF_3 to CF_2 is most complete.

Further defluorination of CF_3, and possibly CF_2 , occurs between 200 and 400 K, as indicated by XPS. This is due, at least in part, to C-F bond activation induced by the adsorption of background H_2 on the surface. This C-F bond breaking is responsible for the two peaks in the HF^+ desorption signal shown in fig. 2. The first peak, at 250 K, is attributed to HF(g) formed during the activation step. The second, appearing between 300 K and 400 K, is due to combinative desorption of some F(ad) with H(ad). (XPS shows in fig. 6 that a significant amount of F(ad) is also retained beyond this point.)

The emergence of the low-temperature HF^+ feature with increasing coverage, coupled with disappearance of the higher-temperature feature, can also be explained by site-blocking (fig. 2). At low coverage, C-F bond activation results in F(ad), which is subsequently depleted by combinative desorption to form HF(g). As coverage increases, dissociation becomes more difficult and occurs only in the presence of H(ad). This is consistent with the observation that the 250 K HF feature becomes dominant at the same exposure where CF_3 desorption begins to appear at 705 K, since we attribute the latter to first-order desorption of stable CF_3. Hence, CF_3 emergence at 705 K and HF growth at 250 K are both signatures of the same

phenomenon: stabilization of CF_3 against dissociation by site-blocking at high coverage. Some fluorocarbon fragments may also be ejected directly into the gas phase upon CF_3 dissociation at high coverages, explaining the small CF^+ and CF_3^+ desorption peaks concomitant with the low-temperature HF^+ peak (fig. 1). Ejection into the gas-phase may again be favored by the absence of sites to accommodate CF_x fragments.

Thus, at high coverages (> 70% of saturation exposure), a substantial amount of CF_3(ad) remains on the surface at 500 K. Some of this CF_3(ad) desorbs with maximum rate at 705 K. As this desorption step begins, surface sites are again available for decomposition. This decomposition is not only supported by an increase in the amount of F(ad) detected at 700 K by XPS (fig. 6), but also by the H_2 coadsorption data presented in fig. 4. After flashing the crystal to 600 K, very little space is available for H_2 adsorption, as evidenced by very little C-F bond activation following H_2 exposure. At 700 K, CF_3 desorption occurs. If surface sites were now available for H(a), H_2 exposure would result in increased C-F bond activation and a large HF desorption peak at 250 K. As fig. 4 shows, this is not the case until the flash temperature reaches 950 K. Instead, as CF_3 desorbs at 700 K, vacated surface sites are quickly filled by further decomposition of CF_3, thereby inhibiting H_2 adsorption after flashing to 700 K.

The thermal desorption data show a very small CF_4 state at 605 K.[15] This is certainly due to a recombination reaction, probably either CF_3(ad) or CF_2(ad) with F(ad), or CF_2(ad) with CF_2(ad). If the reaction involves CF_2(ad), this would explain

the apparent stability of CF_2 up to 500 K, and its abrupt disappearance by 700 K (fig. 6). Alternatively, the disappearance of the CF_2 signal in XPS upon heating to 700 K (fig. 6) may be due to simple dissociation when sites become available at high temperatures.

The CF_3 desorption state from 650 K to 900 K (fig. 1) is actually comprised of two features. The first is the peak at 705 K which we have already attributed to desorption-limited CF_3 evolution. The second, a higher-temperature foot extending to 900 K, is more difficult to interpret. XPS shows no evidence of C-F bonds following a flash to 700 K, but substantial loss of atomic fluorine between 700 K and 900 K. Because the only related desorption feature in this range is the high-temperature CF_3 foot, we are led to conclude that this CF_3 feature is the result of recombination of F(ad) with CF_x (ad) (x=1,2), or with atomic carbon, C(ad). This conclusion is similar to the recombination of PF_x(ad) (x=0,1,2) fragments, observed both on Ni(111)[46] and Ru(001).[47] The fact that XPS detects no C-F species in this range indicates that concentrations of any CF_x species are very small, or that reaction of F(ad) with C(ad) to form CF_3 is followed by instantaneous desorption, leaving no CF_x to detect with XPS upon re-cooling.

The only remaining desorption features are atomic iodine, a CF_2 state at 1165 K and an atomic fluorine state at 1225 K. Figure 1 shows iodine desorption between 700 K and 1200 K. The asymmetry on the low-temperature side of the peak is similar to that which has been observed in at least one other system.[48] In our case, it appears coupled to the state we have attributed to recombinative CF_3 desorption,

an observation for which we can offer no explanation at this time. The CF_2 state may arise from recombination, e.g. of C(ad) and F(ad), although the apparent order of the desorption kinetics does not support this. Alternatively, the CF_2 state may arise from desorption of stable CF_2, although no C-F bonding is detected above 700 K by XPS (fig. 6) or HREELS (fig. 9). The XPS data might be explained if the concentration of CF_2 remaining at high temperatures is simply below the detection limit of XPS, as is certainly the case for the atomic F which remains to 1225 K. A similar explanation could apply to the HREELS data, although a poor detection limit in HREELS could also be due to a tilted geometry (sec. 4.2), rather than a low concentration. (The TDS data cannot be calibrated to yield effective surface concentrations for various states, unfortunately, but it is not unreasonable to expect that the detection limit of TDS can be much smaller than that of XPS or HREELS.) In any case, it is probable that both of these high-temperature desorbates, CF_2 and F, arise from species formed as a result of C-F bond activation at 250 K, since both states are depleted by H_2 coadsorption (figs. 3 and 4). The apparent inertness of these species toward recombination at lower temperature may be a result of preferential adsorption in a specific type of site, such as a defect site. It is reasonable that such more-stable (less-reactive) sites would be occupied first. This would then explain why the two high-temperature desorption states are populated at low to medium coverages, preceding the appearance of recombinative CF_3(ad) (table 1).

The model which develops, then, is one in which dissociation of CF_3I to CF_3 and CF_2 occurs between 100 and 200 K. The CF_3 can dissociate further between 200

and 500 K. As coverage increases, dissociation of CF_3 is inhibited due to site-blocking. At high coverages, around 600 K, recombination, probably of CF_3(ad) or CF_2(ad) with F(ad), yields CF_4(g). At 700 K, desorption of CF_3 occurs, freeing sites for further dissociation, which is then followed by recombination and desorption of more CF_3. The origin of high-temperature desorbates, CF_2 and F, is difficult to assess, mainly because our HREELS and XPS data do not detect any associated adsorbed species.

4.2 Structures of CF_x

XPS shows that the fraction of CF_3I which adsorbs molecularly, directly to the Ru substrate, does so through the iodine atom. Figure 5 shows that the F(1s) binding energy for CF_3I(ad) does not change in moving from submonolayer to multilayer coverages. On the other hand, the corresponding I($3d_{5/2}$) peak, shown in fig. 8, does shift in moving to multilayer coverages. This suggests that the iodine, not the fluorine, interacts with the metal surface. This argument was also used previously to describe the bonding of CF_3I to Pt(111).[16]

The HREELS results of fig. 9 yield information regarding the structure of the fluorocarbon species which form following decomposition of CF_3I. As the results in table 3 indicate, the spectrum for a CF_3I multilayer at 80 K closely resembles that of CF_3I(g). Upon heating, however, several changes occur. The symmetric deformation at 745 cm^{-1} disappears, leaving only C-F stretches at 1082 cm^{-1} and 1240 cm^{-1}. The positions of these peaks match closely the symmetric and asymmetric C-F stretches

measured at 1087 cm^{-1} and 1251 cm^{-1}, respectively, for the CF_3 radical isolated in an inert argon matrix.[44] If we adopt these assignments, and assume that CF_3 is bonded to the metal through the carbon atom, we see that the structure of CF_3(ad) on Ru(001) is much different than on Pt(111) and Cu(100), which show only the symmetric stretch, thereby indicating CF_3(ad) adsorption with C_{3v} symmetry.[16,19,45] The observation of both the symmetric and the asymmetric modes indicates that CF_3(ad) is adsorbed in a tilted configuration on Ru(001).

Upon annealing to 250 K, the symmetric component disappears and only a single peak at 1240 cm^{-1} remains. This may indicate a stronger tilt of the CF_3 group, making the C-F symmetric stretch invisible due to the surface dipole selection rule. (If this interpretation is correct, however, the constancy of the frequency at 1240 cm^{-1} is somewhat puzzling; major changes in orientation should be accompanied by changes in frequency as well.) The single peak persists, although decreasing in frequency, to 700 K where TDS shows CF_3 desorption (fig. 1).

The published C-F stretching assignments listed in table 3 show that frequency assignments based solely on comparison with the matrix isolation study may be inaccurate. For instance, while a frequency of 1087 cm^{-1} is reported for the symmetric C-F stretch of CF_3 in an argon matrix, values reported for CF_3(ad) range from 1060 cm^{-1} to 1205 cm^{-1}.[16,19,45] To provide further help we turn to the ESDIAD results. A CF_3(ad) species exhibiting C_{3v} symmetry and bonded through the carbon atom should produce a hexagonal ESDIAD image generated by two adsorption domains each rotated 60^0 from the other. Our ESDIAD results, however, show

hexagonal emission from CF_3(ad) only on the crystal edge (fig. 11). There is only a single central beam visible from CF_3(ad) on the crystal terraces (fig. 10), generated by ESD of F^+ from a C-F bond oriented perpendicularly to the surface plane. This is consistent with our assignment of the HREELS peak at 1240 cm^{-1} to the asymmetric stretch of tilted CF_3(ad).

Support for this approach to combining ESDIAD and vibrational spectroscopy is provided by a previous study of PF_3 adsorption on Ni(111). There, only one IR band, the P-F symmetric stretch, is visible following PF_3 adsorption indicating a C_{3v} adsorption geometry;[49] consistent with this assignment, ESDIAD shows a six-beam hexagon.[50]

Combining the HREELS and ESDIAD interpretations, then, the picture for CF_3(ad) is one of a tilted molecule which retains some degree of pyramidal symmetry, with one of the C-F bonds perpendicular to the surface. Then the other two C-F bonds would necessarily be in close proximity to the surface, perhaps stabilized by a favorable F-Ru interaction. C-F bond interaction with Ru through the F atom has been documented in the organometallic literature.[51]

Interestingly, our ESDIAD results and their interpretations are very similar to those for NF_3 on Ru(001).[52] In that study, as in ours, only normal emission of ESD products is detected on the crystal terraces, whereas hexagonal images are seen near edges of the crystal face. In both studies, the effect of crystal edges--with their high defect-densities--remains unexplained at this time.

Figure 9 shows that the frequency of the C-F asymmetric stretch decreases

from 1240 cm^{-1} at 215 K to 1202 cm^{-1} at 600 K. Although not shown in fig. 9, this shift actually occurs above temperatures of 400 K. We attribute this shift to a decrease in dipole-dipole interactions between neighboring CF_3 groups following the activation of C-F bonds which occurs below 400 K. A similar effect has been well-characterized for PF_3 adsorption on metal surfaces.[49,53] On Ni(111), for instance, an upward shift of 58 cm^{-1} in the P-F symmetric stretch with increasing coverage is attributed to increased dipole-dipole coupling between PF_3 groups.[49]

While our discussion of the HREELS results has centered around the structure of CF_3(ad), the data must also be reconciled with the evidence for CF_2. The evidence is of two types, and applies over two different temperature regimes: first, TDS data showing CF_2(g) above 700 K; and second, XPS data showing CF_2(ad) below 700 K. It is not necessary that the same explanation apply in both regimes. Possible explanations for the first case have already been offered in sec. 4.1. In the second case, XPS shows a significant amount of CF_2(ad) below 700 K; yet no new HREELS features arise from such a species. One possible explanation is that the bands of CF_2(ad) overlap with those of CF_3(ad). This is possible, given the relative broadness of the peak and the previously-reported stretching frequencies of CF_2 listed in table 3. However, examination of the peak intensities as a function of temperature (not shown) offers no support for this interpretation. Another possibility is that the CF_2(ad) adsorption geometry makes its vibrational activity invisible to HREELS detection. If CF_2 is strongly tilted, i.e. with its molecular axis parallel, or nearly so, to the surface plane {as proposed for CF_3(ad)}, then both the symmetric and

asymmetric C-F stretches would be inactive.

5. Conclusions

CF_3I adsorbs both molecularly and dissociatively at 100 K on Ru(001), with dissociative adsorption dominating at low exposures and molecular adsorption dominating at high exposures. Upon heating, the multilayer desorbs at 136 K and part of the undecomposed, chemisorbed layer desorbs at 145 K. By 200 K all C-I bonds have broken, and some of the remaining CF_3(ad) groups have decomposed to CF_2(ad). Further defluorination of the CF_3 species occurs between 200 and 400 K. Coadsorption with H_2 indicates this process is at least partially induced by H(ad) from adsorption of background H_2 and, at high coverage, may be accompanied by direct ejection of CF_x fragments into the gas phase.

At high coverages, surface fragments combine at 605 K to desorb as CF_4(g), after which desorption of CF_3 begins, peaking at 705 K. This desorption step opens up surface sites for further decomposition of CF_3(ad) and, possibly, CF_2(ad). Some of the decomposition products recombine up to 900 K and desorb as CF_3(g). Above 900 K desorption of atomic iodine is observed, as well as desorption of CF_2 at 1165 K and F at 1225 K. The high-temperature CF_2 state may be due to recombination of atomic species, or desorption of a minority state, such as CF_2 at steps.

HREELS data suggest that CF_3(ad) adopts a strongly-tilted orientation, thereby causing the C-F symmetric stretch to be inactive. This is supported by ESDIAD, which shows only normal emission of F^+ for CF_3 adsorbed on terrace sites.

The ESDIAD results are interpreted to mean that one C-F bond is perpendicular to the surface, while the other two are in close proximity to the metal.

6. Acknowledgments

Thanks are due to J. W. Anderegg for helpful discussions regarding X-ray photoelectron spectroscopy. This work is supported by Ames Laboratory, which is operated for the U.S. Department of Energy by Iowa State University under Contract No. W-7405-Eng-82. In addition, the work is supported by a GAANN Fellowship from the Department of Education (MBJ), and by Grant No. CHE-9024358 from the National Science Foundation (PAT).

7. References

(1) Del Pesco, T. W. In *Synthetic Lubricants and High-Performance Functional Fluids*; R. L. Shubkin, Ed.; Marcel Dekker: New York, 1993; pp 145.

(2) Walczak, M. M.; Leavitt, P. K.; Thiel, P. A. *J. Am. Chem. Soc.* **1987**, *109*, 5621.

(3) Walczak, M. M.; Thiel, P. A. *Surf. Sci.* **1989**, *224*, 425.

(4) Walczak, M. M.; Leavitt, P. K.; Thiel, P. A. *Trib. Trans.* **1990**, *33*, 557.

(5) Leavitt, P. K.; Thiel, P. A. *J. Vac. Sci. Technol. A* **1990**, *8*, 2269.

(6) Jenks, C. J.; Jacobson, J. A.; Thiel, P. A. *J. Vac. Sci. Technol. A* **1994**, *12*, 2101.

(7) Takeuchi, K.; Salmeron, M.; Somorjai, G. A. *Surf. Sci.* **1992**, *279*, 328.

(8) John, P. J.; Liang, J. *J. Vac. Sci. Technol. A* **1994**, *12*, 199.

(9) Maurice, V.; Takeuchi, K.; Salmeron, M.; Somorjai, G. A. *Surf. Sci.* **1991**, *250*, 99.

(10) Golden, W. G.; Hunziker, H.; de Vries, M. S. *J. Phys. Chem.* **1994**, *98*, 1739.

(11) Napier, M. E.; Stair, P. C. *Surf. Sci.* **1993**, *298*, 201.

(12) Napier, M. E.; Stair, P. C. *J. Vac. Sci. Technol. A* **1991**, *9*, 649.

(13) DeKoven, B. M.; Meyers, G. F. *J. Vac. Sci. Technol. A* **1991**, *9*, 2570.

(14) Jones, R. G.; Singh, N. K. *Vacuum* **1988**, *38*, 213.

(15) Dyer, J. S.; Thiel, P. A. *Surf. Sci.* **1990**, *238*, 169.

(16) Liu, Z.-M.; Zhou, X.-L.; Kiss, J.; White, J. M. *Surf. Sci.* **1993**, *286*, 233.

(17) Castro, M. E.; Pressley, L. A.; Kiss, J.; Pylant, E. D.; Jo, S. K.; Zhou, X.-L.; White, J. M. *J. Phys. Chem.* **1993**, *97*, 8476.

(18) Sun, Z.-J.; Schwaner, A. L.; White, J. M. *Chem. Phys. Lett.* **1994**, *219*, 118.

(19) Armentrout, D. D.; Grassian, V. H. *Langmuir* **1994**, *10*, 2071.

(20) Jensen, M. B.; Thiel, P. A. *J. Am. Chem. Soc.* in press.

(21) Forbes, J. G.; Gellman, A. J. *J. Am. Chem. Soc.* **1993**, *115*, 6277.

(22) Lin, J.-L.; Bent, B. E. *J. Vac. Sci. Technol. A* **1992**, *10*, 2202.

(23) Zhou, X.-L.; White, J. M. *Surf. Sci.* **1988**, *194*, 438.

(24) Zhou, X.-L.; Yoon, C.; White, J. M. *Surf. Sci.* **1988**, *206*, 379.

(25) Chiang, C.-M.; Wentzlaff, T. H.; Jenks, C. J.; Bent, B. E. *J. Vac. Sci. Technol. A* **1992**, *10*, 2185.

(26) Henderson, M. A.; Mitchell, G. E.; White, J. M. *Surf. Sci.* **1987**, *184*, L325.

(27) Zhou, Y.; Henderson, M. A.; Feng, W. M.; White, J. M. *Surf. Sci.* **1989**, *224*, 386.

(28) Zhou, X.-L.; Solymosi, F.; Blass, P. M.; Cannon, K. C.; White, J. M. *Surf. Sci.* **1989**, *219*, 294.

(29) Chen, J. G.; Beebe, T. P.; Crowell, J. E.; Yates, J. T., Jr. *J. Am. Chem. Soc.* **1987**, *109*, 1726.

(30) Zaera, F.; Hoffmann, H. *J. Phys. Chem.* **1991**, *95*, 6297.

(31) Zaera, F. *Acc. Chem. Res.* **1992**, *25*, 260.

(32) Anderson, R. B. *The Fischer-Tropsch Synthesis*; Academic Press: Orlando, 1984.

(33) Jensen, M. B.; Dyer, J. S.; Leung, W.-Y.; Thiel, P. A. in preparation.

(34) Columbia, M. R.; Thiel, P. A. *Rev. Sci. Instrum.* **1987**, *58*, 309.

(35) Leavitt, P. K.; Davis, J. L.; Dyer, J. S.; Thiel, P. A. *Surf. Sci.* **1989**, *218*, 346.

(36) Koel, B. E.; Peebles, D. E.; White, J. M. *Surf. Sci.* **1983**, *125*, 709.

(37) Wagner, F. T.; Moylan, T. E. *Surf. Sci.* **1987**, *182*, 125.

(38) Stuve, E. M.; Kizhakevariam, N. *J. Vac. Sci. Technol. A* **1993**, *11*, 2217.

(39) Kay, B. D.; Lykke, K. R.; Creighton, J. R.; Ward, S. J. *J. Chem. Phys.* **1989**, *91*, 5120.

(40) Schwarz, J. A. *Surf. Sci.* **1979**, *87*, 525.

(41) Feulner, P.; Menzel, D. *Surf. Sci.* **1985**, *154*, 465.

(42) Guinn, K. V.; Donnelly, V. M.; Gross, M. E.; Baiocchi, F. A.; Petrov, I.; Greene, J. E. *Surf. Sci.* **1993**, *295*, 219.

(43) McGee, P. R.; Cleveland, F. F.; Meister, A. G.; Decker, C. E.; Miller, S. I. *J. Chem. Phys.* **1953**, *21*, 242.

(44) Milligan, D. E.; Jacox, M. E. *J. Chem. Phys.* **1968**, *48*, 2265.

(45) Girolami, G. S.; Jeffries, P. M.; Dubois, L. H. *J. Am. Chem. Soc.* **1993**, *115*, 1015.

(46) Alvey, M. D.; Yates, J. T., Jr. *J. Am. Chem. Soc.* **1988**, *110*, 1782.

(47) Madey, T. E.; Nair, L.; Diebold, U.; Shivaprasad, S. M.; Johnson, A. L.; Poradzisz, A.; Shinn, N. D.; Yarmoff, J. A.; Chakarian, V.; Shuh, D. In *Desorption Induced by Electronic Transitions DIET V*; A. R. Burns, E. B. Stechel and D. R. Jennison, Ed.; Springer-Verlag: Berlin, 1993; Vol. 31; pp 182.

(48) Jo, S. K.; White, J. M. *Surf. Sci.* **1992**, *261*, 111.

(49) Guo, X.; Yates, J. T., Jr.; Agrawai, V. K.; Trenary, M. *J. Chem. Phys.* **1991**, *94*, 6256.

(50) Alvey, M. D.; Yates, J. T., Jr.; Uram, K. J. *J. Chem. Phys.* **1987**, *87*, 7221.

(51) Catala, R. M.; Cruz-Garritz, D.; Hills, A.; Hughes, D. L.; Richards, R. L.; Sosa, P.; Torrens, H. *J. Chem. Soc., Chem. Comm.* **1987**, 261.

(52) Walczak, M. M.; Johnson, A. L.; Thiel, P. A.; Madey, T. E. *J. Vac. Sci. Technol. A* **1988**, *6*, 675.

(53) Agrawal, V. K.; Trenary, M. *J. Chem. Phys.* **1991**, *95*, 6962.

CHAPTER IV. AN ESDIAD AND LEED INVESTIGATION OF CF_3I ON Ru(001)

A paper to be submitted to Langmuir

M.B. Jensen, J.S. Dyer, W.-Y. Leung, and P.A. Thiel

Abstract

We have investigated the thermal chemistry of CF_3I adsorbed at 100 K on Ru(001) using low-energy electron diffraction (LEED) and electron-stimulated desorption ion angular distribution (ESDIAD). LEED indicates formation of $(\sqrt{3}x\sqrt{3})R30^{o}$ islands of atomic iodine for coverages up to 67% saturation. At higher CF_3I coverages, iodine adsorbs in an apparent p(2x2) configuration until thermal desorption of CF_3(ad) allows the iodine atoms to occupy the more favorable $(\sqrt{3}x\sqrt{3})$ sites. ESDIAD images at temperatures and coverages where CF_3(ad) is the dominant molecular fragment are generated by ESD of F^+ at a desorption angle normal to the surface plane, indicating a tilted configuration of CF_3(ad) in which one C-F bond is oriented perpendicular to the surface. In addition to normal emission, ESDIAD also identifies a number of hexagonal patterns. A small hexagon is attributed to F(ad) on step edges, providing more sensitive detection of F(ad) than XPS. A large hexagon at low coverages may arise from isolated CF_3(ad) species possessing C_{3v} symmetry.

And finally, an intermediate hexagon is attributed to perturbation of the CF_3(ad) orientation by electron-induced decomposition (EID) fragments which result from electron irradiation of physisorbed CF_3I.

1. Introduction

The widespread use of fluorocarbons in a number of technologically relevant applications has generated a great deal of interest in the chemistry of these molecules adsorbed on surfaces. In particular, the chemistry of trifluoroiodomethane (CF_3I) adsorbed on metal surfaces has been the subject of several recent investigations.[1-8] The relatively weak C-I bond (2.3 eV) is easily cleaved by thermal means, making CF_3I an ideal precursor for examining the reactivity of adsorbed trifluoromethyl groups--just as a number of studies have successfully utilized iodoalkanes as precursors to adsorbed alkyl groups.[9]

While a number of surface-sensitive experimental techniques have been applied to the study of adsorbed CF_3I, electron-stimulated desorption ion angular distribution (ESDIAD) is one technique yet to be utilized. Fluorine-containing compounds are ideal for investigation with ESD techniques due to the high ESD cross-section of F^+.[10] This sensitivity, coupled with the strong possibility of azimuthal ordering of CF_3(ad) on a close-packed surface, makes CF_3I on Ru(001) an ideal system for ESDIAD analysis. ESDIAD has been previously applied to the study of other highly symmetric fluorine-containing compounds adsorbed on metals, most notably NF_3 on Ru(001),[11] SF_6 on W(011) and W(111),[12] and PF_3 on Ni(111)[13,14] and

Ru(001).[15-20] We also note a recent related study of the ESDIAD behavior of CCl_4 on Ru(001).[21] To our knowledge, however, ESDIAD has yet to be applied to the investigation of an adsorbed fluorocarbon.

In this paper we present the results of an ESDIAD investigation of CF_3I on Ru(001). The results of a previously reported thermal desorption spectroscopy (TDS) study of CF_3I on Ru(001) are summarized in table 1.[2] Desorption states attributable to CF_3I, CF_4, CF_3, CF_2, F, and I are identified. The integrated area of the atomic iodine desorption peak grows linearly with CF_3I exposure before leveling off at a point we define as 100% saturation. CF_3I exposures in the current study are reported relative to the exposure required to reach saturation.

In another paper, we present X-ray photoelectron spectroscopy (XPS), high resolution electron energy loss spectroscopy (HREELS), and H_2 coadsorption results, as well as preliminary ESDIAD results, of an investigation of CF_3I on Ru(001).[7] Adsorption of CF_3I at 100 K is found to be both molecular and dissociative, resulting in CF_3I(ad), CF_3(ad), and I(ad). By 200 K all C-I bonds have broken and some CF_3(ad) has decomposed to CF_2(ad). Between 200 and 400 K, in a process at least partially induced by H(ad) from background H_2 adsorption, further defluorination of CF_3 is observed. At high coverages, surface fragments combine at 605 K to desorb as CF_4, followed by desorption of CF_3, peaking at 705 K. As CF_3 desorption proceeds, surface sites are opened up for further decomposition of CF_3, and possibly CF_2. Some of these fragments recombine below 900 K and desorb as CF_3.

HREELS, in conjunction with ESDIAD, gives evidence for a "tilted" CF_3(ad)

Table 1. Summary of TDS results [Ref. 2]

Desorbing Species	Peak temperature (K)	Onset exposure (% saturation)	Exposure at maximum yield (% saturation)
I	1130-1060	0	100
F	270-390	18	100
	1226	24	67
CF_3I	145	18	100
	136	100	n/a
CF_2	1165	44	71
CF_3	705	67	100
CF_4	605	100	100

species with one C-F bond oriented normal to the surface plane. In the current paper we present the full results of the ESDIAD study, along with low-energy electron diffraction (LEED) results, covering the entire range of coverage and temperature following CF_3I adsorption at 100 K.

2. Experimental Description

The experiments are performed in a stainless steel, ultra-high vacuum (UHV) chamber with a base pressure of 8×10^{-11} Torr. The chamber, described previously,[22] is equipped for TDS, ESDIAD/LEED, Auger electron spectroscopy (AES), ion bombardment, and gas introduction.

ESDIAD and LEED experiments are carried out using a conventional ESDIAD/LEED optics assembly consisting of three wire mesh grids (two hemispherical and one planar) followed by a dual microchannel plate (MCP) assembly and a phosphor-coated viewing screen. The electron source is a PHI Model 04-015 grazing incidence electron gun. Images are monitored with a CCD video camera and recorded with a videocassette recorder. All ESDIAD and LEED images shown in this report are photographed from videotape, although both live and recorded images may be digitized using a HP Vectra QS/20 computer equipped with a video processor board (Matrox MVP-AT).

A primary electron beam energy set at 250 eV, with a sample current of 25 nA, is used in the ESDIAD experiments. By focusing the electron beam on a phosphor-coated aluminum flag, we estimate the beam diameter at approximately

1 mm, resulting in a current density of 2 x 10^{11} s^{-1} mm^{-2}. An image compression bias of +30 V is applied to the crystal, resulting in a net primary beam energy of +280 eV. The mesh grid closest to the crystal is held at ground potential, the second at +34 V, and the third at -300 V. All ESDIAD images are taken at T ≤ 170 K after heating the crystal to the desired temperature. The electron beam may be rastered with the electron gun deflection plates to avoid excessive electron beam damage.

TDS experiments are performed using a UTI 100C quadrupole mass spectrometer (QMS) interfaced to a HP Vectra QS/20 computer for simultaneous monitoring of 1-8 masses. A series of three electrostatic lenses shield the crystal from stray electron current from the QMS ionizer during the TDS experiment.

The Ru(001) single crystal is spotwelded to two Ta rods in thermal contact with a liquid nitrogen-coolable cold finger. This configuration allows for resistive heating to 1700 K, followed by rapid cooling to 100 K. Temperature is monitored with a W5%Re-W26%Re thermocouple spotwelded to the back of the crystal. Initial cleaning of the Ru(001) crystal is outlined elsewhere.[22] Major contaminants are carbon, oxygen, and silicon. These are removed by a combination of argon ion bombardment, oxygen exposure, and high-temperature annealing, with surface cleanliness monitored by AES. Between experiments the surface is cleaned by a 5-10 L O_2 exposure at 700 K followed by annealing at 1700 K.

CF_3I is purchased from PCR, Inc. which specifies 99.0% purity. Further purification is accomplished by several freeze-pump-thaw cycles with liquid nitrogen. XeF_2 is purchased from Aldrich. Transfer of the XeF_2 to a sealed glass vial with

vacuum fittings is carried out in a helium-filled glove box. Both CF_3I and XeF_2 are introduced into the vacuum chamber through a directional gas doser connected to a gas-handling manifold.

3. Results

3.1 LEED

Figure 1 outlines the LEED behavior, as a function of temperature, for a CF_3I multilayer coverage. The (1x1) pattern obtained from the clean surface is shown in fig. 1a. Figure 1b shows non-integral order spots which appear following annealing of the multilayer coverage to 400 K. It is unclear whether these new spots are due to a p(2x2) or a p(2x1) surface structure since both generate the same LEED pattern. Increasing the temperature to 700 K results in splitting of these non-integral spots, as shown in fig. 1c. This splitting results in the $(\sqrt{3}x\sqrt{3})R30^{o}$ pattern seen in fig. 1d following annealing to 800 K. At 1100 K only the (1x1) spots are visible.

As for the coverage dependence of the LEED patterns, only the (1x1) is seen for exposures below 20% saturation. From 20% to 67% saturation, the $(\sqrt{3}x\sqrt{3})R30^{o}$ pattern emerges between 300 and 600 K. In this coverage regime the temperature of first appearance of the $\sqrt{3}$ pattern decreases with increasing coverage, but its disappearance is always complete by 1100 K. The LEED pattern showing 1/2 order beams first appears at approximately 67% saturation, where the CF_3 desorption state also emerges (table 1), and is visible at all exposures thereafter. These 1/2 order

Figure 1. LEED patterns resulting from a saturation exposure of CF_3I on Ru(001). (a) (1x1) from the clean surface; (b) p(2x2) resulting from heating to 400 K; (c) splitting of the p(2x2) following heating to 700 K; (d) $(\sqrt{3}x\sqrt{3})R30^{o}$ visible upon heating to 800 K.

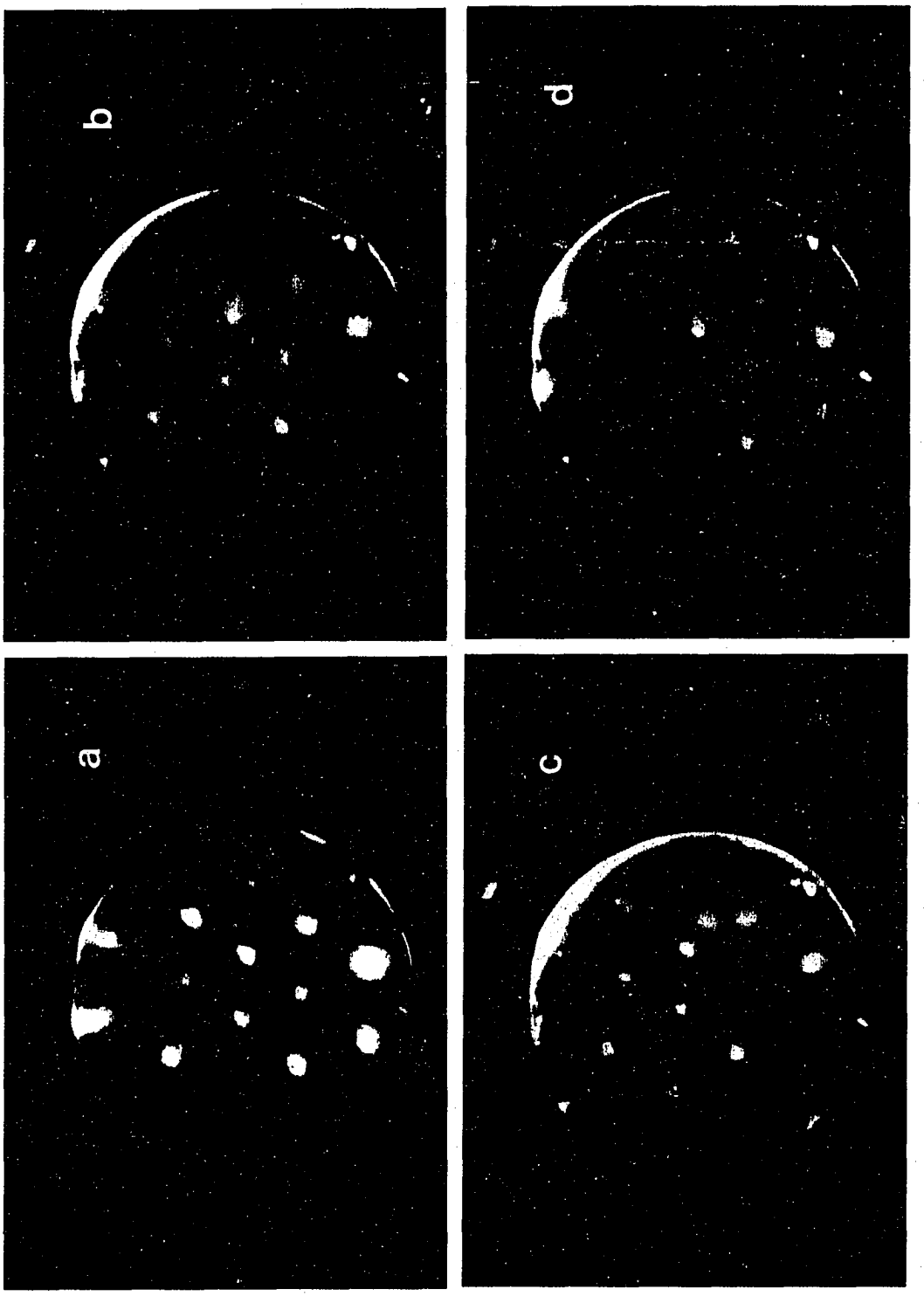
b
d
a
c

beams appear at 300 K, begin to split at 500 K, and disappear at 800 K, leaving the $\sqrt{3}$ pattern, which once again is gone by 1100 K.

3.2 ESDIAD

The identities of the positive ion products resulting from electron-stimulated desorption (ESD) are determined by focusing the desorbing species into the QMS with the ionizer current turned off. At all exposures and temperatures examined, F^+ is the dominant ESD product. Minor contributions from CF_n^+ species are observed, especially upon electron irradiation of the condensed multilayer. No I^+ is ever detected; interestingly, the I(511)/Ru(273) AES ratio shows no loss of iodine over 30 min continuous AES electron beam irradiation (2250 eV, 4 μA sample current) following a 75% saturation exposure of CF_3I at 100 K. Based on these observations, we interpret all ESDIAD images as being generated by ESD of F^+.

Figure 2 illustrates the temperature dependence of the ESDIAD image resulting from a multilayer CF_3I exposure at 100 K. Following adsorption, a broad, diffuse image is generated, attributable to a disordered multilayer. Following heating to 200 K, which results in desorption of both physisorbed and chemisorbed molecular CF_3I (table 1), the corresponding ESDIAD image is a circular spot, much sharper and more focused than in the 100 K case, indicating emission of F^+ normal to the crystal surface. This normal emission image remains unchanged until 700 K, when the lobes of a small hexagonal pattern begin to emerge beneath the strong center

Figure 2. ESDIAD images shown for a multilayer exposure of CF_3I as a function of temperature.

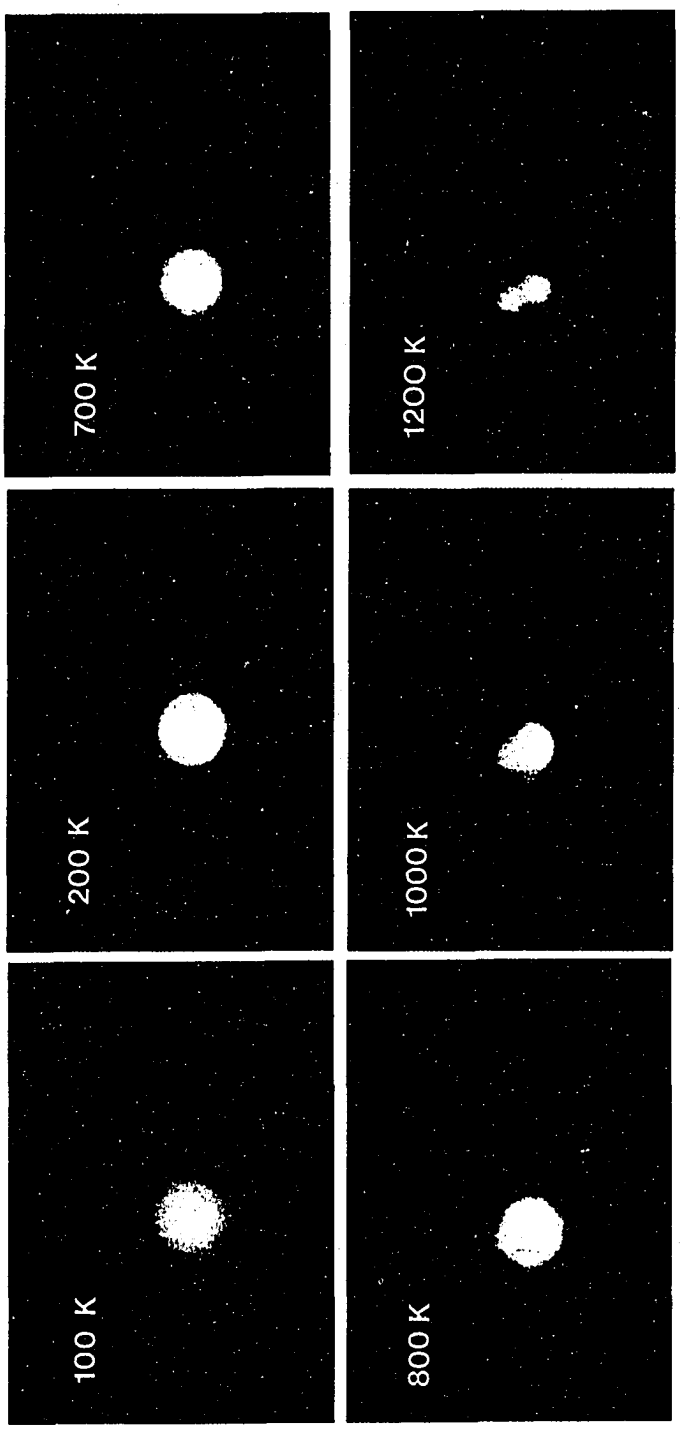
700 K
200 K
100 K
1200 K
1000 K
800 K

beam. These lobes become clearer at 800 K.

Heating to 1000 K results in a decrease in the normal emission intensity, thereby making the lobes of the small hexagon more visible. While the 1000 K photograph presented in fig. 2 shows only two of these lobes clearly, if the incident electron beam is rastered over the entire crystal surface, all six lobes can be seen, although rarely at the same time. After heating to 1200 K, the central spot and small hexagon are still visible, but with lower intensity. In this case, rastering the electron beam shows regions where all six lobes of the hexagon are plainly seen, but with no central spot. All ESDIAD features disappear by 1250 K.

Several coverage-dependent ESDIAD features are apparent. For instance, while the small hexagon-like pattern is first visible at 700 K after a multilayer CF_3I exposure, it is observed at lower temperatures for lower exposures. Figure 3 shows the ESDIAD image produced after heating a 30% saturation exposure to 400 K. Two somewhat unresolved lobes of the small hexagon are visible, along with a small normal emission spot; the advent of the small hexagon at 400 K for low CF_3I exposures is always accompanied by a decrease in the normal emission intensity. The behavior of this pattern upon annealing is similar to the multilayer case, except that the changes occur at somewhat lower temperatures: The central spot for the 30% saturation exposure disappears in some areas at 1100 K, with the entire image gone by 1150 K.

Also visible at low CF_3I exposures, albeit faintly, is a large hexagonal pattern, shown in fig. 4 for a 30% saturation exposure flashed to 500 K. (The small hexagon

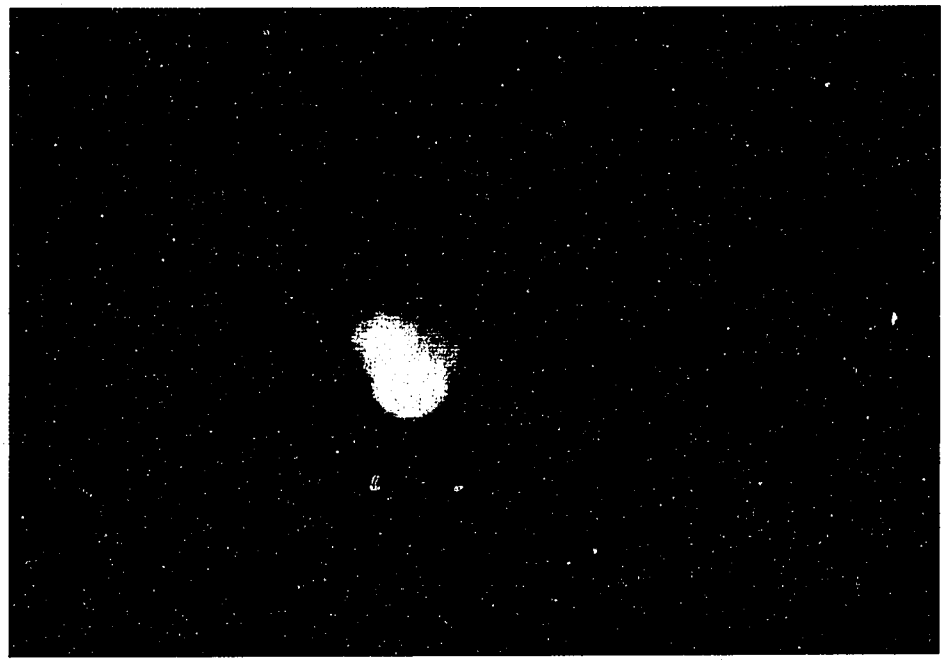

Figure 3. ESDIAD image from a 30% saturation CF_3I exposure following heating to 400 K showing development of the lobes of the small hexagon.

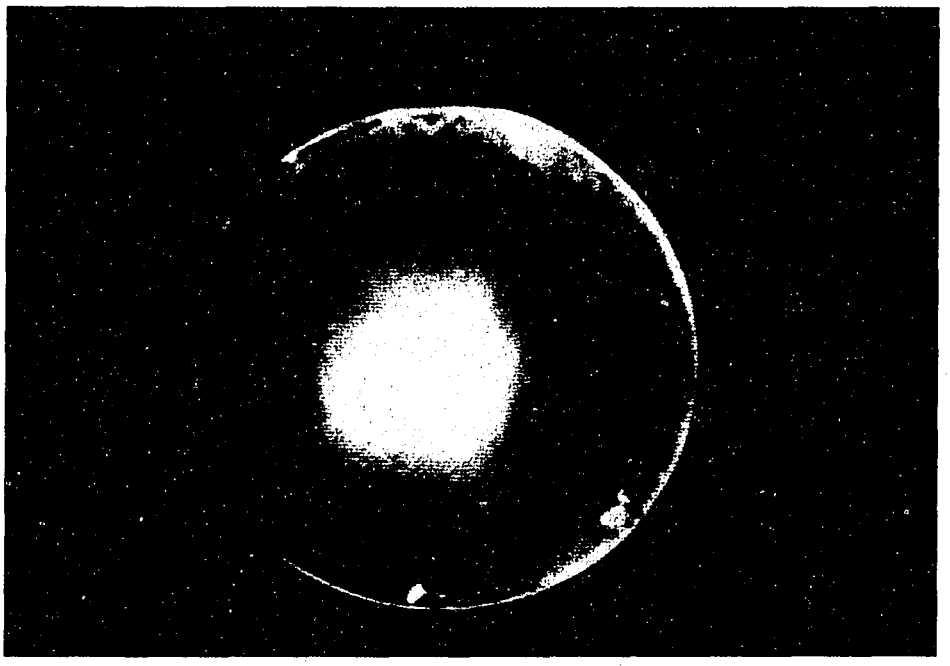

Figure 4. ESDIAD image from a 30% saturation CF_3I exposure following heating to 400 K. The MCP gain is increased to see the large hexagonal pattern.

is unresolved due to the high MCP gain.) This large hexagon is visible from the lowest exposures through approximately 50-60% saturation, first appearing at 400 K and disappearing by 600-700 K. The exact exposure where the image is no longer visible is difficult to determine since, as the CF_3I exposure approaches saturation, this large hexagon seems to become visible only with increasing electron fluence, indicating an electron-induced process. However, if a CF_3I exposure below 50% saturation is flashed directly to 500 K after dosing, this image is immediately visible over the entire crystal surface.

It should also be noted that a similar large hexagonal pattern is visible with the electron beam focused on the crystal edge, a photograph of which appears in ref. [7]. This pattern is visible at all CF_3I exposures, appearing at 200 K for low exposures and at 400 K for exposures closer to saturation. Regardless of exposure, this large hexagon from the crystal edge disappears by 800 K.

3.3 Surface Defect-related Chemistry

Much information can be gained regarding the influence of defect sites on the CF_3I chemistry by ion bombarding the crystal surface prior to adsorption. Of particular interest is the effect of defect sites on the observed ESDIAD images. In our experiments a defect-rich surface is prepared by Ar^+ sputtering for 15 min followed by annealing to 700 K to desorb residual background gases and embedded Ar. The resulting LEED pattern shows (1x1) spots on a diffuse background. CF_3I is then adsorbed at 100 K.

As demonstrated in fig. 5, surface defects greatly alter the thermal chemistry of CF_3I. Curve (a) shows the CF_3^+ TDS signal in the 300-1200 K temperature range following multilayer adsorption at 100 K. The CF_3 desorption state at 705 K is observed. (Smaller features at 510 and 590 K in curve (a) are due to electron beam damage, as discussed below, while the feature visible in both curves at 420 K is a result of desorption from the Ta supports following an abrupt increase in the heating rate at 400 K.) Curve (b) shows the CF_3^+ TDS signal resulting from the same CF_3I exposure onto a defect-rich surface. Curve (b) at first appears to show only a downward temperature shift of the features in curve (a). However, examination of the CF^+ and CF_2^+ TDS signals in the same temperature region (not shown) show that the large peak at 650 K is actually CF_4. The high temperature foot in curve (b) which extends to approximately 900 K is identified as CF_3.

Figure 6 shows the ESDIAD pattern observed after heating a 20% saturation CF_3I exposure on a defect-rich surface to 500 K. All six lobes of the small hexagon are now visible, with no central beam. The image does not change as the electron beam is rastered across the surface. A similar pattern is seen from all exposures up through saturation on the defect-rich surface, although as the exposure increases, the normal emission beam returns and intensifies. The large hexagonal pattern described above is seen at all CF_3I exposures on the defect-rich surface, but *only* on the edges of the crystal.

In an attempt to examine ESDIAD images generated by atomic fluorine, we turn to experiments involving adsorption of XeF_2. XeF_2 has previously been utilized

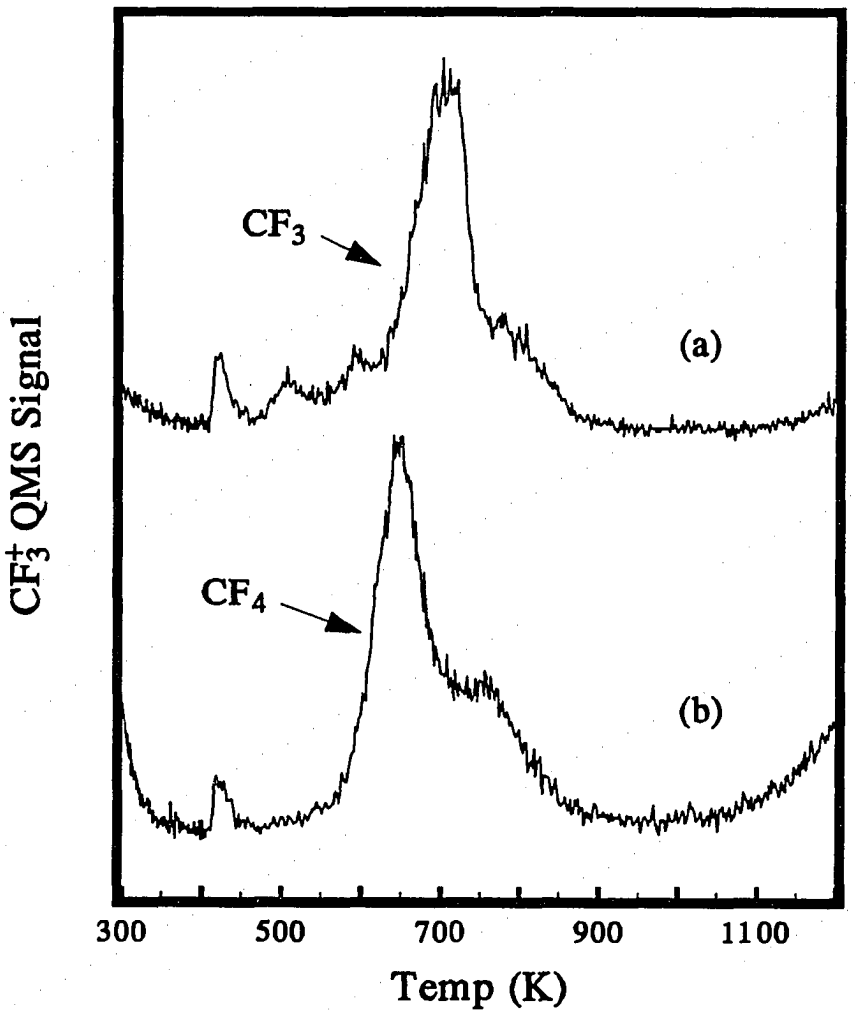

Figure 5. TDS signal for CF_3^+ resulting from a saturation exposure of CF_3I at 100 K onto (a) clean, well-annealed Ru(001), and (b) Ar^+ sputtered Ru(001) annealed to 700 K.

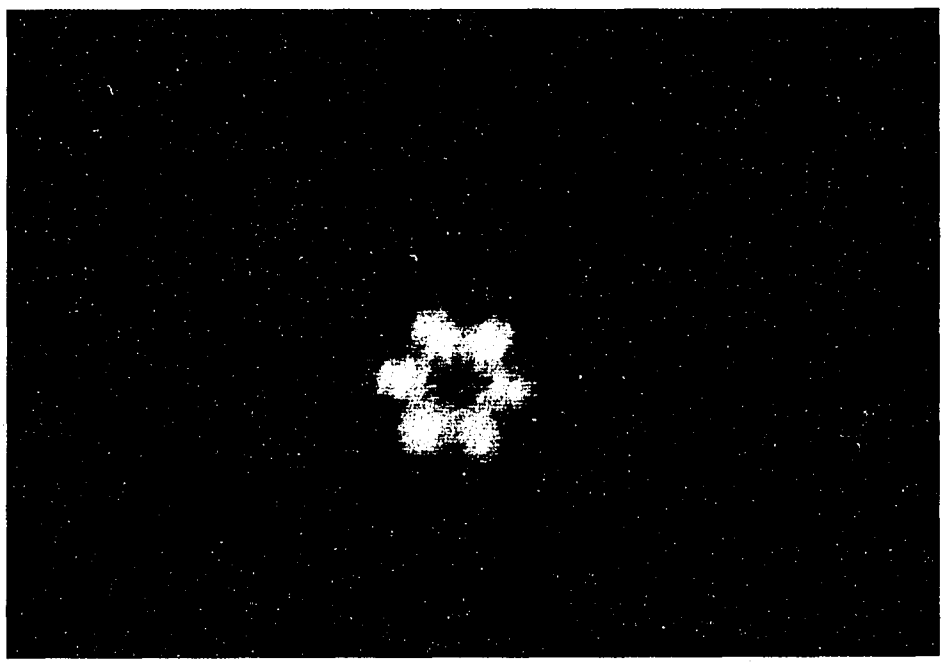

Figure 6. ESDIAD image showing all six lobes of the small hexagon from a 20% saturation CF_3I exposure at 100 K onto an Ar^+ sputtered, partially annealed surface. The particular image shown here follows heating to 500 K.

as a source of atomic fluorine on metal surfaces.[23] Figure 7 shows the ESDIAD image following exposure of XeF_2 onto a defect-rich surface at 300 K. A small hexagon, identical to that shown in fig. 6, is observed.

3.4 Electron-induced Chemistry

Great care must be taken during the ESDIAD experiment to distinguish between those features which accurately reflect the surface geometry of the adsorbate and those which are artifacts of the electron-induced chemistry. If, following a multilayer CF_3I exposure, one spot of the crystal is irradiated for an extended period of time with the focused electron beam, the ESDIAD images obtained from that spot upon subsequent annealing introduce a new pattern. This pattern, shown in fig. 8 for a multilayer exposure heated to 500 K following 5 min of electron bombardment, is a hexagonal image intermediate in size to the small hexagon of fig. 6 and the large hexagon of fig. 4. This intermediate hexagon is first visible at 400 K, disappearing by 700 K.

The entire crystal surface may be irradiated with low-energy electrons by placing a positive bias on the crystal and positioning it in front the QMS ionizer. If this procedure is used to electron bombard the entire crystal face for an extended length of time following a multilayer CF_3I exposure, heating the crystal to 500 K results in the intermediate hexagon of fig. 8 visible over the entire crystal surface. If this same sequence is followed, except with the molecular CF_3I first removed by heating to 200 K before electron irradiation, no intermediate hexagon is observed.

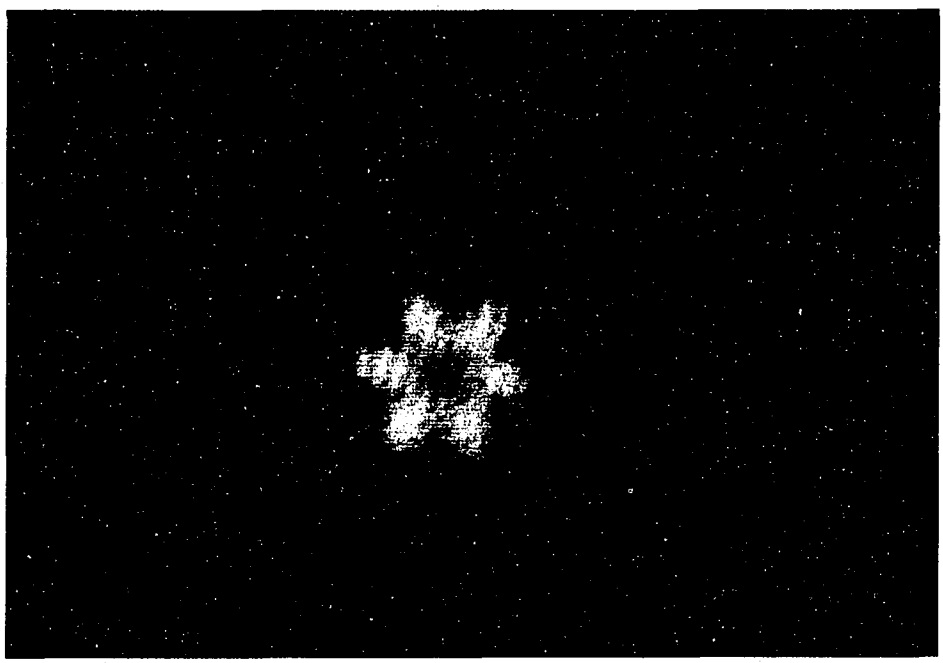

Figure 7. ESDIAD image resulting from XeF_2 exposure at 300 K onto an Ar^+ sputtered, partially annealed Ru(001) surface. The image seen here is after heating to 500 K.

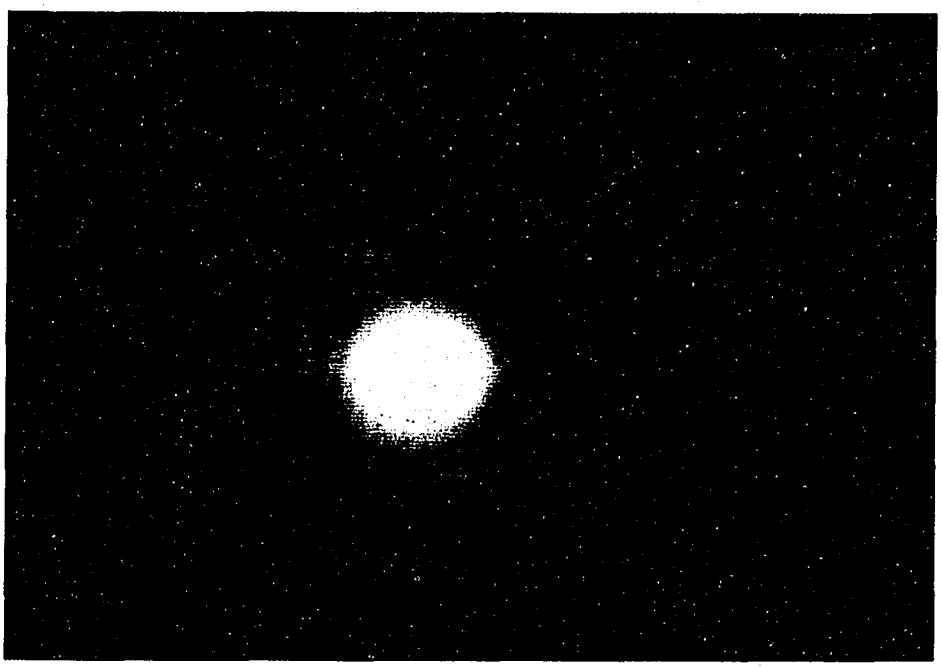

Figure 8. ESDIAD image showing intermediate hexagon which results from electron irradiation of multilayer CF_3I following adsorption at 100 K. The image shown is following heating to 500 K.

TDS following electron irradiation of the multilayer yields several new features, as illustrated by the CF_2^+ TDS spectra in fig. 9 of differing treatments of the same multilayer exposure of CF_3I. Curve (a) shows the normal TDS case for a multilayer exposure at 100 K, with the overranged multilayer state at 136 K, CF_3 at 705 K, and CF_2 at 1165 K. The spectrum shown in curve (b) results from first flashing the temperature to 200 K following the CF_3I dose, cooling to 100 K, and irradiating with electrons for 5 min. Curve (c) results from 5 min electron irradiation at 100 K immediately following the CF_3I exposure. Electron-induced decomposition (EID) of multilayer CF_3I is apparent, resulting in several new features between 200 and 700 K. It is interesting that the small features from curve (a) at 510 and 590 K seem to be enhanced in curve (c), indicating that electrons from the QMS ionizer cause a small amount of damage to the CF_3I multilayer during a normal TDS experiment.

4. Discussion

4.1 LEED

The LEED pattern we most commonly identify following CF_3I adsorption is the $(\sqrt{3}x\sqrt{3})R30^\circ$ pattern shown in fig. 1d, as it is seen for all exposures above 20% saturation. The disappearance of this pattern by 1100 K for all coverages coincides with the desorption of atomic iodine, as identified by TDS (table 1). Therefore, we are led to conclude that atomic iodine created by dissociation of CF_3I is adsorbed in a $(\sqrt{3}x\sqrt{3})R30^\circ$ configuration. Indeed, atomic iodine is known to adopt a

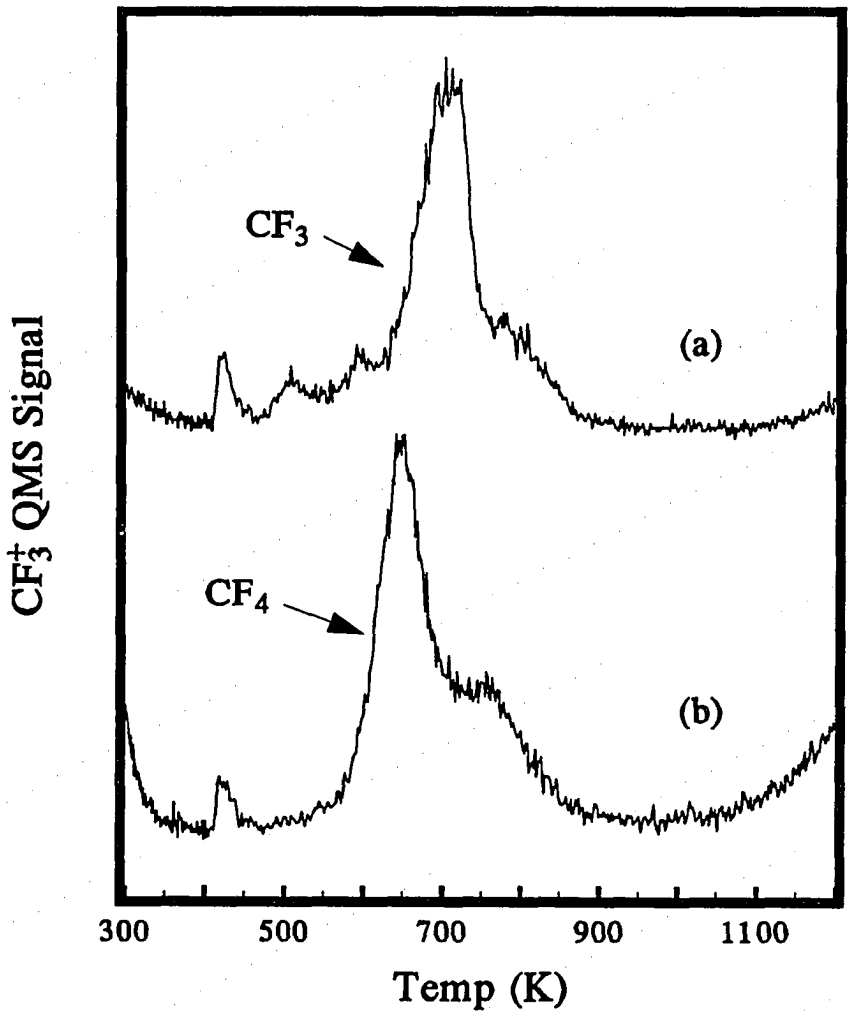

Figure 9. CF_2^+ TDS signal, from a multilayer CF_3I exposure, following: (a) CF_3I exposure at 100 K; (b) CF_3I exposure at 100 K, heating to 200 K, and 5 min low-energy electron bombardment at 100 K; (c) CF_3I exposure at 100 K, and 5 min low-energy electron bombardment at 100 K.

($\sqrt{3}$x$\sqrt{3}$)R30^{o} structure on other close-packed single crystal surfaces.[24,25] The observation of the $\sqrt{3}$ pattern at coverages as low as 20% of the saturation iodine coverage indicates localized ($\sqrt{3}$x$\sqrt{3}$) island formation.

The pattern showing 1/2-order spots is more difficult to interpret. As stated above, we are unable to distinguish between a p(2x2) surface structure and three domains of a p(2x1), as both generate the same LEED pattern. If, however, the four corners of the unit cell are occupied by iodine atoms, as we assume in the ($\sqrt{3}$x$\sqrt{3}$) structure, then a p(2x1) adlattice would place iodine atoms in adjacent surface sites, an impossible situation given the relative sizes of I (or I^{-}) and Ru. We speculate, therefore, that the LEED image shown in fig. 1b is due to a p(2x2) iodine adlattice. With this conclusion, we must explain the change, with increasing CF_3I exposure, from a ($\sqrt{3}$x$\sqrt{3}$) structure with an ideal coverage, θ_I, of 1/3, to a less dense p(2x2) structure with θ_I = 1/4. First, we note that the p(2x2) pattern appears to be related to the CF_3 desorption state at 705 K, as both are first observed at the same CF_3I exposure (67% saturation). Furthermore, all evidence of the p(2x2) pattern disappears at 800 K, after desorption of CF_3, resulting in the ($\sqrt{3}$x$\sqrt{3}$).

It appears, therefore, that the saturation level of I(ad) from CF_3I dissociation is less than the ideal value of 1/3--a conclusion similar to that noted for CF_3I on Ni(100) where TDS following electron-induced decomposition of the multilayer results in an I^+ desorption peak larger than the saturation value.[8] As the CF_3I exposure increases to a level where CF_3(ad) is stable due to a lack of available

surface sites for decomposition, the iodine atoms are adsorbed in a p(2x2) fashion. As surface sites are opened by desorption of CF_3, the iodine atoms are free to return to the more favorable ($\sqrt{3}x\sqrt{3}$) sites.

4.2 ESDIAD

A great deal of information regarding both the reactions of CF_3I and the resulting surface structure of the reaction products can be extracted from the ESDIAD results. At most temperatures and coverages, ESDIAD images resulting from CF_3I adsorption at 100 K are dominated by emission of F^+ at a desorption angle normal to the surface plane. An example is illustrated by the temperature dependence of the ESDIAD image following multilayer adsorption, shown in fig. 2. Upon desorption of molecular CF_3I, one central beam is visible, indicating normal emission of F^+. This pattern remains unchanged until CF_3 desorption begins at approximately 700 K. Since XPS shows that CF_3(ad) is the dominant fluorocarbon fragment present on the surface in this temperature range, the observance of a single normal emission beam has led us to conclude that CF_3(ad) groups are in a "tilted" configuration in which one C-F bond is oriented perpendicular to the surface plane while the trigonal pyramidal shape of CF_3 is retained.[7] HREELS results uphold this conclusion.[7] We add, however, that significant ESDIAD normal emission remains after desorption of CF_3, indicating that species other than CF_3(ad) contribute to this image as well.

In addition to normal emission, a number of other features are observed, most

notably three different sizes of hexagonal patterns, which provide valuable information regarding the surface processes. Ideally, we would like to be able to determine the desorption angles of the lobes of the various hexagonal patterns by rotating the zero-biased crystal under the electron beam until a specific lobe is positioned in the middle of the phosphor screen. Unfortunately, the non-linearity of our liquid nitrogen-coolable cold finger makes rotation of the crystal in this manner impossible.

The small hexagon is very interesting. Following a multilayer CF_3I exposure, we first see evidence of this pattern at 700 K (fig. 2), the same temperature at which XPS shows an increase in F(ad).[7] This pattern is somewhat clearer at 800 K as the intensity of the normal emission decreases with CF_3(ad) desorption. It remains until desorption of F(ad) at 1225 K. The visibility of the hexagonal lobes varies as the electron beam is rastered on the crystal surface, leading us to believe that the hexagon is generated by ESD from defect sites. This is verified by the ESDIAD image shown in fig. 6, following CF_3I adsorption on a defect-rich surface, in which all six lobes of the hexagon are clearly visible.

As stated above, the first appearance of the small hexagon in fig. 2 coincides with the growth of the F(ad) XPS peak, indicating that the small hexagon may be due to ESD of atomic fluorine. Further evidence is provided by the increase in CF_4 desorption, coupled with the decrease in CF_3 desorption, which results from a defect-rich surface, as shown by TDS in fig. 5. Although it is not clear which surface species combine to form CF_4, its growth indicates a substantial amount of C-F bond cleavage,

most likely resulting in an increase in the F(ad) concentration and the bright hexagonal ESDIAD image seen in fig. 6. Finally, the ESDIAD image generated by XeF_2 adsorption on the defect-rich surface (fig. 7) is identical to that generated by CF_3I on the same surface (fig. 6). Hence, we conclude that the small hexagonal ESDIAD pattern results from ESD of F(ad) adsorbed on defect sites.

The temperature at which the small hexagon first appears for a given coverage gives us information on C-F bond scission processes occurring on the surface. At low coverages, as we show in fig. 3, features of the small hexagon are apparent following annealing to 400 K. We have previously shown that C-F bonds, most probably from CF_3(ad), break between 200 and 400 K, producing F(ad) at low coverages, while ejecting CF_x fragments directly into the gas phase at higher coverages.[7] The appearance of the small hexagon at 400 K from a 30% saturation exposure, along with the corresponding decrease in normal emission intensity resulting from a loss of CF_3(ad), supports the low temperature model. We cannot determine, however, based on the ESDIAD results, whether C-F bond scission by 400 K at higher coverages results in F(ad). The high normal emission intensity in this temperature range for the higher coverages makes it impossible to identify any features of the small hexagon which may exist.

Interestingly, no other ESDIAD studies of fluorine-containing molecules report off-normal beams attributable to ESD of atomic fluorine. Of particular note, thermal defluorination of NF_3,[11] as well as electron-induced defluorination of PF_3,[20] is reported on Ru(001); neither study, however, reports the small hexagon we observe

from CF_3I on Ru(001). We do note that ESD-generated F^+ was detected desorbing at angles both normal and 30° off-normal from F/W(100), although no attempt was made to attribute the off-normal beam to a specific surface structure.[26]

Figure 10 shows possible adsorption sites for F(ad) which would result in the observed hexagonal ESDIAD image. A comparison of the reciprocal-space (1x1) LEED pattern for the clean surface (fig. 1a) with the real-space ESDIAD image (fig. 6) gives the desorption direction of the ESD species relative to the substrate orientation. We can see from fig. 10 that desorption of F(ad) from adsorption sites along the six step edge directions will generate the ESDIAD image we observe. These adsorption sites have somewhat arbitrarily been shown in fig. 10 as pseudo-bridging sites, instead of atop sites. This may not be an accurate representation as ESD is known to be more efficient from adsorption sites of reduced coordination.[27]

Also implied from fig. 10 is the generation of an ESDIAD normal emission beam from ESD of F(ad) on terraces. Given the high electronegativity of fluorine, we expect the adsorption sites of F(ad) to be the electron-rich 3-fold hollow sites, as indicated in fig. 10. The high coordination of these adsorption sites may lead to a very low cross-section for F(ad) ESD.[27] Indeed, an investigation by Madey into the ESDIAD behavior of oxygen on stepped W(110) surfaces has shown that no ESD O^+ emission is detected from the flat terraces, while intense O^+ emission is seen in the "downstep" direction from step edges.[28] However, an ESD investigation of F^+ from W(100) detects F^+ desorbing in a direction normal to the surface plane.[26] This implies ESD of atomic fluorine from crystal terraces and leads us to believe that ESD

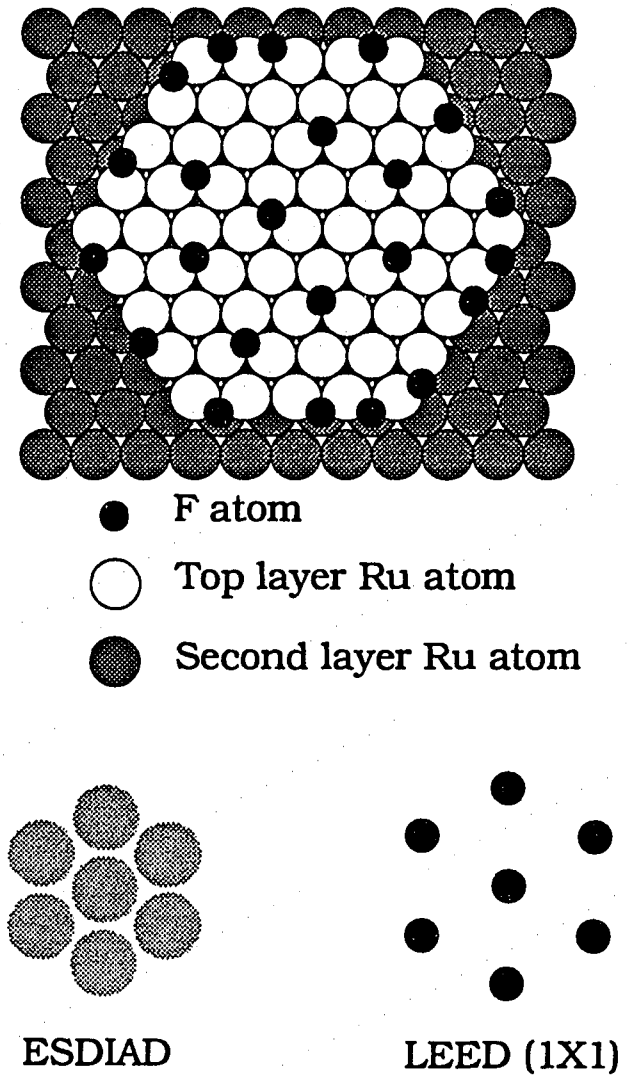

Figure 10. Adsorption sites of F(ad) on step edges and terraces of Ru(001) which may result in the small hexagonal ESDIAD image. The (1x1) LEED pattern gives the relative orientation of the desorbing species with respect to the substrate.

of terrace F(ad) contributes to the ESDIAD normal emission we observe.

Our results indicate that ESDIAD is much more sensitive to the detection of F(ad) than XPS. We have previously reported that XPS of CF_3I on Ru(001) detects no F(ad) above 900 K, although desorption of atomic fluorine is observed at 1226 K.[7] ESDIAD, on the other hand, identifies lobes of the small hexagon at 1200 K, which disappear by 1250 K. The sensitivity of ESD-based techniques toward fluorine detection is well-known, with detection limits as low as 3×10^9 atoms/cm^2 having been estimated for mass spectrometric detection of ESD-generated F^+.[10]

Moving the discussion to the large hexagon shown in fig. 4, we observe this image only at coverages below 50-60% saturation. Unlike the small hexagon discussed above, this image does not appear to be defect-related, as all six lobes are visible at all points on the surface. Furthermore, no evidence of the pattern is seen at any CF_3I coverage on the defect-rich surface. This large hexagon is never visible past 700 K, the temperature at which CF_3 desorption occurs for higher coverages. Therefore, we speculate that this large hexagon is generated by two domains of azimuthally ordered CF_3(ad) exhibiting C_{3v} symmetry. While we have shown that CF_3(ad) groups at saturation coverages are adsorbed in a tilted configuration,[7] coverages well below saturation may result in isolated CF_3(ad) species adopting a C_{3v} configuration.

It is interesting that as the CF_3I coverage increases above 60% saturation, the large hexagon may be visible, but only with increasing electron beam exposure. Once again, no evidence of this pattern is observed above 700 K. This implies that surface

fragments created by electron-induced decomposition (EID) may lead to structural changes in CF_3(ad). This is illustrated once again by the electron-beam damage experiments outlined in sec. 3.4. Figure 9 shows that a number of new desorption products result from EID of CF_3I multilayers. Although we have not attempted to identify these new species, it is likely that a number are due to carbon-carbon coupling reactions, as seen following low-energy electron irradiation of CF_3I multilayers on Ni(100).[8] The ESDIAD intermediate hexagon in fig. 8 resulting from the electron-irradiated multilayer is most likely generated by CF_3(ad) as desorption of this species (fig. 9) coincides with the disappearance of the hexagonal pattern. Once again, it seems that surface fragments created by EID alter the structure of CF_3(ad).

Finally, a brief discussion of CF_2(ad) is in order. XPS indicates a significant contribution from CF_2(ad) at temperatures below 700 K.[8] TDS shows a CF_2 desorption state at 1165 K.[2] Although this desorption state shows no recombinative characteristics, we have been unable to firmly attribute it to desorption of CF_2(ad) since neither XPS nor HREELS shows any indication of CF_2(ad) above 700 K.[8]

Our ESDIAD results show no special features attributable to CF_2(ad) at any temperature. The circular normal emission pattern which dominates at temperatures below 700 K points toward CF_2(ad) adsorbed in one of two possible orientations: (1) one C-F bond is oriented perpendicular to the surface plane and contributes to the normal emission, or (2) the molecular plane is oriented parallel to the surface plane and ESD-generated F^+ ions are undetectable by the ESDIAD optics. At this point we can not conclude which of these two scenarios is correct. The ESDIAD images

observed above 700 K offer little help as only normal emission and the small hexagon are observed. These images may result from F(ad) alone, or from F(ad) with CF_2(ad). A normal emission intensity decrease is observed in moving from 1000 K to 1200 K. However this may be due to the beginning of F(ad) desorption peaked at 1226 K and, therefore, cannot be concluded to result from desorption of perpendicularly oriented CF_2(ad).

5. Conclusions

LEED and ESDIAD have been used to study CF_3I adsorbed on Ru(001). A LEED investigation following CF_3I adsorption at 100 K identifies a $(\sqrt{3}x\sqrt{3})R30^{o}$ surface structure, with iodine atoms occupying the corners of the unit cell, for CF_3I exposures as low as 20% saturation. The low exposure at which this pattern first appears indicates island formation. As the CF_3I exposure increases to a level where CF_3 desorption at 705 K appears, a new LEED pattern showing 1/2-order spots is visible. This pattern is attributed to iodine atoms adsorbed in a p(2x2) surface structure. With heating, this p(2x2) pattern begins to split, eventually disappearing with desorption of CF_3(ad). Less surface crowding following CF_3 desorption allows iodine atoms to once again adopt the $(\sqrt{3}x\sqrt{3})$ structure.

ESDIAD of CF_3I on Ru(001) shows a variety of images which provide information about the reactions which occur on the surface, as well as the structure of the products which result from these reactions. A circular pattern resulting from

desorption of F^+ normal to the surface plane is the dominant image at most coverages and temperatures. This indicates that CF_3(ad) groups are bonded to the surface in a "tilted" configuration with one C-F bond oriented perpendicular to the surface plane.

As the crystal temperature is raised, new features become visible. These features appear to be lobes of a small hexagon emerging from beneath the normal emission spot. Sputtered surface experiments with CF_3I and XeF_2 clearly show all six lobes of this small hexagon, indicating it is generated by atomic fluorine adsorbed on step and defect sites. The observance of this pattern to 1200 K proves that, in this case, ESDIAD is much more sensitive to the presence of F(ad) than is XPS.

Two other hexagonal patterns are visible with ESDIAD. The first is a large hexagon which is visible only at low CF_3I exposures. This pattern disappears by 700 K, the same temperature at which CF_3 desorption is seen for higher coverages, indicating that it may be generated by two domains of CF_3(ad) adsorbed with C_{3v} symmetry. The other observed hexagon is intermediate in size to those previously described, and appears only from a multilayer exposure subjected to electron-induced decomposition (EID). It appears that EID fragments cause CF_3(ad) to adopt a new adsorption structure which generates the observed ESDIAD image.

6. Acknowledgments

This work is supported by Ames Laboratory, which is operated for the U.S. Department of Energy by Iowa State University under Contract No. W-7405-Eng-82. In addition, the work is supported by a GAANN Fellowship from the Department of Education (MBJ), and Grant No. CHE-9024358 from the National Science Foundation (PAT).

7. References

(1) Jones, R. G.; Singh, N. K. *Vacuum* **1988**, *38*, 213.

(2) Dyer, J. S.; Thiel, P. A. *Surf. Sci.* **1990**, *238*, 169.

(3) Liu, Z.-M.; Zhou, X.-L.; Kiss, J.; White, J. M. *Surf. Sci.* **1993**, *286*, 233.

(4) Castro, M. E.; Pressley, L. A.; Kiss, J.; Pylant, E. D.; Jo, S. K.; Zhou, X.-L.; White, J. M. *J. Phys. Chem.* **1993**, *97*, 8476.

(5) Armentrout, D. D.; Grassian, V. H. *Langmuir* **1994**, *10*, 2071.

(6) Sun, Z.-J.; Schwaner, A. L.; White, J. M. *Chem. Phys. Lett.* **1994**, *219*, 118.

(7) Jensen, M. B.; Myler, U.; Jenks, C. J.; Pylant, E. D.; White, J. M.; Thiel, P. A. *J. Phys. Chem.* submitted.

(8) Jensen, M. B.; Thiel, P. A. *J. Am. Chem. Soc.* **1994**, in press.

(9) Zaera, F. *Acc. Chem. Res.* **1992**, *25*, 260, and references therein.

(10) de Moraes, M.; Lichtman, D. *J. Vac. Sci. Technol. A* **1984**, *2*, 1595.

(11) Walczak, M. M.; Johnson, A. L.; Thiel, P. A.; Madey, T. E. *J. Vac. Sci. Technol. A* **1988**, *6*, 675.

(12) Madey, T. E.; Yates, J. T., Jr. *Surf. Sci.* **1977**, *63*, 203.

(13) Alvey, M. D.; Yates, J. T., Jr.; Uram, K. J. *J. Chem. Phys.* **1987**, *87*, 7221.

(14) Alvey, M. D.; Yates, J. T., Jr. *J. Am. Chem. Soc.* **1988**, *110*, 1782.

(15) Joyce, S. A.; Johnson, A. L.; Madey, T. E. *J. Vac. Sci. Technol. A* **1989**, *7*, 2221.

(16) Joyce, S. A.; Yarmoff, J. A.; Madey, T. E. *Surf. Sci.* **1991**, *254*, 144.

(17) Joyce, S. A.; Clark, C.; Chakarian, V.; Shuh, D. K.; Yarmoff, J. A.; Madey, T. E.; Nordlander, P.; Maschhoff, B.; Tao, H.-S. *Phys. Rev. B* **1992**, *45*, 14264.

(18) Johnson, A. L.; Joyce, S. A.; Madey, T. E. *Phys. Rev. Lett.* **1988**, *61*, 2578.

(19) Madey, T. E.; Joyce, S. A.; Yarmoff, J. A. In *Chemistry and Physics of Solid Surfaces VIII*; R. Vanselow and R. Howe, Ed.; Springer-Verlag: Berlin, 1990; Vol. 22; pp 55.

(20) Madey, T. E.; Nair, L.; Diebold, U.; Shivaprasad, S. M.; Johnson, A. L.; Poradzisz, A.; Shinn, N. D.; Yarmoff, J. A.; Chakarian, V.; Shuh, D. In *Desorption Induced by Electronic Transitions DIET V*; A. R. Burns, E. B. Stechel and D. R. Jennison, Ed.; Springer-Verlag: Berlin, 1993; Vol. 31; pp 182.

(21) Sack, N. J.; Nair, L.; Madey, T. E. *Surf. Sci.* **1994**, *310*, 63.

(22) Walczak, M. M.; Thiel, P. A. *Surf. Sci.* **1989**, *224*, 425.

(23) Loudiana, M. A.; Dickinson, J. T.; Schmid, A.; Ashley, E. J. *Appl. Surf. Sci.* **1987**, *28*, 311.

(24) Felter, T. E.; Hubbard, A. T. *J. Electroanal. Chem.* **1979**, *100*, 473.

(25) Forstmann, F.; Berndt, W.; Buttner, P. *Phys. Rev. Lett.* **1973**, *30*, 17.

(26) Park, C.; Kramer, M.; Bauer, E. *Surf. Sci.* **1981**, *109*, L533.

(27) Feibelman, P. J. In *Desorption Induced by Electronic Transitions DIET I*; N. H. Tolk, M. M. Traum, J. C. Tully and T. E. Madey, Ed.; Springer-Verlag: Berlin, 1983; Vol. 24; pp 61.

(28) Madey, T. E. *Surf. Sci.* **1980**, *94*, 483.

CHAPTER V. GENERAL CONCLUSIONS

The work presented in this dissertation examines the reactivity of trifluoroiodomethane (CF_3I) on Ni(100) and Ru(001) under both thermal and electron-induced conditions. The main conclusions are summarized as follows:

(a) A TDS investigation of CF_3I adsorbed on Ni(100) at 100 K identifies thermal desorption of CF_3I, NiF_2, I, and CF_3. Sub-monolayer molecular CF_3I desorbs in a broad state extending from 150 to 350 K. The peak areas associated with NiF_2 and I desorption increase monotonically with exposure before simultaneously reaching a saturation level. The CF_3 desorption state is small, and appears only at exposures approaching saturation. A model develops in which initial exposures of CF_3I completely decompose to C(ad), I(ad), and F(ad) on Ni(100). At exposures approaching saturation, the surface sites required for decomposition become filled, leading to stabilization of CF_3(ad).

(b) Low-energy electron ($E_i \leq 110$ eV) irradiation of multilayer CF_3I on Ni(100) results in electron-induced decomposition (EID) of the parent molecule. The cross-section for the process, σ_{EID}, is measured at 1.5×10^{-16} cm^2. The dominant product detected during electron irradiation is F^+, along with lesser amounts of HF^+, CF_n^+(n=1-3), I^+, and CF_3I^+. A significant amount of atomic iodine created via EID remains on the surface, as identified by post-EID TDS. Post-EID TDS also reveals a number of new desorption products, such as CF_2I and CFI, as well as new CF_n

(n=1,2,4) species. Of greater interest, however, is the identification of products of carbon-carbon bond formation reactions believed to occur in the multilayer during the EID process. C_2F_3I desorption is observed, as well as a mixture of C_2-C_4 species detected in one desorption state and thought to result from two or more reactions triggered by the same rate-determining step, possibly C_2F_5(ad) activation.

(c) The results of XPS and H_2 coadsorption experiments, in conjunction with results of an earlier TDS analysis, help to identify the thermal reactions of CF_3I adsorbed on Ru(001). Adsorption is both molecular and dissociative at 100 K. Heating to 200 K results in cleavage of the remaining C-I bonds, as well as partial defluorination of CF_3 to CF_2. Further C-F bond scission occurs between 200 and 400 K, due in part to activation by H(ad). As CF_3 desorption begins slightly below 700 K, surface sites become available for further CF_3, and possibly CF_2, decomposition. XPS shows evidence for recombination of surface fragments to form CF_3(g).

(d) At coverages and temperatures where XPS identifies CF_3(ad) as the dominant surface species, HREELS detects only one loss feature in the C-F stretching region. The frequency range in which this feature appears, 1202 to 1240 cm^{-1}, closely matches that for the asymmetric C-F stretch measured for CF_3 isolated in an argon matrix. The adoption of a similar assignment for CF_3(ad) on Ru(001) is upheld by ESDIAD experiments which detect emission of F^+ normal to the surface plane. CF_3(ad) is believed to retain its trigonal pyramidal shape, but to be configured in a "tilted" structure, with one C-F bond oriented perpendicular to the

surface.

(e) Several interesting ESDIAD patterns are observed following CF_3I adsorption on Ru(001). A small hexagonal image emerges at temperatures where XPS shows C-F bond scission to result in F(ad). Sputtered surface experiments with CF_3I, as well as with XeF_2, determine this pattern to be generated by ESD of F(ad) adsorbed at step edges. This image is visible even at F(ad) concentrations too low to be detected by XPS. A large hexagonal ESDIAD image, visible only at relatively low coverages, may be generated by low concentrations of C_{3v}-oriented CF_3(ad) isolated from surface crowding effects which result in the tilted CF_3(ad) configuration. A third hexagonal image, intermediate in size to those previously mentioned, results after electron irradiation of multilayer CF_3I, suggesting that EID fragments cause CF_3(ad) to adopt an orientation different from that in the non-EID case.

(f) A LEED study of CF_3I on Ru(001) indicates that iodine atoms formed as a result of C-I bond scission adsorb in $(\sqrt{3}x\sqrt{3})R30^{o}$ islands. As the initial CF_3I exposure increases to where desorption of CF_3 is detected, these atoms instead adopt a p(2x2) surface structure. Surface crowding is reduced following CF_3 desorption, and the iodine atoms are free to occupy the more favorable $(\sqrt{3}x\sqrt{3})$ sites.

APPENDIX I. LOCAL AND COLLECTIVE STRUCTURE OF FORMATE ON Pt(111)

A paper published in Surface Science Letters

Mark B. Jensen, Uwe Myler, and Patricia A. Thiel

Abstract

Formic acid adsorption and reaction on Pt(111) has been studied using LEED and ESDIAD. After conversion of the molecular formic acid (HCOOH) to formate (HCOO) a $(\sqrt{3}x\sqrt{3})R30^{o}$ LEED pattern is observed. This pattern is visible to 280 K, at which point the formate either recombines with H^{+} or decomposes. ESDIAD normal emission reaches a peak in intensity in the temperature region where the molecular plane of the formate is believed to be perpendicular to the surface plane.

1. Introduction

Since the pioneering work of Sexton in 1979 [1], there has been a great deal of work investigating the structure of formate on low-index metal surfaces with a wide variety of techniques. Most of this work has concerned the local (molecular) structure, leading to the common conclusion that formate bonds to the metal through one or both formate oxygens, with the O-C-O plane perpendicular to the surface plane and with the C-H bond pointing away from the surface [1-10]. On the

particular surface which is the subject of this report, Pt(111), there has been previous work with electron energy loss spectroscopy (EELS) indicating that formate exhibits these same characteristics, and in addition adopts a bridging configuration, i.e. a configuration in which the two oxygen atoms are equivalently bonded to two separate metal sites [2, 3]. This configuration is illustrated in fig. 1.

Work concerning the long-range (collective) structure of adsorbed formate is less plentiful. To our knowledge, the only positive report of such structure on a metal surface concerns Ni(110), where low-energy electron diffraction (LEED) shows a c(2x2) structure for formate at room temperature [5, 6]. A similar study of Pt(110) failed to reveal any adsorbate-induced superstructure [4]. Expanding the field of consideration beyond metals to semiconductors, evidence of an ordered structure has also been found for formate on GaAs(110) [11].

There are no previous reports of long-range formate structure, or attempts to find such, for Pt(111), the surface of this study.

Our goal is twofold. Electron-stimulated-desorption/ion-angular-distribution (ESDIAD) has proven very useful in determining the structure of surface-adsorbate systems, as evidenced in a recent review by Ramsier and Yates [12]. We want to determine whether the molecular orientation of adsorbed formate can be confirmed using ESDIAD, which has not previously been applied to any study of adsorbed formate. Second, we want to search for evidence of collective structure in the formate adlayer using LEED. A positive result would be the first of its kind for formate adsorbed on a hexagonal-close-packed metal surface, and only the second of its kind

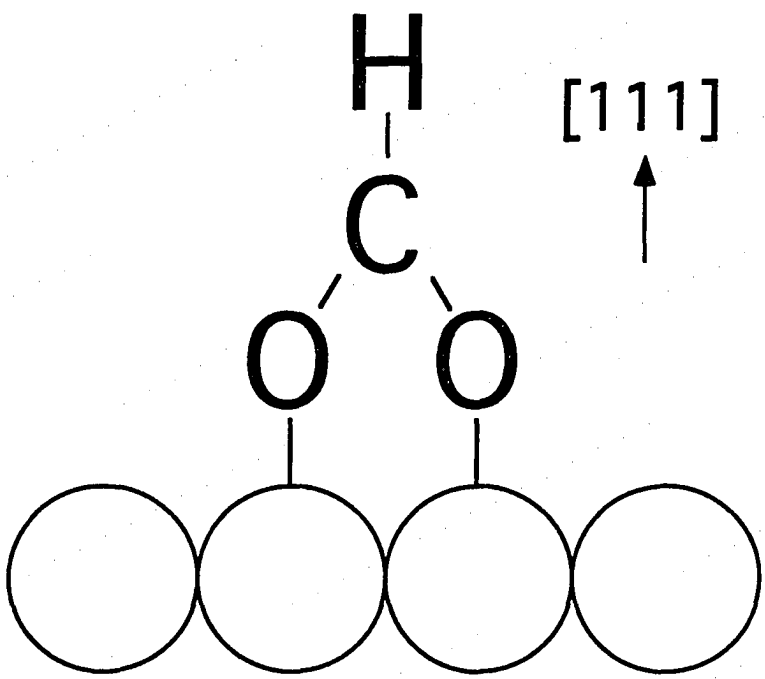

Figure 1. Bridging configuration of formate on Pt(111).

for formate adsorbed on any metal surface.

2. Experimental Description

The experiments are performed in an ion-pumped stainless steel UHV chamber with a base pressure of 2×10^{-10} Torr. The chamber, a cross-section of which has been given previously, is equipped for Auger electron spectroscopy (AES), ion bombardment, quadrupole mass spectrometry (UTI-100C), low-energy electron diffraction (LEED), electron-stimulated desorption-ion angular distribution (ESDIAD), and gas introduction [13].

The conventional ESDIAD apparatus [14, 15] can also be used to obtain LEED patterns. Images are collected by a CCD video camera interfaced to a personal computer for extraction of numerical data. The primary electron energy used in the ESDIAD experiments is 400 eV, with an electron current of 40 nA focussed into a spot of about 1 mm diameter on the crystal surface, which is biased at +40 V. This corresponds to a current density of 5.1×10^{-6} A cm^{-2} or 3.2×10^{-3} electrons s^{-1} $Å^{-2}$.

The Pt(111) single crystal is spotwelded to two tantalum wires, which in turn are in thermal contact with a liquid nitrogen reservoir. Temperature is monitored with a W5%Re-W26%Re thermocouple. The sample can be resistively heated to 1600 K, and cooled to 100 K within about five minutes.

Sample preparation, and its effect on surface chemistry, are described in a separate publication [16]. However, it must be noted that the maximum temperature

of the final high temperature anneal has a pronounced effect on the subsequent surface chemistry. A strong H^+ ESD signal is seen between 200 and 450 K (peaked at about 325 K) if the final temperature exceeds 1350 K. The temperature of 1250 K is used throughout this work because the resulting surface is clean according to AES and ESD, and also shows a sharp (1x1) LEED pattern.

The surface is exposed to formic acid by means of a directional doser, consisting of a conductance-limiting aperture with a diameter of 20 μm, and a spatially-collimating aperture in series. The pressure of formic acid in the dosing line is maintained at 20 mTorr, which is low enough to minimize dimerization of formic acid in the gas phase [17]. With this arrangement, the formic acid monolayer (as seen in the TDS spectra) is saturated after a dosing time of about 40 s, or a dose of about 800 mTorr-s. By comparison with the exposures of Columbia et al. [18] we conclude that 1800 mTorr-s is approximately equivalent to 1 L.

Before experiments, the formic acid (Aldrich, purity 99.6%) is purified further by several freeze-pump-thaw cycles with liquid nitrogen. Prior to every exposure, the dosing line and the doser are flushed several times with formic acid. We believe that this procedure saturates the walls of the dosing lines with formic acid (or a decomposition product), thus preventing further reactions. The long-term stability of the formic acid supply is checked by occasionally substituting fresh acid. No influence due to aging of the acid can be found.

3. Experimental Results

3.1 Thermal Desorption Spectra

Thermal desorption of formic acid following adsorption at 100 K is illustrated in fig. 2 for three exposures, equivalent to ca. 0.1, 0.4, and 1.1 L. These three exposures represent three distinct regimes [18-20]. For exposures less than 0.3 L HCOOH on clean Pt(111), the main desorption products are CO_2(g) with a peak temperature of 310 K, and H_2(g) with a peak temperature between 350 K and 390 K [18-20]. In addition, there is a molecular acid desorption peak (indicated by HCO^+, m/z=29) nearly coincident with CO_2 desorption. It should be pointed out that the CO_2 state at 310 K is not simply due to HCOOH cracking in the mass spectrometer, as the relative abundance of mass 44 is much greater than can be attributed to the high temperature HCOOH desorption state; furthermore, the peak temperatures differ by 20 degrees.

Above 0.3 L, molecular desorption occurs in three major states. The first grows in between 0.3 and 0.6 L with a peak temperature of 210 K. The other two states are populated above 0.6 L, exhibiting peak temperatures of 170 K at their first appearance but shifting upward with increasing exposure. The lowest temperature state is attributed to multilayer formic acid. All three major molecular states are populated in the upper curve of fig. 2c, although the two at lowest temperature are not resolved.

Vibrational studies allow correlation between the desorption states and surface species [2, 3]. Such work shows that the three low-temperature molecular states are

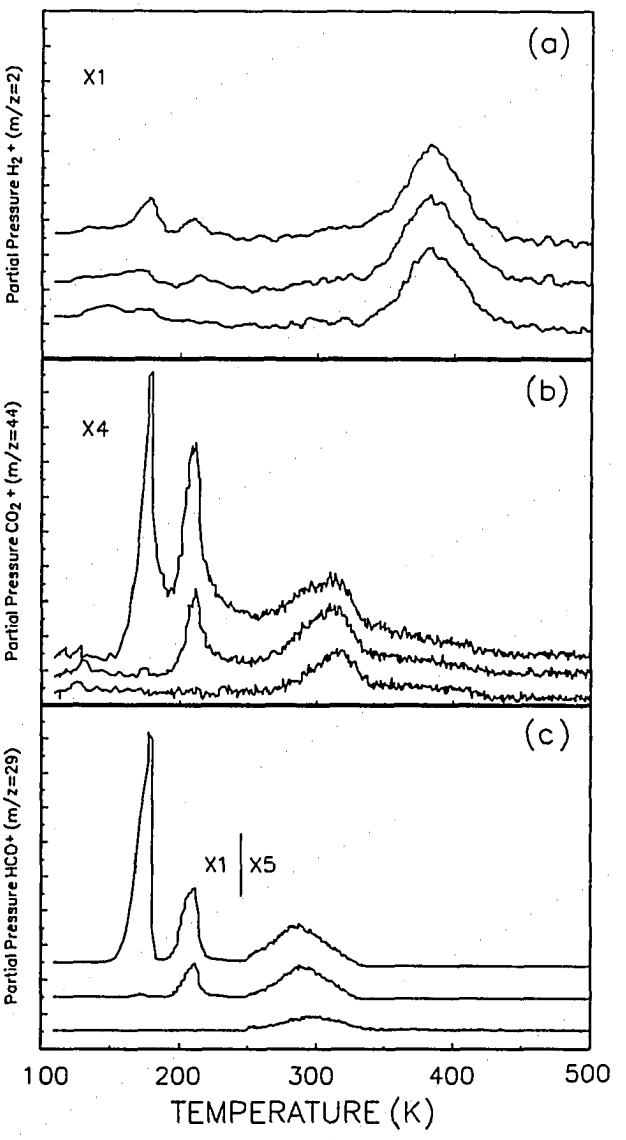

Figure 2. TDS results for three exposures of HCOOH on Pt(111) at 100 K with a heating rate of 2 K/s. Each box represents a different mass fragment. The lower curve in each box is for 0.1 L, the middle for 0.4 L, and the upper for 1.1 L. (a) mass 2, H_2^+. (b) mass 44 CO_2^+. (c) mass 29, HCO^+ (main cracking fragment of HCOOH).

associated with the multilayer and hydrogen-bonded adlayer of formic acid. Some formic acid dehydrogenates to formate at 130-170 K (depending on coverage); this formate begins to dehydrogenate further to CO_2 and H(ad) around 260 K. The 300 K state of formic acid is attributed to recombination between formate and H(ad). Presumably, it is nearly coincident with the CO_2 state because dehydrogenation and recombination are kinetically competitive. At higher temperatures, H(ad) combines to form molecular H_2(g), leaving the surface clean. The main result relevant to the present work is that formate is stable between ca. 170 and 260 K on Pt(111).

3.2. LEED

A $(\sqrt{3} \times \sqrt{3})R30^{\circ}$ LEED pattern is observed in almost exactly this temperature range where formate is stable, 170-260 K. After exposure to formic acid at 100 K, the LEED pattern is (1x1), but a high diffuse background is present. However, upon heating to 180 K the background begins to decline and a faint $\sqrt{3}$ pattern emerges. The background continues to fall, the $\sqrt{3}$ growing stronger, until a clear pattern is observed around 210 K. At higher temperatures, the $\sqrt{3}$ begins to fade and by 280 K it is gone. The fact that the $\sqrt{3}$ is observed in just the temperature range of formate stability leads us to assign the $\sqrt{3}$ pattern to adsorbed formate.

The superstructure is observed even at very low exposures (0.06 L), suggesting that formate suffers attractive interactions and island formation. The observation of a $\sqrt{3}$ superstructure implies that the associated ideal coverage is 1/3 (or--less

probably--some higher multiple). Based upon H_2 peak areas, we previously estimated that only 0.05 to 0.1 monolayer of HCOOH decomposes to CO_2 and H_2 [20]. Given that formate is the precursor to CO_2 and H_2, one would have expected the coverages determined with TDS (as described) and LEED to be more comparable. This discrepancy suggests that either (i) recombination is a significant channel for consumption of formate; or (ii) the surface is never completely covered by the $\sqrt{3}$-formate structure. The latter scenario can be rationalized if islands of $\sqrt{3}$-formate coexist with islands of hydrogen, or if the maximum coverage of formate is limited by the packing density of the parent adlayer.

3.3 ESDIAD

Meaningful interpretation of the ESDIAD patterns can be made only if the products of ESD are first identified. Upon irradiation of the formic acid multilayer by an independent electron beam, the mass spectrometer (with the ionizer off) detects desorption of species at 1, 2, and 29 amu. However, the intensity of the H^+ (1 amu) signal is approximately 20 times more intense than that of the other two species. No desorption of CO_2^+ is detected. The dominance of the H^+ signal over that of the other ESD species allows us to identify any ESDIAD images as being generated by H^+.

The model for formic acid/formate chemistry on Pt(111) postulated by Avery [2] and confirmed by Columbia, et al. [3] allows prediction of specific ESDIAD

behavior. In this model, adsorption at low temperature is molecular, with the formic acid adopting a configuration similar to the solid phase, hydrogen-bonded alpha- and beta-polymorphs. In both of these structures, the C-H and O-H bonds are nearly parallel to the surface plane, which should make them ESD-inactive for H^+ emission [21, 22]. Upon heating, the formic acid converts to formate, which adopts C_{2v} symmetry with the C-H bond now perpendicular to the surface plane. It is from this species that one expects to see strong normal emission of H^+ from the ESD of the acyl hydrogen.

ESDIAD images at selected temperatures are shown in fig. 3 for exposures in each of the three exposure regimes. The first picture in each group is taken immediately after adsorption at 105 K. The second is taken after heating to a temperature where formate should be the dominant species on the surface, and the third after heating to a temperature where, according to TDS and EELS, no adsorbates remain [2, 3].

Normal emission is the sole ESDIAD pattern observed. After an exposure of 0.1 L at 105 K, there is weak normal emission; this image intensifies upon heating to 200 K, and almost disappears again after heating to 500 K. The variation of its integrated intensity as a function of temperature is shown in fig. 4 (bottom curve). This figure shows that the intensity passes through a maximum at about 200 K. After an exposure of 0.4 L at 105 K, the normal emission is stronger. Again, upon heating, the intensity passes through a maximum, this time at 200-230 K; at higher temperature, it falls again to background levels. A similar pattern is displayed upon

Figure 3. ESDIAD images as a function of temperature for three separate exposures of HCOOH on Pt(111). All photographs were taken at T<170 K. (a) 0.1 L, 105 K. (b) 0.1 L, 200 K. (c) 0.1 L, 500 K. (d) 0.4 L, 105 K. (e) 0.4 L, 200 K. (f) 0.4 L, 500 K. (g) 1.1 L, 105 K. (h) 1.1 L, 230 K. (i) 1.1 L, 500 K.

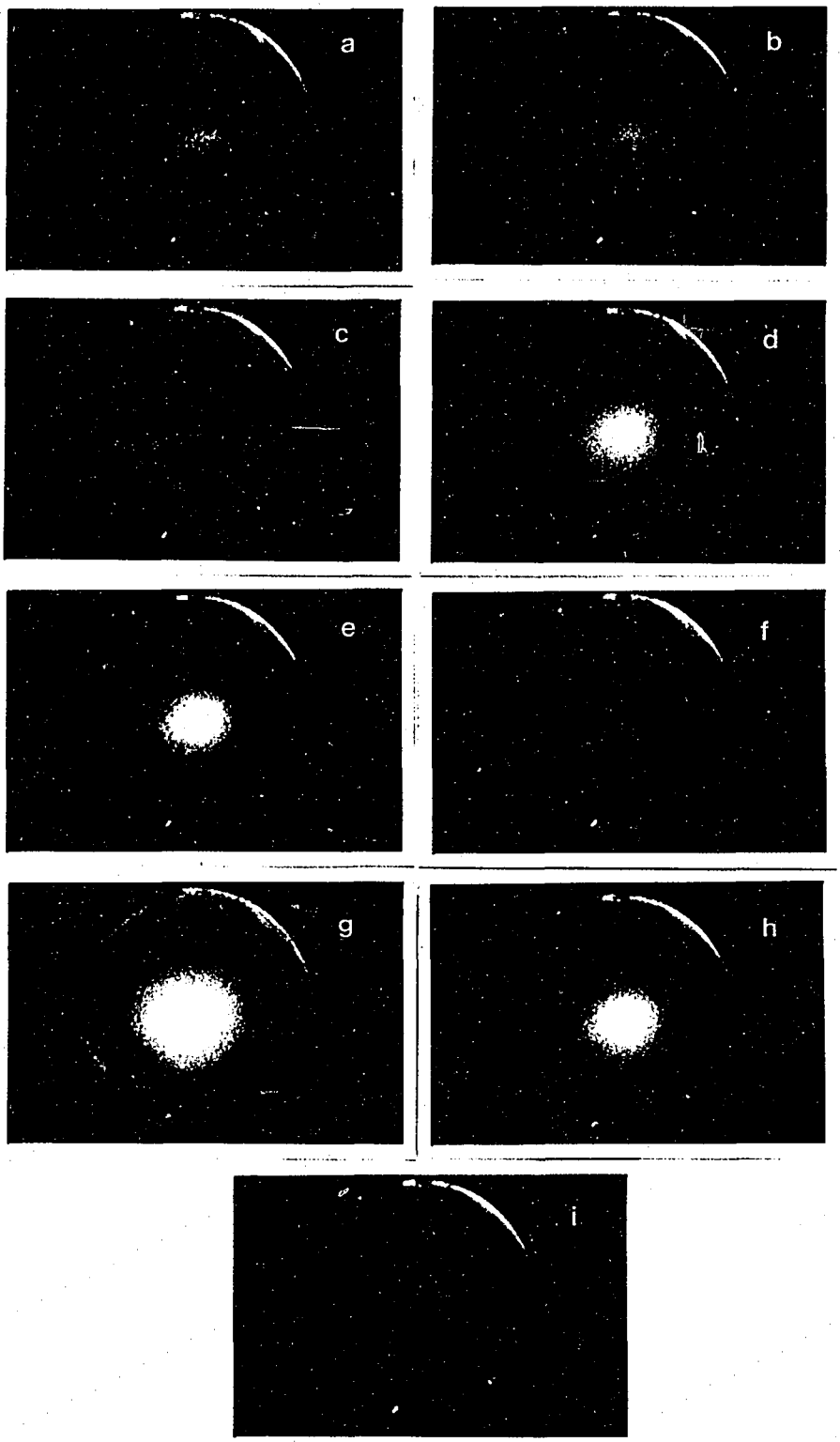
a
b
c
d
e
f
g
h
i

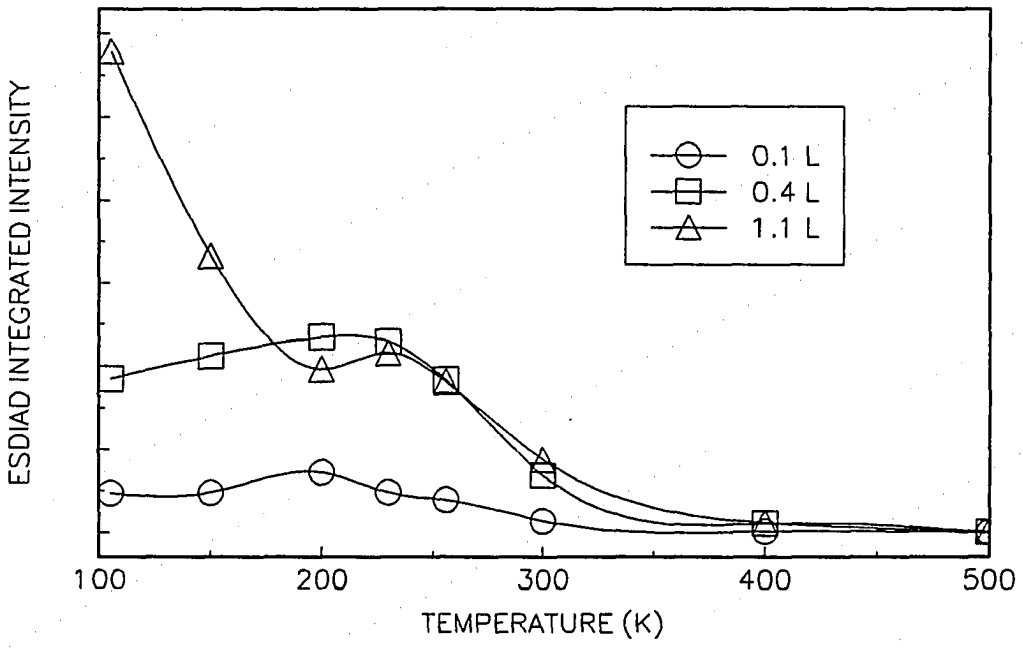

Figure 4. **Total integrated intensity of the ESDIAD normal emission as a function of temperature for 0.1, 0.4, and 1.1 L HCOOH on Pt(111).**

exposure of 1.1 L, although in this case the initial intensity at low temperature is much higher (cf. fig. 4) and the emission spot is much broader (cf. fig. 3g).

In each case, a local maximum in integrated spot intensity occurs at 200-230 K, in the middle of the temperature range where formate is believed to be stable (170-260 K). Thus, we propose that these data support the assignment of formate to a perpendicular geometry, as shown in fig. 1, and associate the maximum intensity in this temperature range with H^+ emission from the C-H bond of the formate. In each case also, the intensity of this normal emission reaches background levels after the sample is heated to a point where only H(ad) remains.

As can be seen from figs. 3a, 3d, and 3g, normal emission is also observed upon exposure at low temperature, 105 K. At 1.1 L, normal emission is very intense, and could be attributable to ESD from a disordered multilayer. The thermal desorption data of fig. 2 show that the multilayer state is well populated at this exposure. More puzzling, however, are the data for 0.1 and 0.4 L exposures, where normal emission is also significant at 105 K (although sharper in comparison to 1.1 L, as indicated by a 20% decrease in the full-width of the emission peak at the lower exposures). The thermal desorption data of fig. 2 show that the multilayer state is absent at 0.1 and 0.4 L exposures. In the model proposed by Columbia, et al. [3], only the acid polymorph is present under these conditions, with C-H and O-H bonds lying parallel to the surface. One possible explanation is that there is some electron-induced decomposition of the parent formic acid. Several studies have shown the susceptibility of oxygenated organic compounds to electron beam damage

[23-25]. Crowell et al. observed changes in the vibrational spectra of formic acid and formate adsorbed on Al(111) following electron bombardment [25]. After sufficient electron fluences, both species were found to decompose to elemental carbon and oxygen. We estimate that if the cross-section for electron-induced dissociation in our experiments is 10^{-15} cm^2 (a worst-case estimate), then the rate of decomposition would be approximately 0.01 monolayer/s. Another possibility is that there is some local disorder on the surface following adsorption at low temperature, resulting in the normal emission we observe. At present, we cannot judge which of these two possibilities is correct.

For each exposure, there is little to no ESD activity above 350 K, as shown by fig. 4. Above 300 K, the surface is covered with only H(ad), and by 450 K, desorption of H_2 is complete, leaving an adsorbate-free surface. In a separate experiment, exposing the clean surface to a saturation coverage of H_2 at 100 K gave no ESDIAD signal. This is in agreement with previous results by Lanzillotto et al. [26] which showed that, for Ni(111), alkali sensitization was necessary for detection of adsorbed atomic hydrogen by ESDIAD. It is a common observation that the cross section for rupture of an internal bond in an adsorbed molecule is greater than the cross section for rupture of a metal-atom bond [27]. Therefore, we attribute the absence of significant ESDIAD emission above 350 K to an ESD-inactive, hydrogen-covered surface, and above 450 K to an adsorbate-free surface.

4. Conclusions

In summary, we report the first observation of long range order of formate adsorbed on a close-packed surface. A $(\sqrt{3} \times \sqrt{3})R30^{o}$ LEED pattern is observed in the temperature region where EELS shows formate to be stable on the surface. We have also used the ESDIAD technique to confirm the molecular orientation of the formate. The total integrated intensity of the H^{+} normal emission shows a reproducible peak in the temperature region where formate exists. We take this as evidence that the C-H bond (and the formate molecular plane) is perpendicular to the surface.

5. Acknowledgments

Acknowledgment is made to the Donors of the Petroleum Research Fund, administered by the American Chemical Society, for the support of this research. Some equipment and all facilities are provided by the Ames Laboratory, which is operated for the U.S. Department of Energy by Iowa State University under Contract No. W-7405-ENG-82.

6. References

1. B. A. Sexton, Surf. Sci. 88 (1979) 319.
2. N. R. Avery, App. Surf. Sci 14 (1982-83) 149.
3. M. R. Columbia, A. M. Crabtree and P. A. Thiel, J. Am. Chem. Soc. 114(1992) 1231.

4. P. Hofmann, S. R. Bare, N. V. Richardson and D. A. King, Surf. Sci. 133(1983) L459.

5. T. S. Jones, N. V. Richardson and A. W. Joshi, Surf. Sci. 207 (1988) L948.

6. T. S. Jones, M. R. Ashton and N. V. Richardson, J. Chem. Phys. 90 (1989) 7564.

7. J. Ushio, I. Papai, A. St-Amant and D. R. Salahub, Surf. Sci. Lett. 262 (1992) L134.

8. S. P. Mehandru and A. B. Anderson, Surf. Sci. 219 (1989) 68.

9. D. P. Woodruff, C. F. McConville, A. L. D. Kilcoyne, T. Lindner, J. Somers, M. Surman, G. Paolucci and A. M. Bradshaw, Surf. Sci. 201 (1988) 228.

10. C. Houtman and M. A. Barteau, Surf. Sci. 248 (1991) 57.

11. R. Matz and H. Luth, Surf. Sci. 117 (1982) 367.

12. R. D. Ramsier and J. T. Yates Jr., Surf. Sci. Rep. 12 (1991) 243.

13. M. M. Walczak and P. A. Thiel, Surf. Sci. 224 (1989) 425.

14. T. E. Madey in: The Use of Angle-Resolved Electron and Photon Stimulated Desorption for Surface Structural Studies, Vol. 17, Eds. E. Taglauer and W. Heiland (Springer-Verlag, Berlin, 1981) p. 80.

15. J. T. Yates Jr., M. D. Alvey, M. J. Dresser, M. A. Henderson, M. Kiskinova, R. D. Ramsier and A. Szabo, Science 255 (1992) 1397.

16. U. Myler and M. B. Jensen, in preparation (1992).

17. J. B. Benziger and G. B. Schoofs, J. Phys. Chem. 88 (1984) 4439.

18. M. R. Columbia, A. M. Crabtree and P. A. Thiel, Surf. Sci. 271 (1992) 139.

19. M. R. Columbia and P. A. Thiel, Proc. DOE Workshop -Direct Methanol/Air Fuel Cells to be published (1990).

20. M. R. Columbia and P. A. Thiel, Surf. Sci. 235 (1990) 53.

21. Z. Miskovic, J. Vukanic and T. E. Madey, Surf. Sci. 169 (1986) 405.

22. Z. Miskovic, J. Vukanic and T. E. Madey, Surf. Sci. 141 (1984) 285.

23. J. G. Chen, J. E. Crowell and J. T. Yates Jr., Surf. Sci. 172 (1986) 733.

24. P. Basu, J. G. Chen, L. Ng, M. L. Colaianni and J. T. Yates Jr., J. Chem. Phys. 89 (1988) 2406.

25. J. E. Crowell, J. G. Chen and J. T. Yates Jr., J. Chem. Phys. 85 (1986) 3111.

26. A.-M. Lanzillotto, M. J. Dresser, M. D. Alvey and J. T. Yates Jr., J. Chem. Phys. 89 (1988) 570.

27. T. E. Madey, D. E. Ramaker and R. Stockbauer, Ann. Rev. Phys. Chem. 35 (1984) 215.

APPENDIX II. DESCRIPTION OF THE LEED/ESDIAD SYSTEM

I. INTRODUCTION

Electron-stimulated desorption ion angular distribution (ESDIAD) is a powerful tool for studying the geometries of adsorbates on surfaces. Several excellent reviews have been written covering both ESDIAD [1,2] and the ESD process [3,4]; the interested reader is referred to these sources for information on the fundamentals and applications of this technique.

The purpose of this appendix is to describe the specific instrument, as well as the experimental method, used to collect both the ESDIAD and LEED images presented in the main body of this dissertation. It is hoped that this description will provide future operators with the necessary practical information to successfully perform the experiment.

II. INSTRUMENT CONFIGURATION

A. Overview

A general schematic diagram of the LEED/ESDIAD system is shown in fig. 1. An electron beam incident on the target causes desorption of ions and neutrals via electron-stimulated desorption (ESD). In our system, only positive ions are detected. These ions, desorbing at angles equivalent to the parent chemical bond angles, are focused through three electrostatic mesh grids, two hemispherical and one planar.

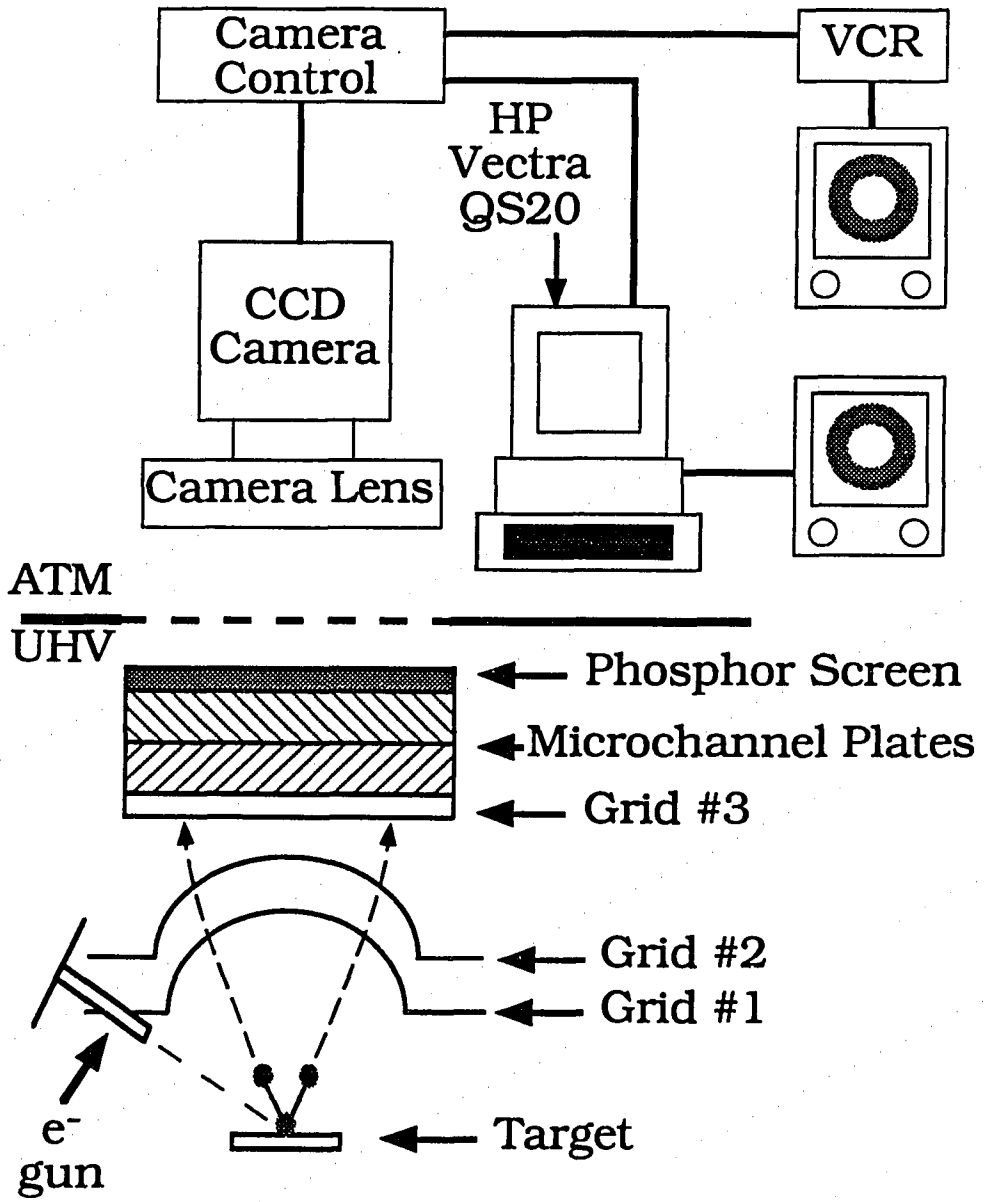

Figure 1. The basic components of the LEED/ESDIAD system.

The ion signal is amplified and converted to an electron signal by a dual microchannel plate (MCP) assembly. This electron signal, imaged onto a phosphor screen and monitored with a CCD camera, can be viewed on a video monitor and recorded with a videocassette recorder; the image may also be fed to a computer with a video processor board for numerical analysis.

B. Electronic Components

A Perkin-Elmer PHI 11-010 electron gun control is used with a PHI Model 04-015 grazing incidence electron gun to generate the electron beam incident on the target. A bias is applied to the target with a HP 62128 power supply, and the current is monitored with a Keithley 485 autoranging picoammeter.

While grid #1 is grounded through a grounding pin, a bias is applied to grid #2 by one of two Kepco PCX 100-0.2 MAT voltage regulators. One of these is configured for operation in the ESDIAD mode, the other for the LEED mode; these configurations are discussed in sections C and D. Grid #3 is biased with a Bertan Model 301 power supply, while a high voltage is applied to the phosphor screen with a Bertan Model 205A-05R high voltage power supply.

A homemade voltage divider box supplies the appropriate voltages to the MCP's. As shown in table 1, these voltages are dependent upon which mode, ESDIAD or LEED, is utilized.

Figure 2 labels the appropriate feedthroughs for connecting the power supplies to the optics system.

Table 1. Measured output voltages supplied to the microchannel plates by the voltage divider box.

Pot. Setting	ESDIAD Mode			LEED Mode		
	Inner (V)	Middle (V)	Outer (V)	Inner (V)	Middle (V)	Outer (V)
100	-99	0	94	47	145	254
200	-197	0	187	94	289	506
300	-295	0	281	142	435	752
400	-393	0	374	192	581	1005
500	-488	0	466	254	773	1265
600	-587	0	558	308	930	1520
700	-686	0	652	361	1086	1772
800	-794	0	748	416	1254	2041
900	-896	0	844	473	1423	2312
1000	~(-1000)	0	993	585	1591	2593

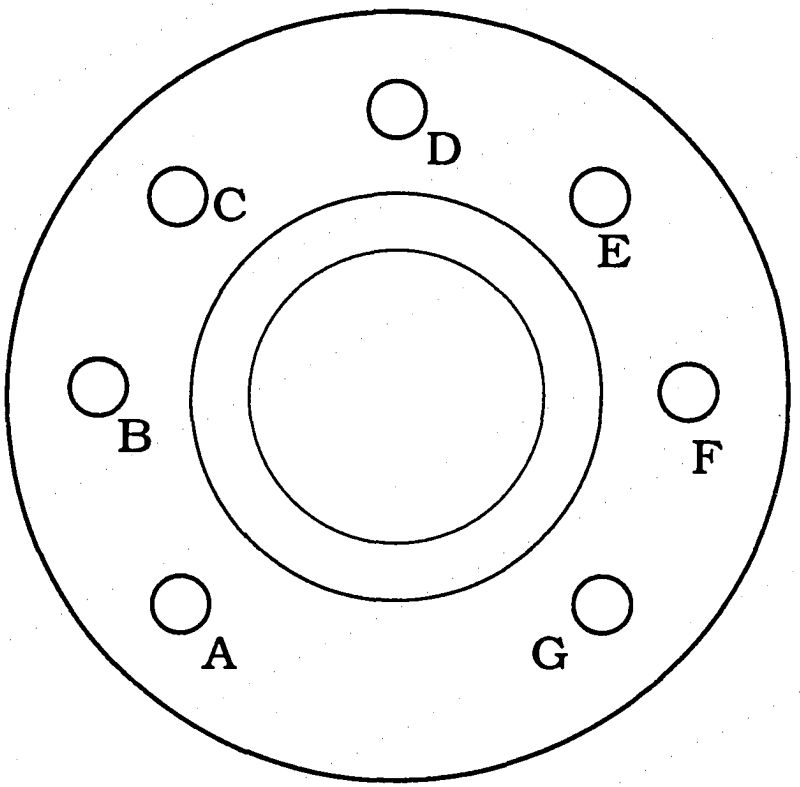

A:	INNER MCP
B:	MIDDLE MCP
C:	OUTER MCP
D:	SCREEN
E:	GRID #3
F:	GRID #2
G:	GRIN #1

Figure 2. Feedthrough connections for the LEED/ESDIAD optics system.

C. ESDIAD Mode

Figure 3 shows the configuration, specific to the ESDIAD experiment, for the sample bias power supply, the picoammeter, and the grid #2 (G2) power supply. In this configuration the voltage applied to G2 is referenced to the sample bias. Therefore, since G1 is grounded, G2 acts as an ion suppressor. For example, a +40 V sample bias and a +4 V G2 power supply reading will result in only ions with a desorption energy above 4 eV passing through G2 to G3. Since G2 is referenced to the sample bias, this cut-off energy remains constant if the sample bias is varied.

D. LEED Mode

The specific configuration for the LEED experiment is shown in fig. 4. The G2 voltage is now referenced to the electron beam energy through a t-connection at the filament output (F2) on the rear panel of the electron gun control. Instead of acting as an ion suppressor, as in the ESDIAD mode, G2 now serves as an electron suppressor. As an example, a primary electron beam setting of -250 V and a G2 power supply setting of +10 V means that electrons must have an energy of at least 240 eV to pass G2. Therefore, G2 establishes an energy acceptance window which will remain constant if the energy of the primary electron beam is changed.

III. PERFORMING THE EXPERIMENT

It is important that a narrowly focused electron beam be used for the ESDIAD experiment. For this reason an aluminum flag with a phosphor coating is

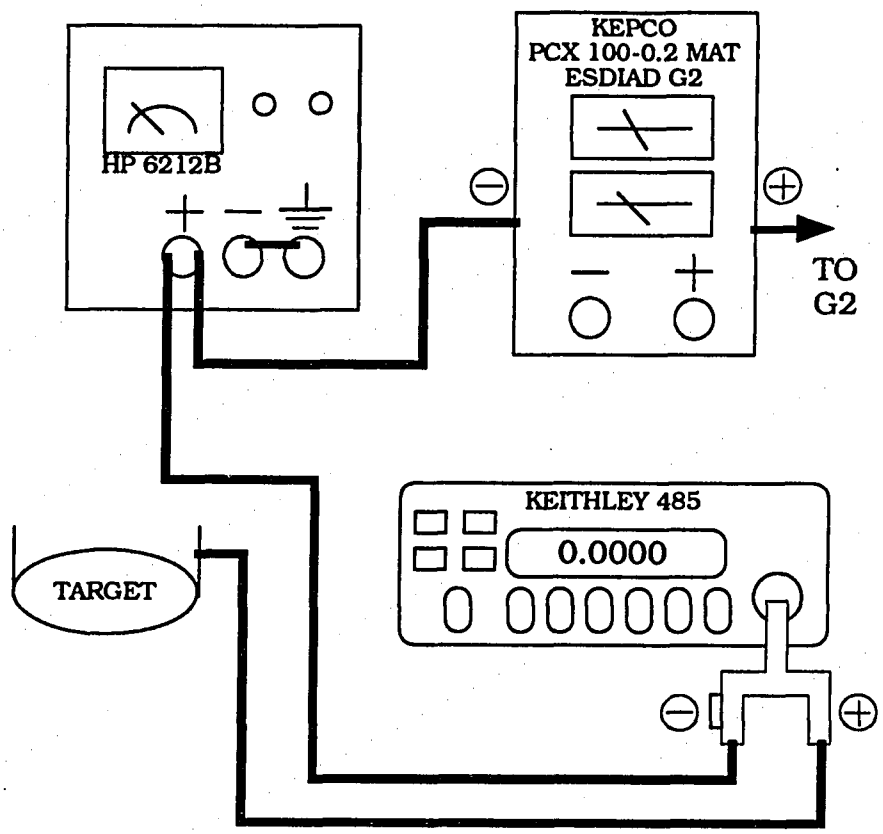

Figure 3. Experimental configuration for ESDIAD.

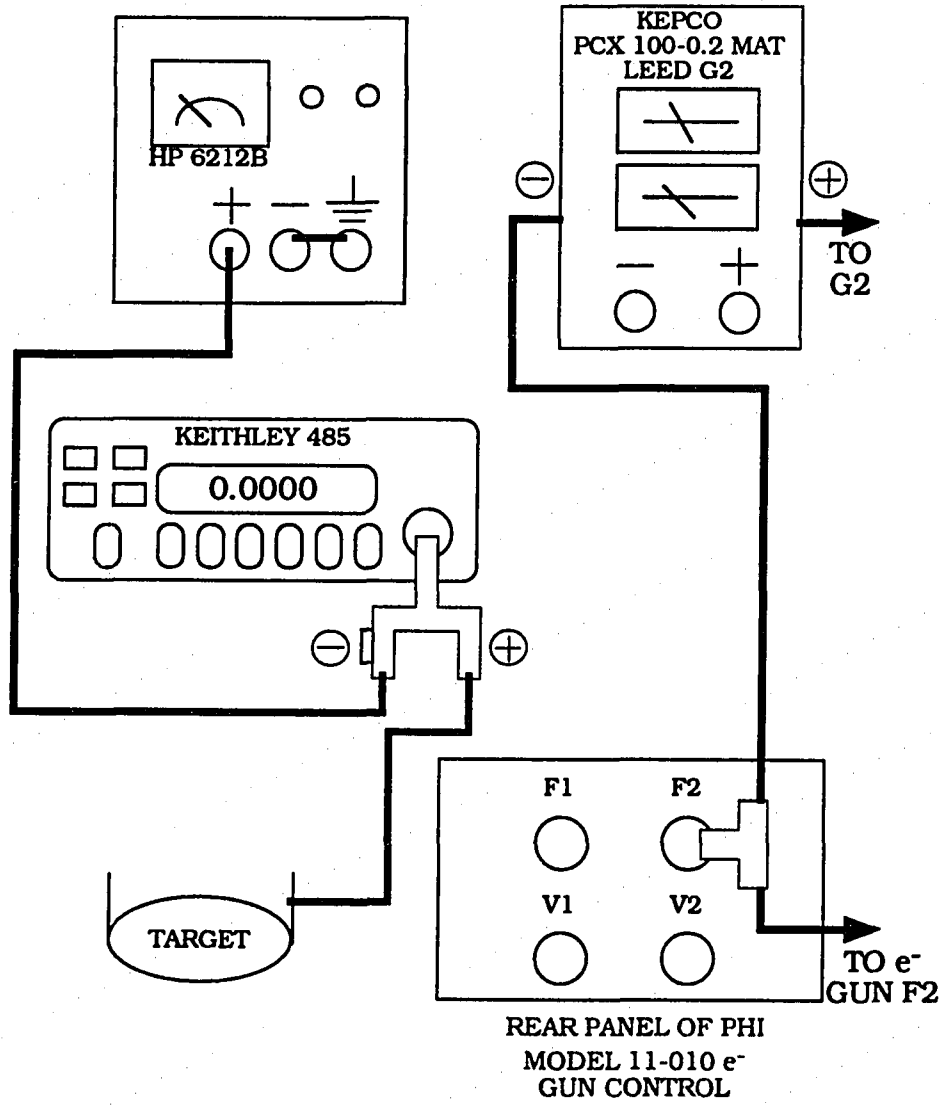

Figure 4. Experimental configuration for LEED.

mounted in the vacuum chamber next to the crystal. (The procedure for recoating this flag is outlined in Jensen #2, pp. 5-6.) Position the flag in front of the electron gun drift tube. Starting with a beam energy of approximately 250 V, set the emission current at 1-2 mA. An illuminated outline of the drift tube exit hole should appear on the phosphor flag. Adjust the focus, emission, and deflector controls until the electron beam is visible as a spot approximately 1 mm^2 in area. Both the x- and y-deflection knobs should be set close to 5.00, since this is the value corresponding to the minimum deflection voltage.

Once the electron beam is properly focused, move the crystal to the front of the ESDIAD optics and in line with the electron gun drift tube. The crystal face should be approximately parallel to the screen, although a slight tilt toward the electron gun may be necessary. Adjust the crystal position, with the electron beam on, until a sample current is observed.

A list of common experimental parameters is shown in table 2 for both ESDIAD and LEED. It is important that both the gain and black level of the CCD camera be in the MANUAL mode to allow for intensity comparisons of different images taken with identical parameters. For viewing the LEED/ESDIAD image it is best if there is no light in the vacuum chamber. The ion gauge filament should be shut off, all viewports should be covered with aluminum foil, and the black cloth cover should be fit over the camera lens.

Before attempting to view the image, set all parameters to the desired value, except the MCP voltage, which should be at 0. Apply the beam voltage and, with the

Table 2. Common experimental parameter for ESDIAD and LEED.

	ESDIAD	LEED
Beam Voltage (V)	-250	-150
Crystal Bias (V)	40	0
Sample Current (nA)	40	40
Grid #1 (V)	GND	GND
Grid #2 (V)	4.0[a]	19.0[b]
Grid #3 (V)	-300	0
MCP[c]	600	500
Screen (V)	4500	4500

[a]referenced to the crystal bias
[b]referenced to the beam voltage
[c]see table 1

camera and monitor on, slowly turn up the MCP voltage until the image is visible on the monitor. Avoid the "blooming" effect associated with a very high MCP current. Once the image is visible, find the center of the crystal with the electron beam by adjusting the crystal position. The LEED/ESDIAD image may be recorded with the VCR and/or sent to the computer for numerical analysis.

IV. COMPUTER-ASSISTED DATA ACQUISITION

A. Starting the Program

The ESDIAD image signal may be sent from the camera control to the Matrox MVP-AT video processor board installed in the Vectra QS/20 computer. A program originally written for video LEED data acquisition, called ACQUIRE.EXE, allows for spot integration, 1-D profiling, and 3-D data structuring. This program, described in detail in ref. [5], is called from within the ESDIAD.BAT batch file, located in the C:\APPLIC\ESDIAD\ sub-directory. This file may be called in one of two ways: (1) selecting ESDIAD from the WP Shell menu, or (2) typing ESDIAD at the DOS prompt from within the correct sub-directory. It is important to call ACQUIRE.EXE with the batch file since this disables the screen saver. One final note on the hardware set-up: it is important that E: is established as a virtual drive. This is accomplished by including the following commands in the CONFIG.SYS file:

```
DEVICE = C:\DOS\RAMDRIVE.SYS 16 512 2 /E
DEVICE = C:\DOS\RAMDRIVE.SYS 1024 512 64 /E
```

B. Setting the Parameters

The purpose of this section is to lead the user through a set-up of the parameters for a typical experiment. Typical parameter values are included in parentheses. As will be the case in sections C and D, only the basic functions necessary to collect the desired information will be covered. For a more complete description of all options, see ref. [5]. Throughout this discussion menu titles will be underlined and keystrokes will be *italicized*.

1. Set the title:

   ACQUIRE --> SETUP --> Title

   Enter a title for the experiment. The program will use this title as the filename for stored data.

2. Set the offset and gain:

   SETUP --> MVP OFFSET/GAIN --> Offset

   Enter the offset (100).

   SETUP --> MVP OFFSET/GAIN --> Gain

   Enter the gain (0).

   MVP OFFSET/GAIN --> *Esc* --> *Esc* --> ACQUIRE

3. Set the number of frames to be averaged:

   ACQUIRE --> *F2* --> IMAGE --> Number of Frames

   Enter the number of frames (60).

   IMAGE --> *Esc* --> ACQUIRE

4. Set the number of windows:

ACQUIRE --> WINDOWS --> Number of Windows

Enter the number of windows (1).

C. Editing the Window(s)

In this section, the size and position of the windows are set, and the data collection options are chosen. For the window set-up, it is helpful if an image signal is sent to the computer. This image may come from either the live camera or a videotape.

1. Create a window:

ACQUIRE --> WINDOWS --> Edit

Enter the number of the window. The window will appear on the monitor. From the window editor select the IMAGE menu by pressing *F10*. Before continuing, an image signal should be sent to the computer from either the live camera or the VCR.

IMAGE --> Image Average --> *Esc*

Following this step, the image, along with the window, will appear on the monitor.

2. Adjust window size and position:

Using the cursor keys, as well as *F1* and *F2*, set the size and position of the window.

3. Set the data options:

Press *F4* to call the data options list. Select the desired option(s): x-profile, y-profile, mean x-profile, mean y-profile, integrate, and block transfer (for 3-D image).

Esc (x4) --> ACQUIRE

D. Collecting the Data

This section describes the actual data acquisition process. Images can be analyzed one at a time or in a continuous fashion as a function of time. Binary data files are created which can be converted to ASCII as described in the next section.

1. Noncontinuous data acquisition:

ACQUIRE --> DATA --> USER INPUT --> Go

The user is prompted to enter an x-value, after which the program performs the intensity measurement. Pressing the *Esc* key will then prompt the user to save the data. This process is repeated until the measurements are complete.

2. Continuous data acquisition:

ACQUIRE --> DATA --> Time

The user is prompted to enter a time constant, i.e. the time between measurements. Hitting any key will begin the measurements; hitting any key will stop the measurements.

3. Saving the data:

Quitting the program will write the files to the virtual drive (E:), and to the active directory on the hard drive (C:\APPLIC\ESDIAD\). The data is also saved by choosing the New Experiment option from the ACQUIRE menu.

E. Converting Data to ASCII Format

Three files are created by ACQUIRE.EXE: (1) FILENAME.LDS stores information about the experiment, (2) FILENAME.LDR stores records for the intensities, and (3) FILENAME.LDD stores the intensities [5]. All three files are written to the C:\APPLIC\ESDIAD\ sub-directory. The first is stored in text mode, while the other two are binary. To convert the binary data to an ASCII format to be read by Axum (or a similar program) use CONVERT.EXE for the integrated intensities, and PRO.EXE for the profiles and 3-d block transfers. Both programs are stored in the C:\APPLIC\ESDIAD\ sub-directory.

V. REFERENCES

1. T.E. Madey, Science 234 (1986) 316.
2. J.T. Yates Jr., M.D. Alvey, M.J. Dresser, M.A. Henderson, M. Kiskinova, R.D. Ramsier and A. Szabo, Science 255 (1992) 1397.
3. R.D. Ramsier and J.T. Yates Jr., Surf. Sci. Rep. 12 (1991) 243.
4. M.L. Knotek, in *Physics Today* 37, 9 (1984) 24.
5. O.L. Warren, Ph.D. Dissertation, Iowa State University (1993).